Title
Fast Detection of Low-Abundance Proteins Based on Ion Concentration Polarization

Author
Lu, Bochao

Publication Date
2019

Peer reviewed|Thesis/dissertation

Fast Detection of Low-Abundance Proteins Based on Ion Concentration Polarization

By

Bochao Lu

A dissertation submitted in partial satisfaction of the requirements for the degree of

Joint Doctor of Philosophy

with the University of California, San Francisco

in

Bioengineering

in the

Graduate Division

of the

University of California, Berkeley

Committee in Charge:

Professor Michel M. Maharbiz, Chair

Professor Adam Abate

Professor Dorian Liepmann

Professor Kristofer Pister

Summer 2019

Abstract

Fast Detection Of Low-Abundance Proteins Based On Ion Concentration Polarization

By

Bochao Lu

Joint Doctor of Philosophy

with the University of California, San Francisco in Bioengineering

University of California, Berkeley

Professor Michel M. Maharbiz, Chair

Molecular detection and analysis are of fundamental importance in disease prevention, disease diagnosis, medical treatment, drug delivery, food industry, and environmental monitoring. Conventional immunoassays require hours of incubation for low concentration analytes (femtomolar) since the rate-limiting step is the transport of target molecules to the biosensors. Thus, a new technology for fast and sensitive immunoassay is highly desirable for disease monitoring and personalized treatments. The work reported in this thesis is focused on developing silicon microfabrication technologies for sensors that can detect low concentration proteins (femtomolar) in a short time (tens of minutes).

We first demonstrate the use of germanium (Ge) films as sacrificial layers that allow the patterning of proteins onto surfaces with commonly used organic solvents. As researchers miniaturize biosensors and microfluidic devices down to submicron scales, high-resolution biomolecule conjugation compatible with these processes is highly desirable. The presented technique is scalable to high volume manufacturing and is compatible with nano- and microfabrication processes, including standard lithography. We achieved nanoscale resolution and misalignment with this technique.

We then discuss the development of ICP-based preconcentration devices on silica and silicon substrates. We report two nanofabrication strategies in this chapter that enhance the accumulation of protein molecules via 1) an increase in the number of nanochannels per microchannel and 2) an increase in the depth of nanochannels. Increasing the depth of nanochannels leads to the switch from silica substrates to silicon substrates, using deep reactive ion etch (DRIE). We also report the attempts for antibody immobilization in the ICP preconcentrators using previously reported Ge technique. However, due to the instability of

antibodies in the drying process, we switched to bead-based immunoassays in our preconcentration devices.

After the demonstration of protein preconcentration in our devices, we present a scalable method for fabricating hundreds of vertical nanochannels (6.5 μm deep) employing ion concentration polarization (ICP) enrichment for fast analyte detection. Compared to horizontal nanochannels, massively paralleled vertical nanochannels not only provide comparable electrokinetic functions but also significantly reduce effective fluid resistance in each microfluidic channel, which enables microbead loading for sensing purposes. These nanochannels filter microbeads by size and preconcentrate analytes at the anodic side of the test area via electrokinetic entrapment. The device is capable of enriching protein molecules by >1000 fold in 10 min. We demonstrate fast detection of IL6 down to 7.4 pg/ml with only a 10 min enrichment period followed by a 5 min incubation, which is a 162-fold enhancement in sensitivity compared to that without enrichment. Our results demonstrate the possibility of using silicon/silica-based vertical nanochannels to mimic the function of polymer membranes for protein enrichment.

To my mother

Contents

List of Figures

Acknowledgements

I feel so fortunate to be mentored by and work with so many talented individuals throughout my PhD. I would like to acknowledge all the people who mentored and supported me through this journey.

First and foremost, I must acknowledge Professor Michel. M. Maharbiz, my research mentor and my dissertation committee chair, without whom I would not have the opportunity to present this work. His support, guidance, and encouragement have made a huge impact not only on my research, but also on my personal growth as a scientist and an engineer. He also played a critical role in shaping me into a better person. He encouraged me to be not only a smart person but also a person making wise decisions. I can never give enough thanks and admiration to Prof. Maharbiz. Thanks also go to Prof. Adam Abate, Prof. Dorian Liepmann, and Prof. Kris Pister for serving on my committees.

I also want to give my thanks to my labmates in the Maharbiz lab. I thank Travis Massey, Camilo Diaz-Botia, Maysam Chamanzar, Tom Zajdel and Konlin Shen for their training, guidance, and help in fabrication. In my 3rd year in the program, Travis and I were the only two people working in the Nanolab at midnight. We were each other's partner (Nanolab buddy) for the work at night. It was Travis, who helped me during those painful troubleshooting nights in the Nanolab. In addition, I am very grateful toward Amy Liao. She not only helped me in lab, but also introduced me to the world of consulting, which revealed another excellent career option after PhD. I would not have been able to land a role at BCG without the case-interview practices with Amy.

I have many thanks for all other lab members: Monica Lin, Alyssa Zhou, Arda Ozilgen, David Piech, Oliver Chen, KyoungTae Lee, DJ Seo, Stefanie Garcia, Wei Li, and Soner Sonmezoglu. It was my pleasure to work and establish lifetime friendships with all these talented individuals. I am so grateful for all the time we shared together and the support they provided during the hard times of my PhD.

I am thankful for all my friends throughout my entire PhD process. Many of them helped me both in the lab and in daily life.

The work I have done in this thesis would not have been possible without funding from the Defense Advanced Research Projects Agency, and the Berkeley Sensor and Actuator Center.

Most importantly, I have a deep debt of gratitude to my family, especially to my mother. My mother provided whatever she could to give me a better education. Without her love and support, I would not have been able to come to the United States. It is my fortune to be her only son.

Chapter 1: Introduction

1.1 Micro/nanofluidic preconcentration is important for biosensing

Molecular detection and analysis are of fundamental importance in disease prevention, disease diagnosis, medical treatment, drug delivery, food industry, and environmental monitoring.[1–4] With advances in microfabrication technologies, miniaturized biosensors have been developed and integrated into microfluidic platforms. These microfluidic biochips have numerous advantages over traditional benchtop devices, including faster detection speeds, lower costs, higher sensitivities, less sample volume needed, and greater suitability for portable devices. Thus, miniaturized biosensors have attracted much interest in the past two decades [2,5–8].

In order to perform a reliable and accurate detection of a diffusible analyte, that analyte's concentration must be higher than a putative sensor's lower limit of detection (LOD). However, for many biosensing applications this can be very difficult. Examples include sensing analytes for the diagnosis of early stage cancers [9,10] and the detection of heavy metals that are lethal at low concentration [11], among others. When the analyte concentrations are extremely low (femtomolar), the rate-limiting step is the analyte transport to the biosensors [12–15]. For example, Ying-Chih Wang et al. (2008) showed that the equilibrium time of R-phycoerythrin (R-PE) capture by an antibody increases significantly as concentration decreases [16]. For this reason, many sensing methods make use of prolonged incubation times (> several hours) when detecting low concentration analytes - especially when the target concentration is lower than the antibody dissociation constant.

However, some applications demand faster detection times (< 1 hr). A very important example is the detection of sepsis in human patients. Sepsis is the tenth leading cause of death in developed countries [17]. Sepsis arises when the body's own immune response to an insult (like infection or injury) is so acute that it leads to tissue damage and if untreated, eventually organ failure and death. Despite a small decline in mortality rate, the total number of patients dying from sepsis is still growing due to antimicrobial resistance, the growing elderly population, the wider use of immunosuppressive therapies, and more invasive medical technologies [18]. Cytokines are the critical chemical signaling mediators and biomarkers for inflammatory diseases such as sepsis. Cytokine concentrations are significantly correlated with septic patient mortality rate and can be used for sepsis diagnosis [19–21]. Septic patients' survival rate decreases by 8% for each hour delay of treatment [22], so these patients have to be treated immediately. However, conventional cytokine detections take hours if not days due to their low concentrations (femtomolar). Thus, a

new technology for biomolecular detection, which is fast and highly sensitive, is highly desirable for cytokine level monitoring to open the door to patient-specific treatment [23,24].

Many assays have been developed for biosensing at low concentrations via signal amplification and/or high-sensitivity sensors, such as optical microcavity-based assays[25], magnetic bead-based assays [10,26], cantilever-based biosensors [27–30], nanowire-based immunoassays [31–34], graphene-enhanced immunoassays [35–39], and surface plasmon resonance-based analyte detections [40–44]. However, most of these technologies rely on high-quality antibodies (low dissociation constant) and/or require lengthy incubation times. Therefore, fast detection for low abundance analytes remains a challenge.

Another approach for rapid and sensitive detections is analyte preconcentration. The simplest method for analyte enrichment is physical filtration, in which large analytes are size-excluded from the filter [45,46]. However, physical filtration membranes have clogging issues and low recovery rate. There are many sample preconcentration devices based on electrokinetic phenomena, including amplification stacking [47–50], isoelectric focusing [51–54], dielectrophoresis [55–58], and isotachophoresis [59]. Of these various techniques, micro/nanofluidic analyte enrichment using ion concentration polarization (ICP) has attracted a lot of attention because of its high enrichment factor (up to 10^6 fold) [60]. Besides the enrichment factor, ICP-based preconcentration has following three major advantages: 1) no need for special buffers or reagents; 2) uses only DC voltages, so the instruments are much simpler (compared to dielectrophoresis); 3) preconcentrates charged molecules regardless of their sizes. Due to these advantages, ICP-based enrichment has been applied to a lot of different analytes such as cells, protein, DNA, metal ions, and other small molecules [1].

1.2 Foundations of ICP-based preconcentration

1.2.1 Mechanism of ICP-based preconcentration

As we discussed above, analyte enrichment is highly desirable to enhance the LOD of biomolecule detection. ICP effect is one of the most commonly used methods for the preconcentration of charged analytes [1,3,61]. The ICP phenomenon usually appears at the junction region between microchannels and nanochannels (or perm-selective membranes). These nanochannels allow counter-ions to pass across, while most of the co-ions are blocked by electrostatic repulsion. This phenomenon is called ion-selectivity (or perm-selectivity), which is the key to generating ICP.

For the case of negatively charged microchannels and nanochannels (or perm-selective membranes), electroosmotic flow (EOF) carries the bulk solution from the anode to the cathode under DC voltages. Due to the cation selectivity of the nanochannels (or membranes), more cations (counter-ions) are transported through these nanochannels than anions (co-ions), resulting in the formation of ion depletion at the anodic side of the nanochannels (Fig 1.1 a). The depletion zone has very low concentration of ions and therefore induces a large electric field. The amplified

electric field in the depletion zone repels negatively charged molecules (including negatively charged analytes) toward the anode by electrophoretic force (Fig 1.1b). In addition, the low ionic strength in the depletion zone induces non-equilibrium space charge layers, which in turn results in the accelerated non-equilibrium EOF (EOF of the 2nd kind). The non-equilibrium EOF in the depletion zone has a much higher velocity than the EOF in the bulk solution. Since the fluid is incompressible, strong vortical flows are generated in the depletion zone (Fig 1.1c).

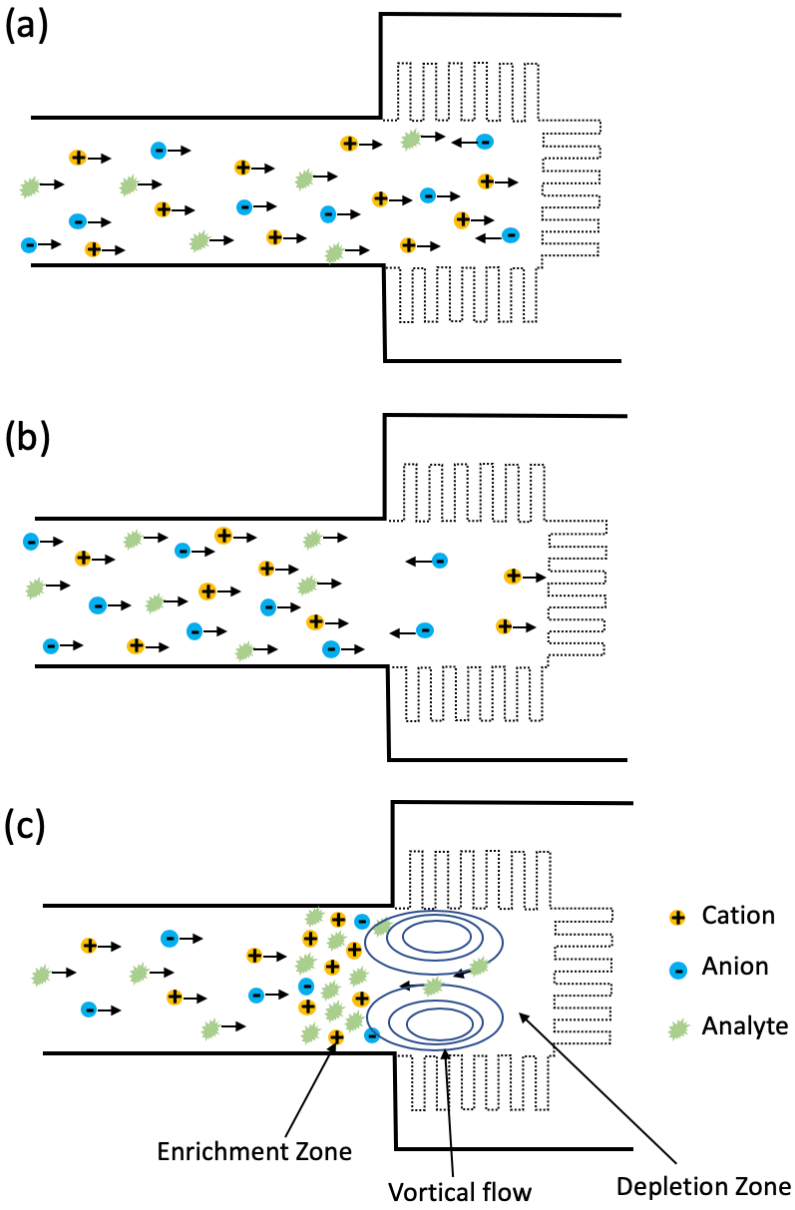

Fig 1.1 The mechanism of ICP in front of nanostructures.
The anode is on the left side of the nanostructure. (a) The negatively charged nanochannels transport more cations than anions. (b) The additional cations transported by surface conduction initiate a weak concentration polarization and decrease ion concentration on the anodic side of the nanochannels. The lower ionic strength increases the thickness of local electrical double layers (EDL), which enhances permselectivity of nanochannels. This positive

feedback promotes a strong concentration polarization even when the Debye length is significantly shorter than the nanochannel width. (c) The depletion zone induces nonequilibrium space charge layers and generates nonequilibrium EOFs near nanochannels, which induces vortical flow. The backwards fluid flows along with the amplified electric field in depletion zone move analytes (negatively charged) upstream until the convection and electromigration balance, resulting in analyte enrichment.

The force analysis of analytes is shown in Fig 1.2. When the negatively charged analytes are far from the nanostructures, the dragging force of EOF (1st kind) is dominant and brings analytes toward the nanostructures (Fig 1.2a). When the negatively charged analytes are in the depletion zone, the amplified electrophoretic force (electromigration) and the dragging force from the back flow of the vortical flow (EOF of the 2nd kind) become larger than the EOF of the 1st kind, bringing analytes upstream (Fig 1.2b). Thus, the backflow of the circulation flows and the amplified electromigration bring analytes upstream until the convection balances the electromigration (Fig 1.2c), resulting in the enrichment of negatively charge analytes at the boundary of the depletion zone [62].

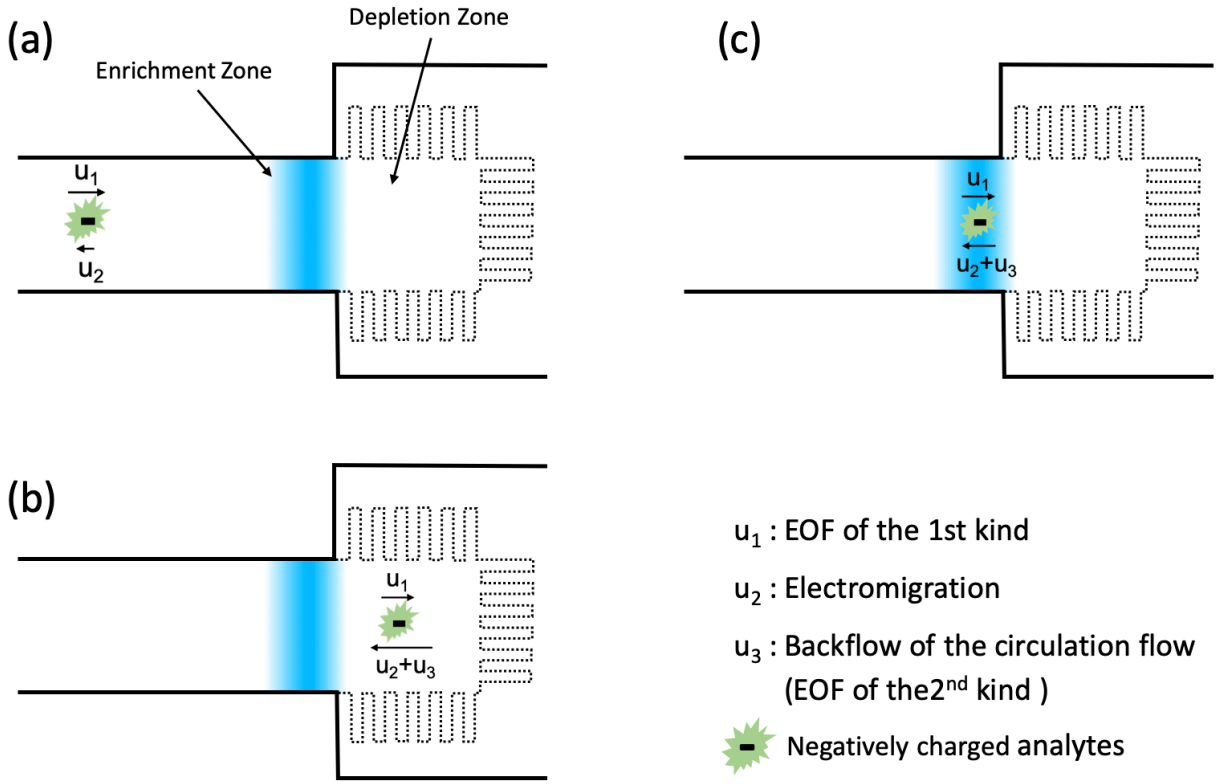

Fig 1.2 Mechanism of ICP-based analyte enrichment.
(a) EOF of the 1st kind dominates at positions away from the nanostructures. (b) The amplified electromigration and the back flow of the vortical flow overcome the EOF of the 1st kind in the

depletion zone. (c) Analytes accumulate at the position where electromigration and convections balance.

The overlap of electrical double layers (EDLs) was previously believed to be the cause of this ion-selectivity in nanochannels, but recent research showed that the ratio of surface conduction to bulk conduction is the key for this phenomenon [63]. Most of the silica-based preconcentrators [16,60,64–67] including our devices in Chapter 4 have nanochannels at the sizes of ~30-40 nm, but the thickness of EDL is usually < 3 nm, depending on the specific buffer solution they used. These devices can still induce ICP-based preconcentration with non-overlapped EDLs, because surface conduction (the ion conduction in EDLs) causes additional cations (counter-ions) to transport through the nanochannels. This additional cation conduction through the EDL is usually overwhelmed by bulk conduction unless the channel size is comparable to the EDL thickness. This additional cation conduction initiates a weak ICP and slightly lowers the ion concentration at the anodic side of the nanochannel. The lower ion concentration increases the perm-selectivity of nanochannels due to the local thicker EDL, which in turn initiates a positive-feedback toward the faster formation of full ICP. This positive-feedback mechanism enables the use of ICP-based preconcentration even at moderate or high (~100mM) ion concentrations.

1.3 Important factors in ICP-based preconcentration

1.3.1 Dukhin number and nanochannel sizes

There are many factors that may vary the ICP-based enrichment, including channel sizes, ionic strength, applied voltages, surface charge density, pH values of the sample solutions etc. As we discussed above, surface conduction (EDL conduction) in nanochannels (membranes) is the key factor for ion-selectivity. The surface conduction is the ion current through EDL, which is induced by the electric field across the channels. The ion current through EDL is mainly composed by the transport of counter-ions since counter-ions outnumber the co-ions in EDLs, which is the cause of the ion-selectivity. The ion-selectivity can be quantified by the Dukhin number, which is the ratio of the surface conductivity to the bulk conductivity [63]. The Dukhin number indicates the dominant mechanism of conduction and the ion-selectivity of the nanochannels.

To induce ICP, the size of the nanochannel has to be at the same scale as the characteristic thickness of the EDLs (Debye length). As the channel size decreases down to tens of nanometers, the bulk conduction decreases dramatically and therefore the Dukhin number as well as the ion-selectivity increases accordingly. For example, most of the ICP-based preconcentrators on silicon/silica substrates use ~40 nm nanochannels, while their systems have Debye lengths ~ 3 nm [16,60,64–67]. Although the EDLs are not overlapped in these devices, the bulk conduction has been decreased to the extent that the surface conduction cannot be overwhelmed by the bulk conduction anymore, resulting in the ion-selectivity in these nanochannels. With larger sizes, the nanochannels cannot provide enough ion-selectivity and in turn cannot induce ICP development.

1.3.2 pH value

In addition, the pH value of the sample solution also plays an important role in ICP-enhanced immunoassays. First, the pH value determines the charge density on the surfaces of micro-/nanochannels. For example, in a silica-based device, a higher pH induces more deprotonated silanol groups and therefore results in higher charge density on the silica surfaces. The surface conduction and Dukhin number increases as the charge density increases, which in turn enhances the ICP development. Second, the pH value not only affects the surface charge density on channel sidewalls but also changes the surface charges on analyte molecules. Based on the concept of ICP, only charged molecules can be trapped at the boundary of the depletion zone. If the pH value of the sample solution is the same as the isoelectric point (pI) of the target molecules, then most of the molecules are neutral. Thus, analytes cannot be enriched by electrokinetic force, when the pH value of the solution equals the pI value of analytes. The pH value also determines the electrical mobility of analytes by changing the surface charge on molecules. Since the analyte accumulation depends on the counteracting effects of the electromigration and the convection (the bulk flow induced by the EOFs of the 1st kind and the vortical flow caused by the EOFs of the 2nd kind) at the interface of the depletion zone, different molecules can be trapped at different locations based on their electrical mobilities [68]. Thus, by changing the pH value of the solution, researchers can determine which analyte can be enriched and where the analyte can be trapped. Third, the pH value also affects the efficiency of the immunoassay integrated with the ICP-based preconcentration. By adjusting the pH value far away from the pI value of the targets, researchers can achieve more efficient trapping of the target molecules. However, the pH value also significantly affects the antibody-antigen binding affinity. For example, the equilibrium constant of the same antibody-antigen pair is 100-fold higher at neutral pH than at pH 5.0 or 9.5 [69]. Therefore, extreme pH values should be avoided for ICP-enhanced immunoassays using antibodies.

1.3.3 Different materials

Besides the pH values of sample solutions, surface charge density also varies among different substrate materials. Thus, silica surfaces are usually preferred rather than silicon surfaces for ICP development [16,60,64–67], since silica surfaces have more silanol groups available and in turn have higher charge density than silicon surfaces. The higher charge density of the surface increases the surface conduction in EDLs, which is helpful for ICP development. Nafion membrane is also commonly used for ICP-based preconcentration due to its high surface charge density [68,70–78].

1.3.4 Ionic strength

Furthermore, ionic strength is another deterministic factor for ICP-based preconcentration. Lower ionic strength leads to higher zeta potential on the substrate surfaces, which in turn results in a faster electroosmotic flow. Electroosmosis is the leading cause of the bulk flow, and the bulk flow brings all the analytes toward the enrichment zone. Thus, the change in background ionic strength affects the flux of analyte molecules entering the enrichment zone, and as a result, determines the speed of the enrichment. More importantly, the lower ionic strength of the sample

solution induces thicker EDLs, which enhances the ion-selectivity of nanochannels. Thus, ICP can be initiated and developed faster in the solution with lower ionic strength. The efficiency of analyte trapping is higher at lower buffer concentrations with fewer molecules leaking through the nanochannels (or membranes).

However, lower ionic strength is not always better for the ICP-based preconcentration. Although the lower ionic strength can accelerate the ICP-based analyte accumulation, the final achievable concentration factor may decrease if the background buffer concentration is too low. The concentration factor is defined as the ratio of the final peak analyte concentration to the initial analyte concentration. At high buffer concentrations, the thinner EDLs in nanochannels lead to a compromised ion depletion effect due to lower surface conductivity and weaker cation-selectivity. Thus, the analytes cannot be trapped efficiently by the compromised depletion zone, resulting in analytes leaking through the depletion zone. In this 'leaking' regime, lowering the buffer concentration can improve the ICP development and therefore enhance the analyte trapping efficiency, entering 'non-leaking' regime and achieving higher concentration factors [62].

In the 'non-leaking' regime, the ICP can be fully developed, and the depletion zone can perfectly trap the analytes. After the system enters the 'non-leaking' regime, decreasing the buffer concentration lowers the peak analyte concentration and the concentration factor. This is because when the analytes are perfectly trapped and highly concentrated, the negatively charged analytes replace background anions, becoming one of the leading charge carriers in the enrichment zone. When the background anion concentrations decrease down to zero to maintain electroneutrality, the cations are neutralized solely by negatively charged analytes, and the analyte concentration can no longer be concentrated further. Thus, in the 'non-leaking' regime, the background buffer concentration determines the final analyte concentration, and therefore, lowering the buffer concentration in this regime decreases the concentration factor [62]. This effect is not problematic for the purpose of immunoassays since most antibody pairs can detect antigens easily at micromolar concentrations, while most of the preconcentrators use background buffers at millimolar levels [61], which are at least three orders of magnitude higher than the concentration we need for biomolecule detections.

1.4 Current fabrication methods to induce ICP-based preconcentration

ICP development requires ion-selective nanochannels or nanopores (in perm-selective membranes) connecting to microscale channels. There are many methods reported for the fabrication of these nanofluidic features. These fabrication techniques can be categorized by different materials. The earlier fabrications of these nanofluidic devices used expensive nanofabrication techniques on silicon/silica substrates. These fabrication techniques are costly, but they are usually CMOS compatible and do not require non-conventional fabrication tools. Recently, multiple cheaper prototyping approaches have been developed using perm-selective membranes such as Nafion. Nafion patterning is one of the most widely used fabrication strategies for ICP-based enrichment due to its cheaper and faster prototype process with no requirement for clean-room settings. Also, there are other non-lithographic methods in literature such as self-assembled

colloidal nano-beads [79,80], elastomeric microvalves [81], PDMS wrinkling [82], and nanojunction gap breakdown with high voltage [83]. In section 1.4, we present the current fabrication strategies for ICP-based preconcentrators.

1.4.1 Silicon/silica based preconcentrator

ICP-based preconcentration was first reported with silicon/silica nanochannels [60][67]. These devices were fabricated using conventional photolithography tools. The 5 μm – 20 μm wide nanochannels were patterned on the silicon substrate first and etched with reactive ion etching (RIE) for the depth of 40 nm. After etching the nanochannels, the microchannels were then patterned and etched with a similar process, except that a longer RIE process was used for deeper channels in microscale. Subsequently, the through-hole reservoirs were achieved by KOH etching or manual grinding. After fabricating all features on the silicon substrates, a layer of thermal oxide was grown on the device for better electrical insulation. After oxidation, the devices were sealed with a silica or glass wafer by anodic bonding, or the devices could be sealed using polysilsesquioxane (PSQ) as an adhesive layer (see details in Chapter 3).

In these devices, the nanofluidic channels are only 40 nm deep, and the Debye length is no longer negligible (at buffer concentrations ~10 mM). For the negatively charged silica surfaces, these nanochannels can be cation-selective, transferring more cations (counter-ions) than anions (co-ions). This cation-selectivity results in the development of ICP and analyte preconcentration. Most of these silicon/silica-based preconcentrators use horizontal nanochannels as we described above [16,60,64–67]. These nanochannels cannot provide enough fluidic flow through the nanofluidic channels. Therefore, all of these preconcentrators have their nanochannels perpendicular to the main microchannels so that the main flow does not go through these nanochannels, which leads to more complicated structures and more difficulties in multiplexing.

Compared to horizontal nanochannels, hundreds of vertical nanochannels can provide more volumetric flow through the nanochannels to enable sample loading and washing steps in immunoassays without the perpendicularity between nanochannels and microchannels. In Chapter 4 of this dissertation, we report a new fabrication process for a nanostructure with hundreds of vertical nanochannels (nanogaps). In brief, the vertical nanochannels were etched with RIE and then shrunk from 250 nm to 30 nm with oxide deposition. These vertical nanochannels concentrate analytes by ICP development and collect microbeads via size filtering for bead-based immunoassays. Bead-based immunoassays have been successfully performed in front of these vertical nanochannels and the sensitivity is improved by two orders of magnitude (details in Chapter 4).

1.4.2 PDMS based preconcentrator using horizontal Nafion membranes

Instead of fabricating silicon/silica-based nanochannels, which requires clean rooms and advanced photolithography tools, researchers can pattern a thin layer of perm-selective membrane on a glass slide and then bond a layer of PDMS with microchannels on top of that membrane to form an ion-selective junction [68,70–78]. For example, Nafion is one of the most commonly used

ion-selective membranes, with high surface charge density due to its strongly negatively charged sulfonic groups.

There are generally two ways to pattern Nafion membranes - micro-flow patterning and micro-stamping [61][78]. In the micro-flow patterning method, a PDMS layer with microchannels defining the membrane shapes is reversibly bonded to the glass substrate followed by the loading of Nafion perfluorinated resin. Then, the resin is completely removed by applying negative pressure on one end of the channel. After curing at 95 ^{o}C, the PDMS layer is removed, leaving the Nafion membrane on the glass substrate. Finally, the PDMS chip with preconcentrator structures is bonded on the Nafion patterned glass substrate via conventional plasma bonding. In this method, the thickness of the Nafion membrane can be tuned by varying the concentration of the Nafion resin and the incubation duration of resin in the microchannel. Alternatively, the Nafion membrane can be patterned on the glass substrate by micro-stamping. In this method, a block of PDMS with stamping patterns is dipped into Nafion perfluorinated resin, and then the Nafion resin is stamped onto the glass substrate. After curing the Nafion resin, the PDMS chip is bonded on top of the Nafion membrane with the same process as the micro-flow patterning method.

1.4.3 PDMS based preconcentrator using vertical Nafion membranes

In addition to horizontal Nafion membranes, another technique called 'self-sealed' junction method is also useful to build PDMS concentration devices with vertical Nafion membranes [84]. This method utilizes the flexibility and softness of PDMS to insert Nafion membranes into the devices without additional photolithography processes. The PDMS chip with preconcentration structure is cut with a knife at the location where the nanofluidic junction is supposed to be. Then, the gap is opened by bending, and the Nafion resin is infiltrated into the incision. After Nafion resin infiltration, the PDMS is released to close the gap, and excessive Nafion resin on the surface is removed manually. The Nafion resin is trapped and cured in the incision, followed by plasma bonding of the PDMS chip onto a glass substrate. In this technique, the Nafion membrane is vertically inserted into the PDMS layer with a high aspect ratio, which enables a high throughput preconcentration device with large channels (1000 μm width x 100 μm depth).

1.4.4 Other methods to induce ICP based preconcentration

Instead of using silicon/silica nanochannels or ion-selective membranes, one can also use self-assembled silica nano-beads to achieve ion-selective nanofluidic junctions [79,80]. In this technique, polyelectrolytes are deposited layer by layer on top of 300 nm colloidal silica beads, and these silica beads are then loaded into the bead delivery channels. After air drying for three hours, colloidal silica beads form a cation-selective membrane by self-assembly with an average pore size ~15% of the silica bead diameter. The pore size of the resulting nanoporous membrane can be further tuned by ionic strength [85], the pH value of the solutions [85,86], and temperature [87]. With this technique, Syed et al. preconcentrated DNA up to 1700 fold in ~10 min [80].

Besides colloidal beads, there are some other techniques to fabricate ion-selective nanofluidic junctions with PDMS only. For example, an elastomeric microvalve can be used to create a nanofluidic junction within the sample channel to induce ICP [81]. In this technique, there

is a control channel on top of the sample channel. Applying pressure in the control channel can close the valve, forming nano-space underneath the microvalve in the sample channel. The nano-space heights vary between ~55 nm and ~7 nm depending on the pressure applied in the control channel. The advantage of this technique is that the concentrated analytes can be transported downstream by opening the valve, in case that concentrated sample collection is desired.

In addition to microvalves, nanochannels can be formed via a PDMS wrinkling process. After oxygen plasma treatment, a thin stiff film can be formed on a stretched PDMS surface [82]. This stiff film is mainly composed of SiO_x, the density of which is approximately 50% of the density of silica. After slowly releasing the PDMS layer, a sinusoidal wrinkled surface can be formed on top of the PDMS layer [82]. The amplitude and period of the wrinkled surface vary between 50-600 nm and 100-3500 nm, respectively, depending on the magnitude of the strain and the exposure time to the plasma. To localize the wrinkled pattern in the nano-junction area between microchannels, the researchers usually cover the PDMS layer with a mask during oxygen plasma except for the nano-junction areas. Besides the oxygen plasma treatment, focused ion beam [88] and ultraviolet/ozone [89] can also be used to create such wrinkled nanochannels.

Another non-photolithographic technique to create nanofluidic junctions is to use high voltage to break down the junction gap between two PDMS microchannels [83]. In this technique, a PDMS layer with two adjacent microchannels is irreversibly bonded onto a glass slide after standard oxygen plasma treatment. After filling both of the microchannels with 10^{-2} M phosphate buffer, a high voltage (>1000V) is then applied between two microchannels, forming nanogaps by electrical breakdown. This technique is straightforward, but the limited ion-selectivity of the nano-junctions and the non-reproducible bonding strength between silica and PDMS constrain the efficiency of analyte preconcentration.

Furthermore, there are multiple other materials and techniques to induce ICP-based analyte enrichment. Chun et al. developed an ICP-based preconcentrator using a poly-AMPS (2-acrylamido-2- methyl-1-propanesulfonic acid) membrane between two microchannels [90]. Poly-AMPS is a cation-selective polymer membrane, and the sulfonic groups keep AMPS negatively charged over a wide pH range. Song et al. reported an ICP preconcentration device with a 50 μm thick nanoporous Zwitterionic polymer membrane between two microchannels [91]. The Zwitterionic polymer membrane was fabricated inside the junction of two microchannels using laser-patterning. In the laser-patterning process, a monomer solution was loaded in the microchannels followed by the excitation with a 355 nm laser beam. The laser exposure triggered the polymerization and resulted in a membrane formation in the junction between two microchannels. In addition, Dhopeshwarkar et al. and Hlushkou et al. reported ICP development and biomolecule enrichment using ion-selective hydrogel micro-plugs [92,93]. Furthermore, Nafion can also be integrated onto paper-based devices (μPADs) in order to enhance the sensitivity of paper-based immunoassays. By depositing Nafion in the center of the wax-printed μPADs, Yang et al. reported ~20-fold enrichment of fluorescein-labeled bovine serum albumin (FITC-BSA) with a convergent-channel design in 130 s [94] and Yeh et al. demonstrated an 835-fold concentration of FITC-BSA with shallow paper-based channels [95].

1.5 Dissertation outline

In this thesis, we present two major topics - protein patterning with germanium as a sacrificial layer and ICP-enhanced immunoassays.

In Chapter 2, we demonstrate the use of germanium (Ge) films as water-soluble features that allow the patterning of proteins onto surfaces with commonly used organic solvents. As researchers miniaturize biosensors and microfluidic devices down to submicron scales, high-resolution biomolecule conjugation compatible with these processes is highly desirable. The presented technique is scalable to high volume manufacturing and is compatible with nano- and microfabrication processes, including standard lithography. We show that 50 nm thick Ge layers can be completely removed in 10 min without residues remaining on the surface. More importantly, nanoscale resolution and misalignment can be achieved with conventional photolithography equipment. Also, the process can be used to functionalize sidewalls, a capability of recent interest for cell-cell adhesion studies.

In Chapter 3, we discuss the development of ICP-based preconcentration devices on silica and silicon substrates. This chapter explains why we started with a single-nanochannel preconcentrator on silica substrates and then switched to a multi-nanochannel design with deeper etching. We also report two nanofabrication strategies in this chapter to enhance the accumulation of protein molecules via 1) an increase in the number of nanochannels per microchannel and 2) an increase in the depth of nanochannels. Both of these two strategies provide a higher volumetric flow rate and protein accumulation rate. Increasing the depth of nanochannels leads to the switch from silica substrates to silicon substrates, using different etching techniques. This chapter also includes the DRIE recipe for high-aspect-ratio nanochannels. Besides the fabrication challenges, multiple attempts at surface protein immobilization are also reported in this chapter. However, due to the instability of antibodies in the drying process, bead-based immunoassays are used in the next chapter.

Chapter 4 presents a scalable method for fabricating vertical nanochannels (6.5 μm deep) employing ion concentration polarization (ICP) enrichment for fast analyte detection. Compared to horizontal nanochannels, massively paralleled vertical nanochannels not only provide comparable electrokinetic functions but also significantly reduce effective fluid resistance in each microfluidic channel, which enables microbead loading for sensing purposes. These nanochannels filter microbeads by size and preconcentrate analytes at the anodic side of the test area via electrokinetic entrapment. The device is capable of enriching protein molecules by >1000 fold in 10 min. We demonstrate fast detection of IL6 down to 7.4 pg/ml with only a 10 min enrichment period followed by a 5 min incubation, which is a 162-fold enhancement in sensitivity compared to that without enrichment. Our results demonstrate the possibility of using silicon/silica-based vertical nanochannels to mimic the function of polymer membranes for protein enrichment.

Chapter 2 : Germanium as a scalable sacrificial layer for nanoscale protein patterning

Adapted with permission from:

1. B. Lu and M. M. Maharbiz, "Protein patterning using germanium as a sacrificial layer," *2017 39th Annual International Conference of the IEEE Engineering in Medicine and Biology Society (EMBC)*, Seogwipo, 2017, pp. 1865-1868. doi: 10.1109/EMBC.2017.8037210

2. Lu B, Maharbiz MM "Germanium as a scalable sacrificial layer for nanoscale protein patterning." *PLoS ONE.* 2018;13(4): e0195062. https://doi.org/10.1371/journal.pone.0195062

2.1 Abstract

We demonstrate the use of germanium (Ge) films as water-soluble features that allow the patterning of proteins onto surfaces with commonly used organic solvents. This technique is scalable for manufacturing and is compatible with nano- and microfabrication processes, including standard lithography. We use Ge as a sacrificial layer to mask and protect areas of the substrate during surface functionalization. Since Ge dissolves in 0.35% hydrogen peroxide (H_2O_2) in water but not in organic solvents, Ge can be removed after patterning without significantly affecting protein activities. In this chapter, we present examples of protein patterning with two different techniques. We show that 50 nm thick Ge layers can be completely removed in 10 min without residues and, importantly, nanoscale resolution and misalignment can be achieved with conventional photolithography equipment. Both biotin and streptavidin maintain ~80% and >50% activity after 10 min and 360 min incubation in 0.35% H_2O_2, respectively. Lastly, the process can be used to functionalize sidewalls with proteins, a capability of recent interest for cell-cell adhesion studies.

2.2 Introduction

As researchers miniaturize biosensors and microfluidic devices down to submicron scales[96–98], high-resolution biomolecule conjugation compatible with these processes has become desirable. Several protein patterning techniques have been demonstrated, including gasket-based patterning[99,100], microcontact printing (μCP)[100–104], and dip pen lithography (DPL)[105–107]. Gasket-based patterning is the easiest and arguably most popular protein patterning approach in academic work. In this approach, removable polymer gaskets, usually made of polydimethylsiloxane (PDMS), are used as a mask on the conjugation surface to localize surface functionalization reagents. Since alignment is usually performed manually, it is difficult to precisely align the polymer gaskets with existing surface structures. This method is suitable for low resolution and low throughput research projects, but is difficult to scale up. DPL and μCP are both based on the contact between small probe tips with surface chemistry reagents and a substrate surface. μCP uses PDMS stamps with micron[101,104] or, more recently, submicron features[103] to pattern functionalization reagents onto a substrate. This method exhibits higher resolution and throughput than that of gasket-based methods, but the alignment between desired protein patterns and existing features is limited by the alignment tool. DPL involves using an atomic force microscopy (AFM) tip to trace out the functionalization patterns and can achieve nanoscale resolution with submicron alignment, but usually requires custom AFM systems and is thus difficult to scale up for bulk manufacturing.

To achieve high resolution, precise alignment and bulk manufacturability, engineers have long turned to photolithography techniques to pattern surface moieties. For example, lithographically patterned gold films can be functionalized with thiol groups to pattern proteins onto gold surfaces selectively[108–110]. However, gold thin films may have strong interference with fluorescent signals, so this process may not be suitable for some cases requiring a fluorescent readout. Another common technique involves depositing a sacrificial layer, such as common photoresists, to occlude a region of the surface where conjugation is unwanted, and subsequently dissolve the sacrificial layer with a biocompatible solvent[98,111,112]. However, photoresists can be problematic for surface chemistries that require organic solvents, since photoresists dissolve quickly in most of the commonly used organic solvents (e.g. ethanol, acetone, isopropyl alcohol (IPA) and dimethyl sulfoxide (DMSO)). For example, silane is commonly used for silica surface functionalization, but due to the hydrolysis of silane groups in aqueous solution, an organic solvent like ethanol or DMSO is preferred for silane dissolution in order to maintain the activity of silane groups. A sacrificial layer which will dissolve in a biocompatible solution but not in commonly used organic solvents would enable precise surface conjugation across a wider range of surface chemistries. While there are alternatives to photoresist such as using a dissolvable metal as a sacrificial layer in protein lift off[113], the dissolution rates of these metals are low at neutral pH, they are difficult to deposit, and some are flammable.

Here, we demonstrate a simple, inexpensive and manufacturable protein patterning technique with submicron resolution and only nanoscale misalignment using germanium (Ge), a semiconductor material, as a sacrificial layer for a lift-off process. This method is suitable for creating patterns of a target material on a surface using a sacrificial material. Ge has been studied for decades in the field of microelectromechanical systems (MEMS) and has been used as a sacrificial layer due to its solubility in aqueous solutions[114,115]. Ge dissolves slowly in aqueous solution, but is not affected by most organic solutions[116]. Germanium is first oxidized into germanium dioxide by oxidizing agents (e.g. dissolved oxygen molecules or aqueous hydrogen

peroxide (H_2O_2)). H_2O_2 accelerates the oxidation of Ge since it is a much stronger oxidizing agent than oxygen molecules. The spontaneous dissolution of germanium dioxide in water (containing some oxidizer) exposes more Ge for further oxidation until complete dissolution of the Ge sacrificial layer occurs[114,115].

In brief, our process is as follows: A thin layer of germanium is first patterned. The entire surface (containing germanium and non-germanium coated surfaces) is then functionalized and the germanium is then dissolved away, leaving biomolecules only on the surfaces that originally were uncoated by germanium. The whole process is scalable and easy to apply in any microfabrication lab, as it relies on standard thin film techniques. In addition, germanium and its dissolution products are biocompatible, which enables the use of this technique for both *in vitro* and *in vivo* devices[117].

In this chapter, we report protein patterning results from two different Ge deposition processes, E-beam evaporation and low temperature chemical vapor deposition (LPCVD). Since E-beam evaporation is more directional (more material deposited on horizontal surface than on vertical sidewalls) and LPCVD is more conformal (same film thickness on both vertical and horizontal surfaces), LPCVD protects vertical walls from biomolecule attachment while E-beam evaporation enables sidewall functionalization, which is a topic of recent interest[118]. Both biotin and streptavidin surface activity were characterized with various incubation periods in 0.35% H_2O_2. To our knowledge, this study is the first demonstration of protein nanoarray fabrication with Ge as a sacrificial layer.

2.3 Experimental Methods

2.3.1 Fabrication

Substrate features were first patterned onto p-type silicon wafers by conventional photolithography techniques. Deep ultraviolet (DUV) photoresist (Dow UV210-0.6) was spun at 7000 rpm for 420 nm final thickness, exposed in ASML 5500/300, developed in MF26A for 1 min and hard baked for 2 h at 120^{o}C (all DUV photoresists were patterned with these conditions unless otherwise indicated). Wafers were then etched in a Lam TCP 9400SE Etcher to provide 120 nm-deep alignment markers, which enabled alignment of protein patterns with substrate features in subsequent germanium patterning. In this chapter, we etched 500 nm deep square wells into the substrate in a Lam Etcher system to demonstrate alignment accuracy and sidewall functionalization. After well etch, we deposited a layer of high-temperature oxide (HTO) in a TYTAN Diffusion Furnace System at 900^{o}C. HTO was not necessary for our protein patterning technique with a Ge mask, but provided a blank surface with binding sites for silane chemistry. If other surface chemistries are used, the HTO step can be skipped and the Ge process applied after substrate fabrication.

There are two Ge fabrication methods presented in this chapter (Fig 2.1). In method 1, we used an E-beam evaporation and lift-off process to pattern Ge. DUV photoresist (Dow UV210-0.6) was spun at 1480rpm to form a 900nm sacrificial layer and patterned to cover the areas to be functionalized.

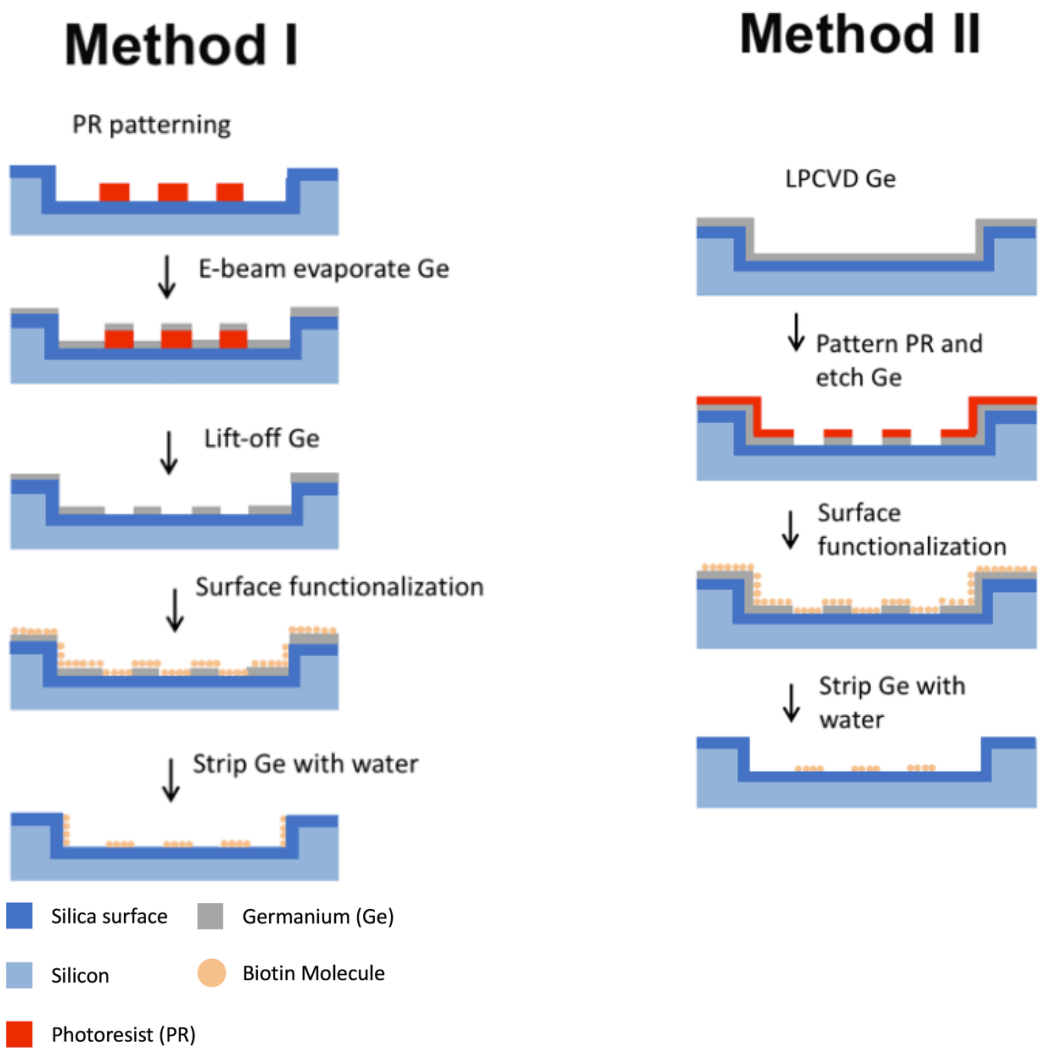

Fig 2.1 Fabrication process overview.
Left) 50 nm Ge layer is patterned with E-beam evaporation and a lift-off process. Vertical sidewalls are functionalized along with horizontal openings. Right) 50 nm Ge layer is patterned with LPCVD and etching. Vertical sidewalls are completely covered and not exposed to functionalization solution. After Ge patterning and surface chemistry, Ge layer is dissolved in 0.35% H_2O_2 and the chip is ready to use.

In this work, we patterned micron scale squares inside the previously etched square wells as a demonstration. 50 nm thick germanium was evaporated on top of the patterned photoresist in

a CHA E-beam Evaporator at 10^{-6} Torr base pressure. The surface conjugation areas were then exposed by stripping photoresist in 1-methyl-2-pyrrolidone (NMP). In method 2, we deposited Ge first with LPCVD and then etched away Ge in surface functionalization areas. 50 nm thick germanium was deposited in a TYTAN Diffusion Furnace System at 340°C after depositing a layer of 2 nm amorphous silicon as an adhesive layer between HTO and Ge. Then, 420 nm DUV photoresist was patterned over the germanium. Germanium exposed through the photoresist was completely etched away in a Lam TCP 9400SE Etcher to open windows for protein patterning in the next step. The plasma etching of germanium had high selectivity against HTO so that HTO also worked as a stop layer during germanium etching. After Ge patterning with either method, we brought the substrates in contact with 25 mg/ml silane-PEG-biotin (Nanocs, New York, NY) in ethanol or dimethyl sulfoxide (DMSO) and incubated for 30 min at room temperature. After washing away excess silane solution, wafer substrates were immersed in deionized (DI) water with 0.35% hydrogen peroxide to strip Ge. After the dissolution of germanium, wafers with biotin patterns were washed in DI water and blown dry with nitrogen, followed by storage in a 4°C fridge for future use.

2.3.2 Ge dissolution

Germanium dissolution rate as a function of H_2O_2 concentration, temperature and pH had been well characterized in literature[119]. For the first Germanium dissolution test in Fig 2.2, germanium films of 2 nm thickness were E-beam evaporated (as per *Fabrication*) on silica chips. Kapton tape was used to cover some chip area (leaving the center exposed), in order to provide enough contrast between Ge and non-Ge areas. Four circles were drilled around Ge deposited area, so that we could identify the Ge area even after complete dissolution. Ge deposited silica chips were then immersed into pure DI water, DI water with 0.35%w/v hydrogen peroxide, NMP, IPA, acetone, DMSO and ethanol for 10 min, 30 min, and overnight to test the dissolution rate in different solutions.

For the dissolution test in Fig 2.3, we fabricated as following. Before surface conjugation with silane chemistry, dissolution of Ge was tested in 0.35% H_2O_2 and surfaces were imaged with a Gemini Scanning Electron Microscope (SEM) before and after dissolution. Substrates were first patterned with 25 μm by 25 μm square wells that were etched 500 nm deep, followed by 100 nm HTO deposition. A layer of 50nm Ge was deposited in an LPCVD furnace and 3 μm by 3 μm squares were etched inside the square wells. The etching recipe had a 20 s overetch after the 50nm Ge etch to ensure all Ge and amorphous Si on top of the HTO was etched away. Substrates were then imaged in SEM to identify the Ge surface versus oxide surface. After immersion in 0.35% H_2O_2 for either 10 min or overnight at room temperature, substrate surfaces were imaged by SEM again to characterize the surface after Ge dissolution. It was very easy to distinguish oxide from Ge in SEM, since the oxide surface was smoother and brighter than the Ge surface which had micron-size grains.

2.3.3 Labeling patterned biotin with fluorescent streptavidin

Prior to functionalization, 25 μm by 25 μm and 42 μm by 42 μm square wells were etched 500 nm deep into the silicon wafer, followed by 100 nm HTO deposition. All samples were

separated into two groups. Group 1 and 2 were fabricated and functionalized using Method 1 and 2, respectively (Fig 2.1). 3 μm x 3 μm and 5 μm x 5 μm squares patterned inside 25 μm x 25 μm and 42 μm x 42 μm square wells (16 squares per well) were biotinylated using silane-PEG cross linker (see *Fabrication*). Wafers were then incubated with 1% bovine serum albumin (BSA) blocking solution for 1 hour at room temperature to prevent nonspecific binding. Streptavidin conjugated with Alexa-Fluor 647 (Strep-647) was used to fluorescently label the biotinylated surface by incubating 10 μg/ml Strep-647 in 1X PBS with substrate surfaces for 30min at room temperature, after which Ge was removed by 10 min-immersion in 0.35% H_2O_2 with mild stirring. Since Ge is dissolved after Strep-647 labelling, it was not strictly necessary to incubate in blocking solution; the step was carried out to be certain that Strep-647 bound to biotin specifically (as streptavidin is known to bind nonspecifically to surfaces). We did not find significant signal decrease due to oxidation in H_2O_2, so all Strep-647 labeling was done before Ge dissolution (with the exception of the experiment to test biotin activity in H_2O_2). Fluorescent images were taken using a Nikon Eclipse Ti fluorescent microscope after washing and blowing dry.

2.3.4 Protein Nanopatterning

The resolution of proteins patterned with Ge hard masks was limited by the photolithography process and exposure tools. In order to show that the limit was attributable to lithography limits, we pushed the resolution of our protein patterning down to 250 nm, the limit of our ASML model. For this experiment, 500 nm deep square wells were not etched before HTO deposition, since a 500nm height difference disrupted the uniformity (even distribution of photoresists) of DUV photoresist coating (420 nm thick) and affected submicron lithography. Thus, protein nanoarrays were fabricated on flat silicon wafers with 100 nm HTO and Method 2 was used to pattern 50 nm Ge film with 1 μm x 1 μm, 500nm x 500nm, 300nm x 300nm and 250nm x 250nm openings for conjugation. Biotinylation of nanoarrays was performed as per *Fabrication*. Strep-647 was then used as described above to label biotin molecules on the surface. Fluorescent images were taken with a Carl Zeiss Elyra SR.1 Super Resolution Microscope in order to resolve the 250 nm squares.

2.3.5 Stability testing of streptavidin and biotin after incubation in diluted H_2O_2

As the concentration of H_2O_2 used for Ge dissolution was very low, both biotin and streptavidin surface exhibited sufficient activity for the following experiments. Biotin-conjugated chips were fabricated as above. Biotin activity was demonstrated by incubating biotin conjugated chips in 0.35% H_2O_2 for various periods from 10 to 360 min at room temperature. For streptavidin-activity tests, biotin conjugated chips were first incubated with 100ug/ml non-fluorescent streptavidin solution for overnight to get streptavidin surfaces. Streptavidin conjugated chips were immersed in 0.35% H_2O_2 for different incubation periods as per biotin groups. (Note, sufficient H_2O_2 solution and a sealed the container should be used for long incubations to prevent drying. If the H_2O_2 solution dries or too much water evaporates during incubation, neither biotin nor streptavidin survive). After H_2O_2 incubation, biotin and streptavidin chips were blocked in 1% BSA for 1h at room temperature before brought in contact with Strep-647 and Atto-488 Biotin

(Biotin-488), respectively. Fluorescent images were then taken with a Nikon Eclipse Ti fluorescent microscope after washing and blowing dry.

2.4 Results & Discussion

2.4.1 Germanium dissolves in diluted H_2O_2 rapidly but not in organic solvents

Germanium dissolves easily in aqueous solution but not organic solutions. As shown in Fig 2.2, brown areas indicated by black arrows are areas deposited with 2nm Ge, which dissolved completely in pure DI water and water with 0.35% w/v H_2O_2 in 30 min and 10 min respectively, but did not dissolve in any organic solvent after an overnight incubation at room temperature. Note, the Ge dissolution rate in 0.35% H_2O_2 is higher than 2nm per 10min. This experiment was to demonstrate the different dissolution rates of Ge in different solvent solutions qualitatively and to prove the feasibility of using Ge as a sacrificial layer for protein 'lift-off'.

Germanium dissolved completely in 0.35% H_2O_2 at room temperature. As shown in Fig 2.3 A&B, each 25 μm x 25 μm well had sixteen 3 μm by 3 μm squares for functionalization. The exposed oxide area was smoother than the Ge layer, for which micro-scale grains were evident. After 10 min incubation in 0.35% H_2O_2, it was very clear that all Ge grains were completely removed and overnight incubation didn't remove more material (Fig 2.3 C&D). Any residual Ge on the oxide surface would be very obvious in SEM. Thus, a 10min incubation in 0.35% H_2O_2 was sufficient to remove a 50nm Ge sacrificial layer. After Ge dissolution, 3 μm by 3 μm squares were still visible under SEM (Fig 2.3 C&D). This arose because the additional over-etch step in the Ge etching process etched away the 2 nm Si layer in those 3 μm by 3 μm conjugation regions, while the 2 nm Si layer elsewhere did not dissolve in H_2O_2 during Ge dissolution.

As Strep-647 was dissolved in 1X PBS, the germanium layer oxidized and dissolved slowly during the 30min labeling process. The Ge dissolution rate in 0.35% H_2O_2 was accelerated if done after a 30min incubation in PBS. Importantly, a 30min incubation in PBS was insufficient to dissolve a 50 nm Ge layer. The germanium did not exhibit appreciable etching until 0.35% H_2O_2 was added. This is evidenced by the low background intensity in Fig 2.4 as the intensity of the unconjugated area was not higher than that of a blank silicon wafer. On the other hand, the Ge surface integrity was less important since a biotin pattern was formed on chip surface during the silane chemistry step. Even if the Ge layer completely dissolves before streptavidin conjugation, streptavidin should only be immobilized on biotin surfaces. Thus, after biotin conjugation, Incubating chips in aqueous solution is not a problem.

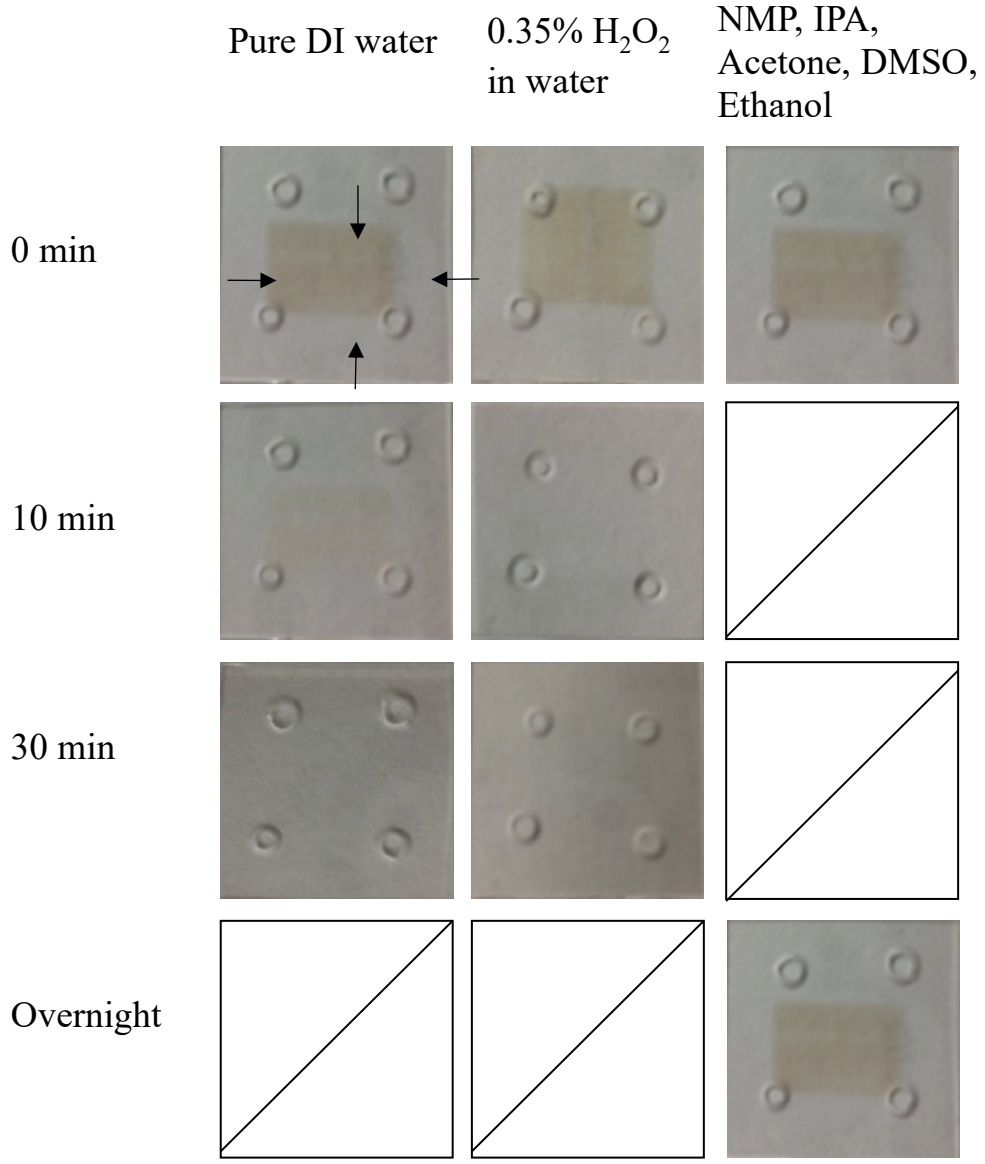

Fig 2.2 Germanium dissolution test.
Silica chips with 2nm thick Ge layer were incubated in different solutions at room temperature for 10min, 30min and overnight.

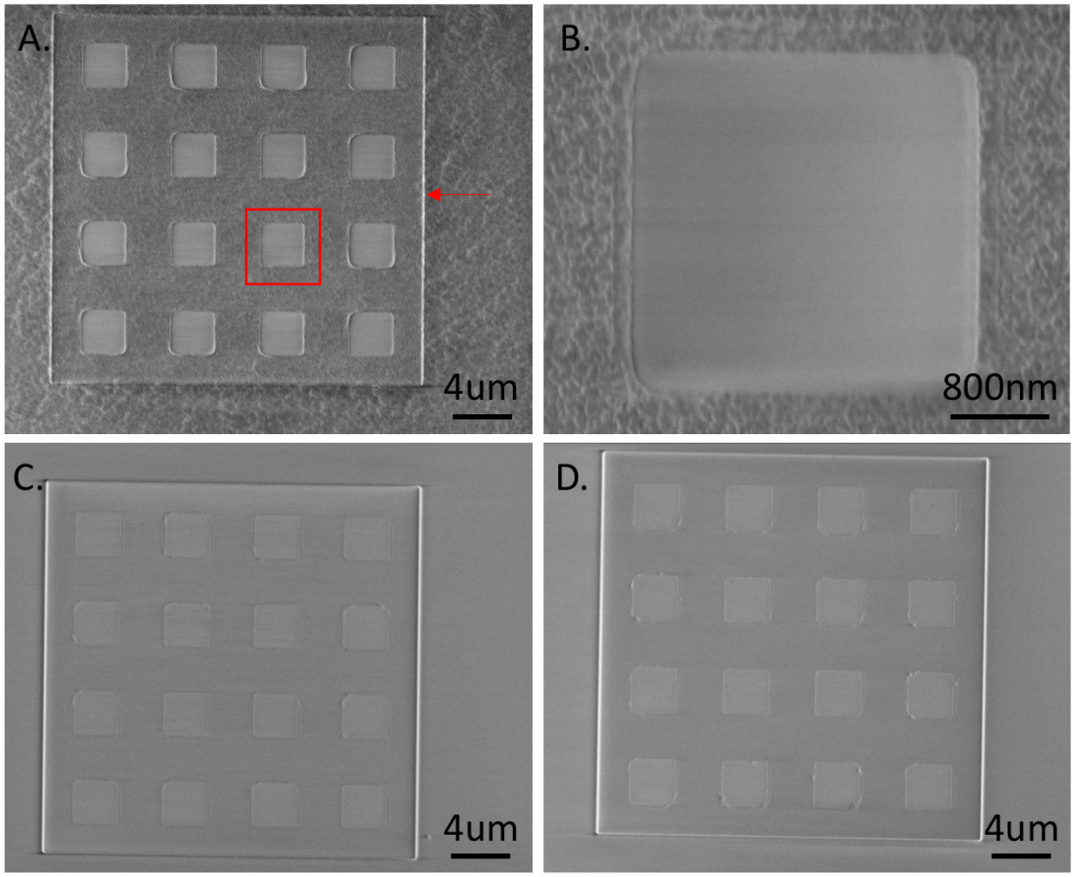

Fig 2.3 Germanium dissolution.
A) SEM image of 50 nm Ge films deposited by LPCVD before dissolution. Red arrow indicates the edge of a 25 μm by 25 μm square well, etched 500nm deep. B) Higher magnification of red box in A). C&D) SEM images of Ge layers after 10min C) and overnight D) incubation in 0.35% H_2O_2 at room temperature. Ge was completely dissolved in 10min with no residues left. Faint square outlines are due to the over-etch process in the Ge etching recipe and thus the adhesive amorphous Si layer between Ge and HTO is etched away.

2.4.2 Nanoscale patterning is achieved

All biotinylated regions were successfully conjugated by fluorescent streptavidin. The results for both Ge patterning techniques, Method 1 & 2, are shown in Fig 2.4A&B, respectively. The fluorescent sidewalls in Fig 2.4A pointed out by red arrows indicate sidewall conjugation (in contrast to Fig 2.4B, which did not exhibit this). The intensity profiles along yellow dash lines in Fig 2.4 A&B are shown in Fig 2.4C&D respectively. Four major peaks represent 4 squares labeled with fluorescent streptavidin. There are two additional little peaks caused by sidewall conjugations on each side of the 4 major peaks, highlighted with red arrows in Fig 2.4C. These additional intensity peaks have much lower intensity than the major peaks, but still high enough to be

distinguished from background, which are however not exhibited in Fig 2.4 D at all. This sidewall conjugation arose because of the non-conformal deposition of Ge evaporation: evaporated ultrathin Ge films (e.g. 50 nm) covered only horizontal surfaces and left vertical sidewalls exposed for biotin conjugation. In contrast, LPCVD Ge films of the same thickness protect vertical sidewalls from surface chemistry.

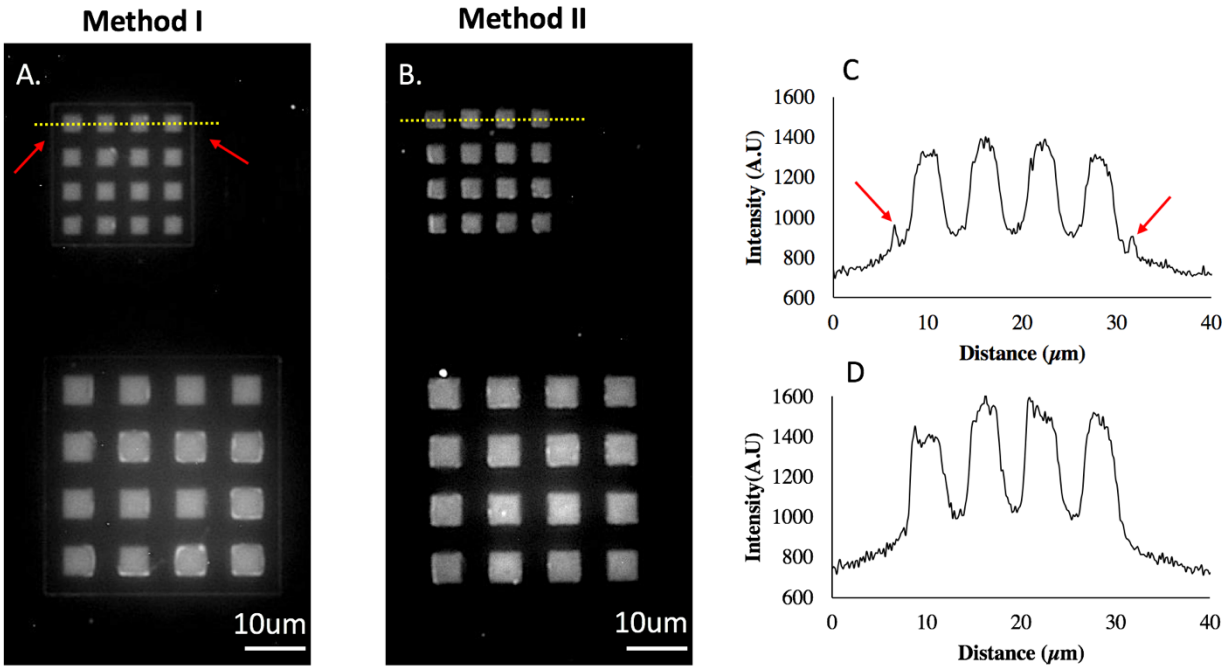

Fig 2.4. Sidewall coverage depends on how conformal the deposition process is.
Biotin microarrays were generated by either Method 1 (A) or Method 2 (B) illustrated in Fig 2.1 Strep-647 was then used to label biotinylated surfaces. Sidewall conjugation is shown in A) pointed out by red arrows but not in B) due to the higher conformal deposition of LPCVD (B) vs. E-beam evaporation （A）. Intensity profiles along the yellow dash lines in A) and B), are shown in C) and D) respectively. Red arrow in C) correspond to the side wall intensity labeled by the red arrows in A). Any misalignment between conjugated regions and wells was too small (<100nm) to measure with our fluorescent microscopy.

The use of modern deep ultraviolet (DUV) lithography enabled nanoscale protein patterning. As shown in Fig 2.5, all features ranging from 250 – 1000 nm were successfully resolved and conjugated with biotin. No nonspecific binding was evident. The feature rounding on smaller features was an artifact of submicron lithography.

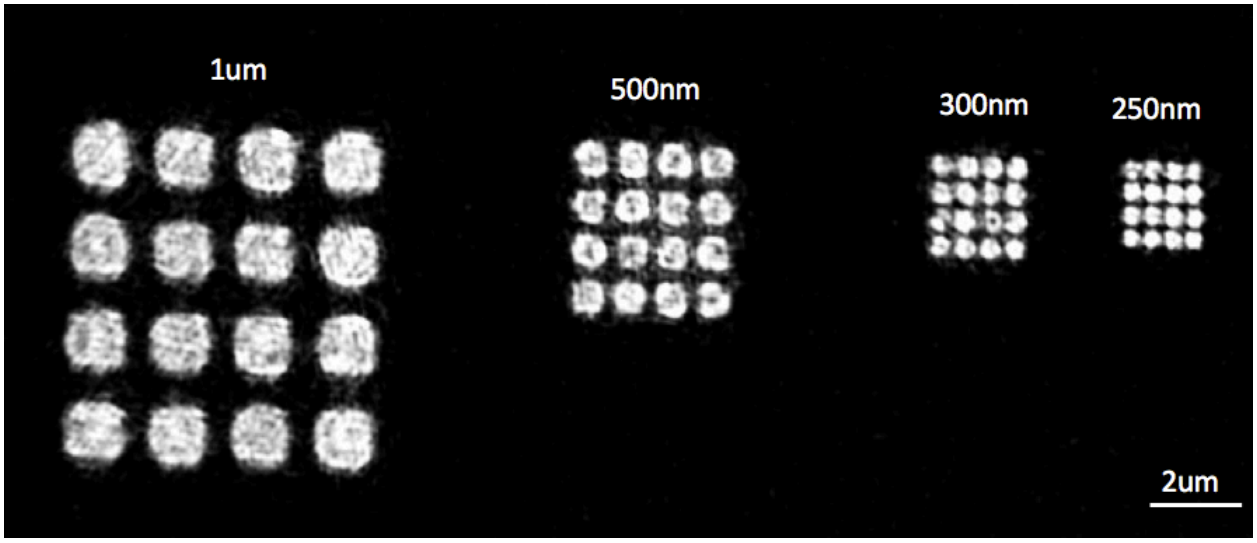

Fig 2.5. Nanoscale protein patterning.
Submicron squares were patterned with biotin and then labeled with strep-647. From left to right the squares have 1 µm, 500 nm, 300 nm and 250 nm sides, respectively; 250 nm is the resolution limit of the lithography tool. The inhomogeneity of fluorescent signal was most likely caused by the nature of super-resolution fluorescent imaging.

2.4.3 Both biotin and streptavidin can maintain the activity after Ge dissolution

Both biotin and streptavidin could maintain activity after H_2O_2 incubation, as shown in Fig 2.6. The activity was measured in terms of the number of fluorescent biotin or streptavidin molecules bound on streptavidin and biotin surfaces, respectively. Thus, the fluorescent intensity was proportional to the remaining activity of the surface molecule. With 10min 0.35% H_2O_2 incubation, both biotin and streptavidin showed ~80% activity. Even after immersing in H_2O_2 for 6h, biotin and streptavidin surface still had more than 50% activity remained. Longer incubation was not required for 50nm Ge dissolution; here the longer incubation periods were used to show biotin and streptavidin stability in H_2O_2 in case a longer incubation was needed for other applications.

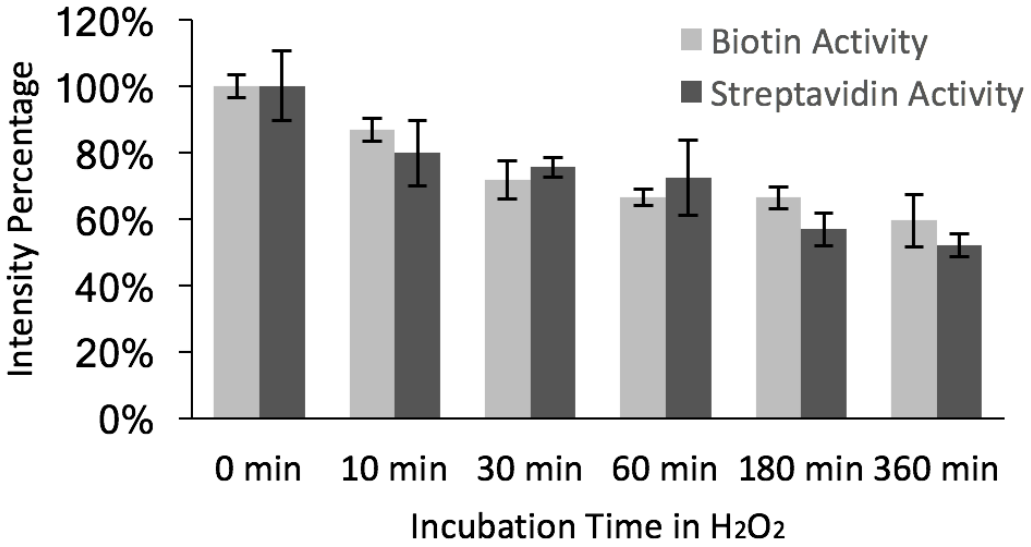

Fig 2.6. Biotin and streptavidin activity after H_2O_2 incubation.
Microarrays were fabricated and conjugated with biotin as per Method 2. Streptavidin conjugated chips were obtained by incubating biotin conjugated chips with 100ug/ml non-fluorescent streptavidin solution overnight. Both biotin and streptavidin conjugated chips were then incubated in 0.35% H_2O_2 for 10min, 30min, 60min, 3h and 6h at room temperature. After H_2O_2 incubation, all chips were blocked in 1%BSA. Biotin chips were then labeled with 10ug/ml Strep-647 while streptavidin chips were labeled with 1ug/ml Biotin-488. Intensity was normalized by using control group (0min) as 100% intensity.

2.5 Conclusion

In this work, we demonstrate the use of germanium sacrificial layers to achieve biomolecule patterning which is compatible with nano/microfabrication, scalable to high resolutions with precise alignment, and ultimately suitable for low cost and high volume manufacturing of biosensors. In addition, the method is applicable to a wide range of biomolecules and surface chemistries. It is of particular utility for surface conjugation chemistries which require organic solvents. Examples include the commonly used primary amine reactive chemical groups for protein labeling, such as N-hydroxysuccinimide ester (NHS), which hydrolyzes quickly in water and the conjugation of proteins onto silicon dioxide surfaces using silane-PEG-NHS. Because both functional groups hydrolyze in water, organic solvents are usually required and a germanium sacrificial layer would be of significant use.

Two processes are reported in this chapter, each of which has specific advantages. Method 1 uses evaporation and a lift-off process to pattern the Ge hard mask. This process avoids the high temperature deposition process of Ge and the aggressive etching process in Method 2. For LPCVD processing, all wafers must be cleaned in piranha and hydrogen fluoride (HF). This mandates that

there be no organic materials on substrate, which is often not the case for biosensor applications. Since Method 1 uses a lift off technique instead of etching, there is no need to have a stop layer (such as the HTO layer in our case) which is compatible with both the surface chemistry and the etching process. Thus, Method 1 is compatible with low-melting-point biomaterials underneath the Ge layer. We demonstrated nanoscale protein patterning only with Method 2. This is due to lift-off process in Method 1 requiring submicron pillars, which are much harder to resolve than submicron openings with positive photoresists. If an appropriate negative photoresist is available, Method 1 can also be used to resolve nano-features. Furthermore, sidewall functionalization can be achieved and controlled by using a non-conformal Ge deposition process (as in Method 1). On the other hand, the Ge film in Method 2 is much more uniform over the whole surface due to the conformal LPCVD process. It can successfully avoid protein immobilization on sidewalls, which may be preferred for some biosensor applications.

This work employed biotin/streptavidin conjugation to demonstrate the germanium sacrificial proof of concept; both biotin and streptavidin surfaces were stable enough to maintain activity after 0.35% H_2O_2 incubation. We also used streptavidin as an example of the method's use for protein patterning. Of note, streptavidin can be directly used as a cross linker to immobilize biomolecules. For example, after Ge dissolution, a protein can be immobilized on a biotin surface by conjugating a target protein with streptavidin first. Alternatively, streptavidin can be immobilized onto the surface first to capture biotin conjugated proteins onto the surface after Ge dissolution. We believe this method could have wide applicability across a variety of protein patterning applications.

In this chapter, we successfully demonstrate a new method to conjugate biomolecules onto the surfaces in microfluidic channels, which is useful for microfluidic-based immunoassays. However, as we discussed in Chapter 1, we need to enrich target molecules to enhance the sensitivity and speed of immunoassays. Thus, we introduce an ICP-based preconcentrator in Chapter 3 as well as the process about how we developed from the single-nanochannel design on silica substrates to the multi-nanochannel design on silicon substrates.

Chapter 3：Silica-based ICP preconcentrator with single/multiple nanochannels

3.1 Introduction

As we discussed in Chapter 1, the rate-limiting step for the detection of low-concentration analytes is the analyte transport to the biosensors. Thus, preconcentrating analytes to accelerate the analyte capturing without compromising the sensitivity becomes a heated topic.

This chapter discusses the development of preconcentration devices on silica and silicon substrates. It explains how we started with single-nanochannel preconcentrator on silica substrates and then switched to multi-nanochannel design with deeper etching.

Two different fabrication processes for nanochannels were demonstrated on silica substrates: e-beam lithography and deep-UV (DUV) lithography followed by oxide deposition. The latter was chosen for our project because it has higher throughput and results in a cleaner surface, which is better for sealing afterwards. After fabricating the preconcentrator with a single 30 nm-wide nanochannel, we applied DC voltage across the preconcentrator to demonstrate the ion concentration polarization (ICP) based protein enrichment in front of that single nanochannel.

One single vertical nanochannel is, however, unable to accumulate protein molecules fast enough for highly sensitive immunoassay due to the low volumetric flow rate in the microchannel. We also report two additional strategies in this chapter to enhance the accumulation of protein molecules, 1) increasing the number of nanochannels per microchannel and 2) increasing the depth of nanochannels. Both of these two strategies provide higher volumetric flow rate and carry more protein molecules to the enrichment zone in the same period of time.

In order to increase the depth of nanochannels, we had to switch from silica substrates to silicon substrates, since DRIE for silica substrate was not available in our lab. Besides the fabrication challenges, we also attempted to immobilize proteins on the surfaces in front of the nanostructures. However, we found the drying process would deactivate antibodies, so we switched to bead-based immunoassays, as described in the next chapter.

3.2 Methods

3.2.1 Design of single-nanochannel devices

The first single-nanochannel preconcentration device is fabricated on a silica substrate and has two main parallel channels connected by nanochannels (Fig 3.1a). The main channels are 3μm deep, 3 mm wide and around 1 cm long. As shown in Fig 3.1b, there are three microchannels connecting two main channels. Each microchannel is approximately 200 μm long, 30μm wide and 300 nm deep and has a ~30nm wide, ~1 μm long and 30 nm deep nanochannel in the middle (Fig 3.1c). We chose to etch 300 nm deep for microchannels instead of using the same depth as the main channels because deep reactive ion etching (DRIE) was not available for silicon dioxide in our lab. The RIE tool requires a lot of parameter tuning or testing to provide a relatively higher aspect ratio. For example, in the e-beam lithography method, if we wanted to fabricate 3 μm deep channels, then the aspect ratio for nanochannel etching would be 100:1 (3 μm deep and 30nm wide).

Tubing and electrodes are connected through four reservoirs (two for each main channel). To apply DC voltages, the left main channel is connected to the anode, and the right channel is connected to the cathode during analyte preconcentration. The finished devices are sealed with another silica wafer (or coverslip, in the case of sealing a chip), with PSQ as the adhesive layer after oxygen plasma. For tubing purposes, a layer of PDMS with 4 through-holes is covalently bonded to the back side of the silica wafer with structures. The through-holes were used to form connections with rubber tubes and electrodes.

3.2.2 Fabrication process of single nanochannel devices

We proposed two fabrication processes for nanochannels: 1) E-beam lithography(Fig 3.2a) and 2) Deep-UV (DUV) followed by oxide deposition(Fig 3.2b). Both of the nanochannel fabrication processes are shown in the schematic cross-section along the orange dashed line in Fig 3.1b, while Fig 3.2 demonstrates the fabrication process for nanochannels only, and Fig 3.3 shows the complete fabrication process.

In the first method with E-beam lithography, the 300 nm deep microchannels connecting two main channels were patterned with DUV lithography with ASML 5500/300 (ASML, Veldhoven, Netherlands) followed by Reactive Ion Etching (RIE) in an inductively coupled plasma etcher (SPTS Technologies, Newport, UK). In this step, the left and right halves of the microchannels were 1 μm away from each other and not connected yet. Fig 3.2a only shows the cross-section of the nanochannel fabrication process, so these steps are not demonstrated in Fig 3.2a.

Subsequently, the 30 nm nanochannel was fabricated with E-beam lithography on top of the microchannels to connect the left and right in the middle. For E-beam lithography, Poly(methyl methacrylate) (PMMA) was used as a high resolution resist, so 2% PMMA (495,000 g/mol) in anisole was first spin-coated on the silica wafer to form a 100 nm thick resist layer. Since the substrate was an insulator (silica), electrons could not be dispensed efficiently, which would

significantly lower the resolution of E-Beam lithography. Thus, a 20 nm thick layer of conductive polymer (ESPACER, Showa Denko, Japan) was spin-coated on top of the PMMA layer to avoid electron accumulation under the electron beam. Then the silica wafer (or diced silica chip) was exposed in Crestec (CABL-9510CC Electron Beam Lithography System) to direct-write the 30 nm wide nanochannels.

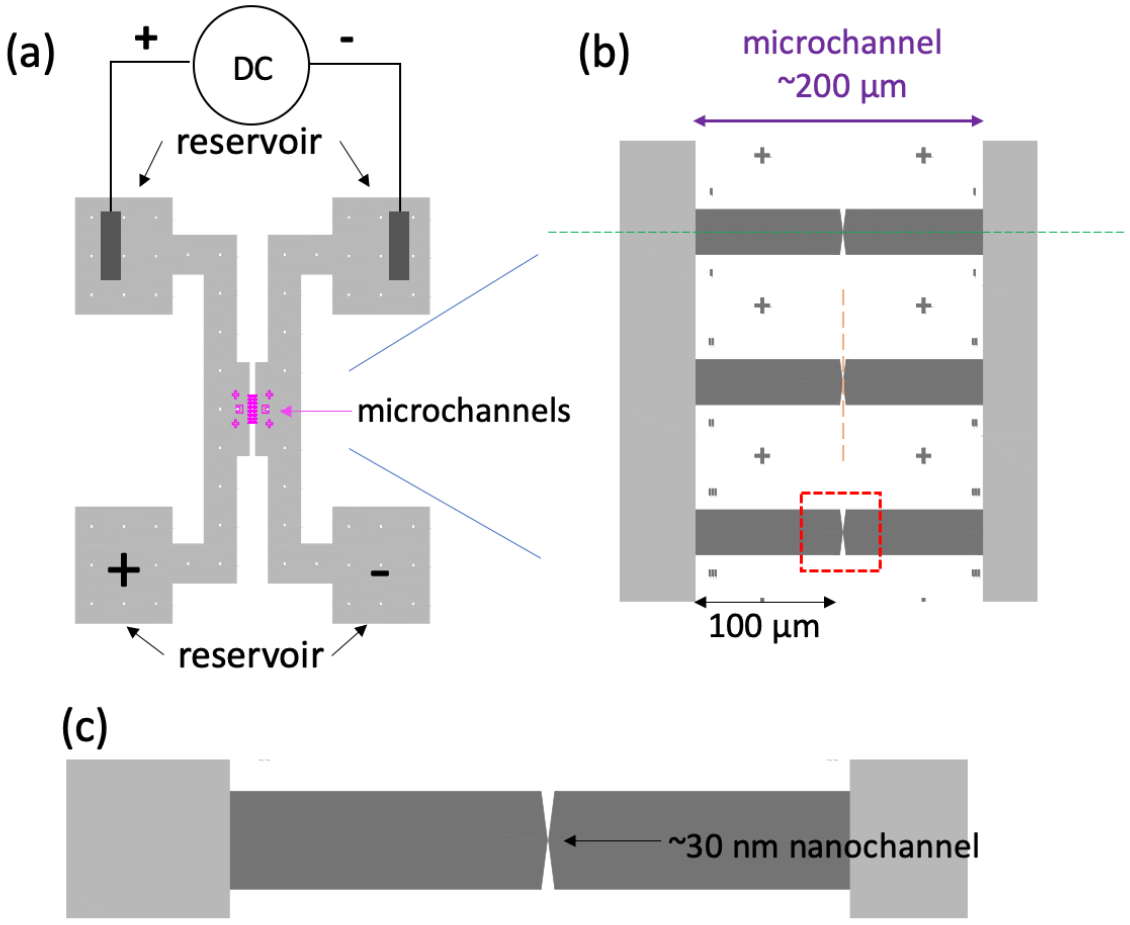

Fig 3.1 Overview of the single-channel nanofluidic device.
(a) Schematic diagram of the entire device. There are two main channels connected by microchannels. Each main channel has 2 reservoirs, connecting to external fluidic tubing and contacting with electrodes. Each microchannel has 1 nanogap for analyte enrichment. (b) Close-up of the microchannels connecting two main channels. These microchannels are 100 µm long on each side of the nanogap, 30 µm wide and 300 nm deep. The nanogap in each microchannel is around 30 nm wide. (c) Close-up of the microchannel in (b).

After the E-beam writing in Crestec, the conductive polymer was washed away in water, and the PMMA was developed in the 1:3 MIBK: IPA developer. After development, the same RIE tool was used again to etch the nanochannels 300 nm deep. Finally, the residual PMMA was

removed using Remover PG (MicroChem, Westborough, MA), although this PMMA removal process was not very successful (see *Results and Discussion*). Note that the main channels fabrication is not included in this process, since the nanostructure was never successfully fabricated with e-beam lithography.

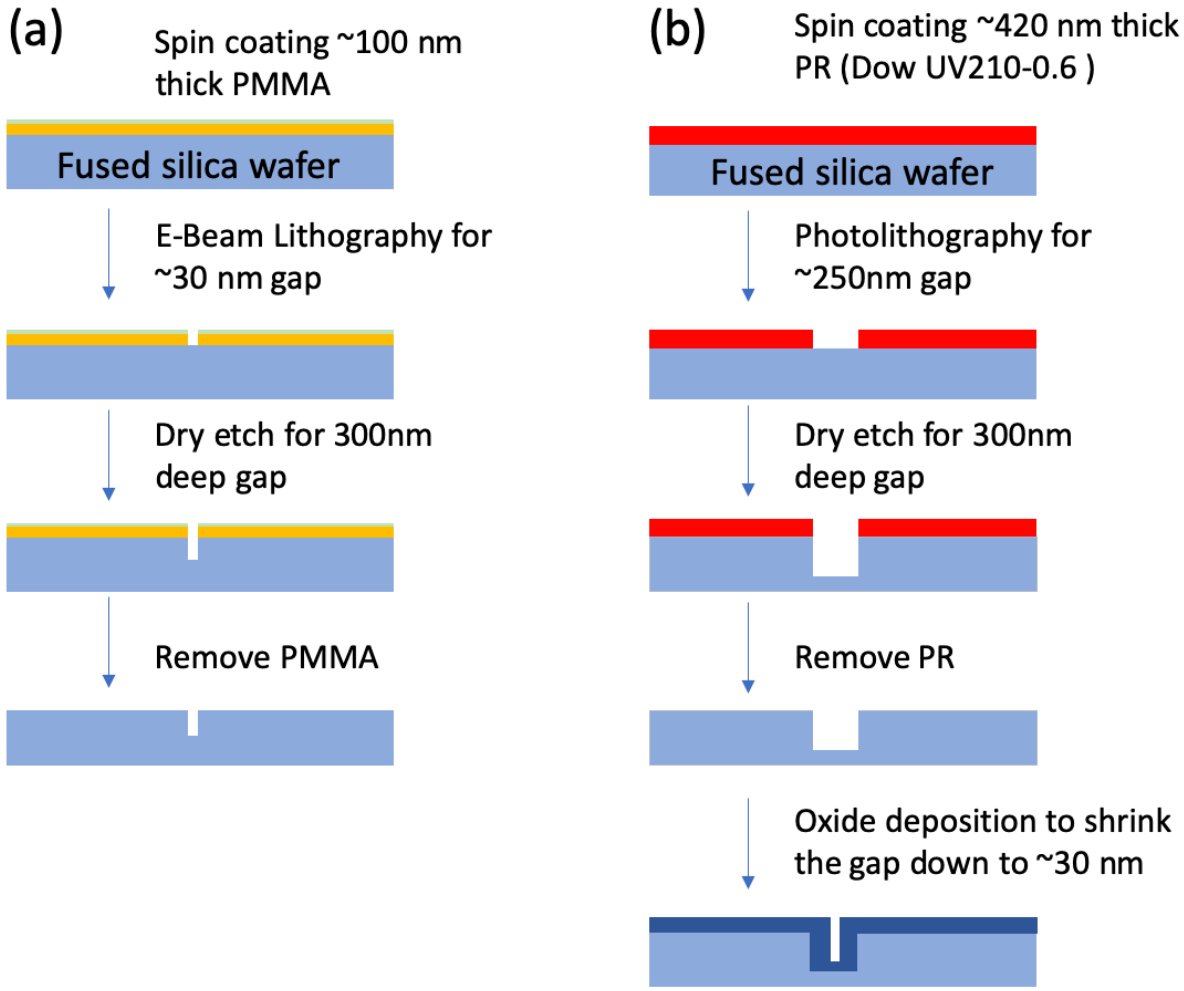

Fig 3.2 Two strategies for nanogap fabrication.
(a) E-Beam lithography process. Since the device was based on a silica wafer, in order to dissipate the charge accumulated on the surface during E-beam Lithography, an additional conductive layer, E-SPACER 300Z (light green) was spin-coated on top of the positive resist, PMMA (orange). (b) Photolithography with oxide deposition process. Both processes are shown with the schematic cross-section at the orange dashed line in Fig 3.1b.

Besides E-Beam lithography, we also proposed to fabricate nanochannels ~250 nm wide and ~300 nm deep with DUV and RIE on silica substrates, followed by an oxide deposition to shrink the nanochannel width from 250 nm down to ~30 nm (Fig 3.2b). The whole process of the chip is shown in Fig 3.3.

First, the microchannels with a ~250 nm nanochannel in the middle of each microchannel were fabricated on the silica wafer. A 50nm layer of Cr was deposited on the back side of the silica wafer because both the spin-coating tool and exposure tool required an opaque substrate. Then, a ~60 nm thick layer of anti-reflective coating (AR3-600) was applied before a 420 nm thick layer of DUV photoresist (UV210-0.6, Dow Chemical, Midland, MI) was patterned on the front side of the silica wafer.

The microchannels and nanochannels were then etched ~300 nm deep with RIE in an inductively coupled plasma (ICP) etcher (SPTS Technologies, Newport, UK). The residual photoresists were removed using an oxygen plasma asher (Matrix Plasma Asher Model 106), followed by piranha cleaning at 120 ºC for 10 min.

After fabricating the micro-/nanostructures, the main channels were fabricated with a similar process, except that a thicker layer of DUV photoresist (~900 nm) was used. It was critical to pattern the ~300 nm deep microchannels before the main channels because the 3 μm tall side walls of the main channels would disturb the spin-coating process of ~420 nm photoresist for microchannels, while the ~900 nm thick photoresist could be coated fairly well on top of ~300 nm tall side walls without compromising the resolution.

After all features were etched, we deposited a layer of high-temperature oxide (HTO) at 900ºC with a TYTAN Diffusion Furnace System (Tystar, Garden Grove, CA) to reduce the nanochannel size from ~250nm to ~30nm. Four reservoirs were then ground manually with a dental drill to create access holes through the silica substrates after spin-coating a 10 μm thick layer of photoresist (SPR 220-7.0, Dow Chemical, Midland, MI) for surface protection. Since silica is relatively hard to etch (due to its slow etching rate), it takes hours to etch through-holes on silica surface. Thus, we chose to ground through-holes manually, which was quicker in the scale of prototyping (one or two wafers per batch).

After fabricating all the features on the silica wafer, we sealed the device with another silica wafer coated with ~100 nm thick polysilsesquioxane (PSQ, Gelest, Morrisville, PA) as shown in Fig 3.3. We adapted the similar process reported by Gu et al [120,121]. In short, the PSQ was diluted in xylene (2:3) and spin-coated on a plain silica wafer. For a better and more uniform coating, we cleaned the silica wafer with oxygen plasma in YES-G500 Plasma Cleaning System (Yield Engineering Systems, Livermore, CA) at 600W for 2 min. The PSQ-coated silica wafer was then baked in an oven overnight at 150 ºC. The hard-baked silica wafer, along with the silica wafer with all the features, were oxygen plasma treated in YES-G500 at 100W for 1 min.

Oxygen plasma treatment would damage biomolecules' activity. Thus, if biomolecules, such as biotin or antibodies, were immobilized in the microchannels, we only plasma-treated the PSQ silica wafer, while we kept the silica wafer with all the features and bioconjugations dry and clean. A weaker plasma was used in for PSQ layers because high energy plasma might damage

the backbone of PSQ, and therefore reduce the bonding strength. The proper duration was also critical, since long duration of plasma treatment might reduce the effective number of silanol groups via back-biting scission reactions [122].

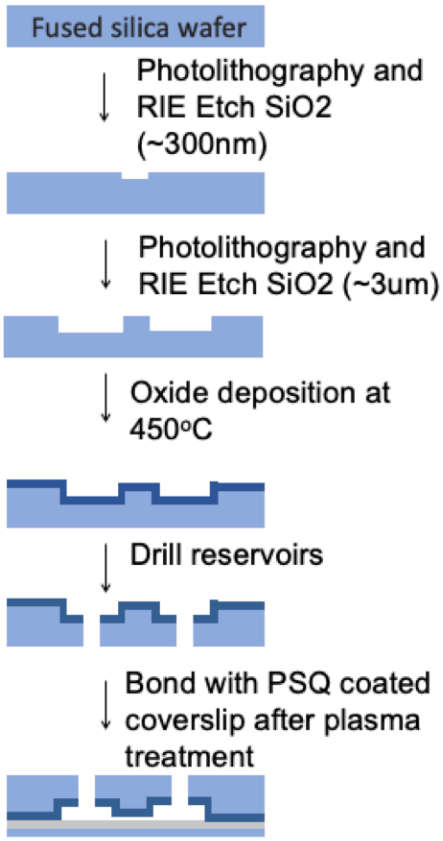

Fig 3.3 Schematic cross-section of fabrication on fused silica at the green line shown in Fig 3.1b.
The microchannels and nanogaps are approximately 300nm deep while the main channels are approximately 3 μm deep. Oxide deposition (LPCVD) was used to shrink the nanogap size from approximately 250 nm to approximately 30 nm. The nanofluidic device was sealed with a PSQ coated silica wafer after oxygen plasma treatment.

After plasma treatment, two silica wafers were brought into contact immediately and additional pressure was applied manually to confirm good bonding. If asymmetric plasma treatment was applied (only the wafer with PSQ was treated), the bonding was weaker than that after symmetric plasma treatment. PSQ has similar bonding chemistry as PDMS, and has been used for sealing processes in microfluidic devices [56,120,121]. However, PSQ has higher strength and is less likely to collapse into our low aspect ratio microchannels (~30 μm x ~100um x ~300 nm). Commercially available PSQ is also more amenable to dilution and spin-coating, since

commercially available PDMS usually has two components and the base solution is too viscous for spin-coating a thin layer.

After sealing, the wafer was diced into chips and ready to use. While using the devices, we could either glue commercially-available tube adaptors onto the through-hole reservoirs or bond another layer of PDMS with four through-holes for tubing connection. Note that Fig 3.3 only shows the complete fabrication process for the second proposed method in Fig3.2b, since the e-Beam lithography approach (Fig 3.2a) was not successful (see *Results and Discussion*).

3.2.3 Conjugating biotin onto the channel surfaces

Since our final goal was to perform immunoassays in this preconcentrator, we tried to functionalize the silica surface with biotin to mimic the antibody-antigen binding in immunoassays. We tried two different surface chemistries. The protein patterning strategy using Ge as a sacrificial layer, described in Chapter 2, was also used to pattern the biotin molecules only in enrichment zone so that the bioconjugation would not affect the sealing steps afterward.

The first conjugation chemistry uses (3-Aminopropyl)triethoxysilane (APTES, Sigma-Aldrich, St. Louis, MO) to provide amine groups on the surface, followed by the treatment with *N*-hydroxysuccinimidobiotin (NHS-Biotin, Thermal Fisher Scientific, Waltham, MA) for biotin conjugation. In detail, 4% APTES in acetone was added onto the Ge patterned silica chips and incubated for 15 min at room temperature, followed by rinsing in acetone, IPA and water. Ge was patterned on the surface, and only the areas near nanochannels were open for bioconjugation as shown in Fig 3.8a1 & b1(Grey boxes indicates the bioconjugation areas). APTES formed covalent bonds with silica surface and provided prime amine for further bioconjugation. Then, 20mM NHS-Biotin in dimethylsulfoxide (DMSO) was added onto the device surface for a 30 min incubation at room temperature. NHS groups in this solution formed covalent bonds with the prime amine groups on the APTES molecules, so the biotin molecules were covalently bound on the silica surfaces after this step. The biotinylated surfaces were washed in water and stored at 4 ^{o}C for further treatment, such as Ge removal in diluted H_2O_2 and sealing steps before use.

The second surface chemistry is similar to the one in Chapter 2, using silane-PEG-biotin (Nanocs, New York, NY), which is a commercially-available crosslinker using PEG as the spacer. On one side of the PEG molecules, there are silanol groups, which can condense with other silanol groups on silica surfaces to form covalent bonds. On the other side of the PEG molecules, there are biotin molecules to provide binding sites for streptavidin. In short, we incubated the Ge patterned substrates with 25 mg/ml silane-PEG-biotin in ethanol/water solution (95% ethanol and 5% water) for 30 min at room temperature. Then, excessive silane-PEG-biotin molecules were washed away with DI water. Note, the 5% DI water in the silane-PEG-biotin solution and the DI water used for washing were not enough to effectively dissolve the Ge layer. Then the biotinylated surfaces were stored at 4 ^{o}C, and the following treatments were the same as above.

3.2.3 Conjugating antibodies onto the channel surfaces

In order to perform protein detection other than streptavidin, we needed to immobilize antibodies (instead of biotin) onto the surface before sealing. The sealing process required the two surfaces to be dry and clean, so we needed to verify that the drying process would not deactivate the antibodies. In this experiment, we used similar surface chemistry as the sections above to conjugate antibodies into microchannels, except that instead of using silane-PEG-biotin, we used silane-PEG-NHS (Nanocs, New York, NY).

First, a silica wafer was patterned with a 50 nm thick layer of Ge. The pattern used here had no relation with our previous device. We reused an old mask to get some openings on the Ge layer. The silica wafers were sliced into chips so that we could perform different experiments on different chips. The silane-PEG-NHS was diluted in ethanol/water solution (95% ethanol and 5% water) to the concentration of 25 mg/ml. The higher concentration of silane-PEG-NHS might lead to a better result. Due to the limited availability of this chemical, we used a lower concentration.

Silane-PEG-NHS solution was added onto the Ge patterned substrates for a 15min incubation at room temperature, followed by rinsing with ethanol and water. Immediately after washing away excessive crosslinkers, antibody solution (500 μg/ml) was added onto the substrates and incubated for 2 hrs at room temperature. The NHS groups on crosslinkers attacked amine groups on the antibodies to form covalent bonds. The processes after silane-PEG-NHS incubation had to be quick since NHS would hydrolyze slowly in water. The antibody we used here was purified rat anti-mouse-IL6 IgG (BD Bioscience, San Jose, CA), commonly used as the capture antibody in sandwich immunoassays. After antibody immobilization, the silica substrates were washed and separated into two groups. One group of silica substrates was kept wet by storing in 1X PBS, while the other group was blown dry to test the effect of the drying process on the antibody activity.

3.2.4 Conjugating antibodies onto microbeads

Since the surface conjugation of antibodies in microchannels were not very successful (see *Results and discussion*). Thus, we also investigated the antibody conjugation on bead surfaces. We used conventional EDC (1-Ethyl-3-(3-dimethylaminopropyl)-carbodiimide, Thermo Fisher Scientific, Waltham, MA) and Sulfo-NHS (N-hydroxysulfoxuccinimide, Thermo Fisher Scientific, Waltham, MA) chemistry to conjugate IgG molecules onto commercially available carboxyl group-coated polystyrene microbeads (~4.6 μm diameter, Spherotech, Lake Forest, IL). First, 0.5% w/v microbeads were mixed with EDC and Sulfo-NHS for 15min at room temperature. We tested different concentration of EDC and Sulfo-NHS (1x: 0.6mg/ml EDC + 1.2mg/ml NHS; 0.02x : 12μg/ml EDC + 24μg/ml NHS) in order to get the optimal conjugation on beads. Then the microbeads were centrifuged and resuspended in DI water with 0.1% Tween-20 to remove unreacted crosslinking molecules. Tween-20 was added to reduce bead aggregation and bead adsorption on centrifuge tubes. These washing steps were repeated for 3 times. Since sulfo-NHS hydrolyzes in water, the washing steps had to be fast. After the last wash, the microbeads were resuspended in 500μg/ml anti-IL6 capture antibody (BD Biosciences, San Jose, CA) solution for 2h at room temperature. After the incubation with the antibody, the reaction was stopped by adding hydroxyl amine (Sigma-Aldrich, St. Louis, MO) into the mixture and incubating for 10 min. Then,

the microbeads were washed for 3 times again. The microbeads were ready to use after blocking in 1% BSA (bovine serum albumin, Thermo Fisher Scientific, Waltham, MA) for 1 hr. The blocking step could significantly reduce unspecific binding. (see *Results and discussion*)

3.2.5 Instruments

An inverted fluorescent microscope (Nikon Eclipse Ti, Nikon Instruments Inc, Melville, NY) was used for all the fluorescent images. The images of enrichment and immunoassays were taken with the anode connected to the left reservoirs and the cathode connected to the right reservoirs. Platinum wires (0.13mm in diameter, A-M System, Sequim, WA) were used as electrodes. The DC voltage from a waveform generator (Keysight, Santa Rosa, CA) was amplified by a fixed gain amplifier (Tegam, Geneva, OH) before applied to the devices. ImageJ was used for all the fluorescent image analysis. A ZEISS Gemini Scanning Electron Microscope (ZEISS, Oberkochen, Germany) was used to image submicron features (EHT=2kV). For contact angle measurement, a drop of DI water was added onto the surface first, and a Kruss Contact Angle Measuring System (Kruss, Matthews, NC) was used to measure the contact angle.

3.3 Results and Discussion

3.3.1 PMMA cannot be removed after RIE

After E-Beam lithography and RIE etch, nanochannels were imaged using a scanning electron microscope (SEM). As shown in Fig 3.4a,b, the silica surface was not clean, and there were many residues left on the surface. These residues compromised the bonding between silica and PSQ surfaces and resulted in leaking.

We hypothesize that these were PMMA residues that could not be removed by organic solvent (Remover PG, MicroChem, Westborough, MA). We tried to remove PMMA by cleaning in piranha solution at 120 ^{o}C for 2 hrs, but piranha could not remove these residues as shown in Fig3.4c. Then, high power oxygen plasma treatment was used for further cleaning. With 30s high power oxygen plasma (~900W), the surface became much cleaner and smoother, although there were still some residues left (Fig 3.4d). Then, the same oxygen plasma cleaning process was repeated for another 5min. PMMA could be removed successfully, but the nanostructure was also sputtered away by oxygen radicals, which in turn enlarged the nanochannels (Fig 3.4e,f).

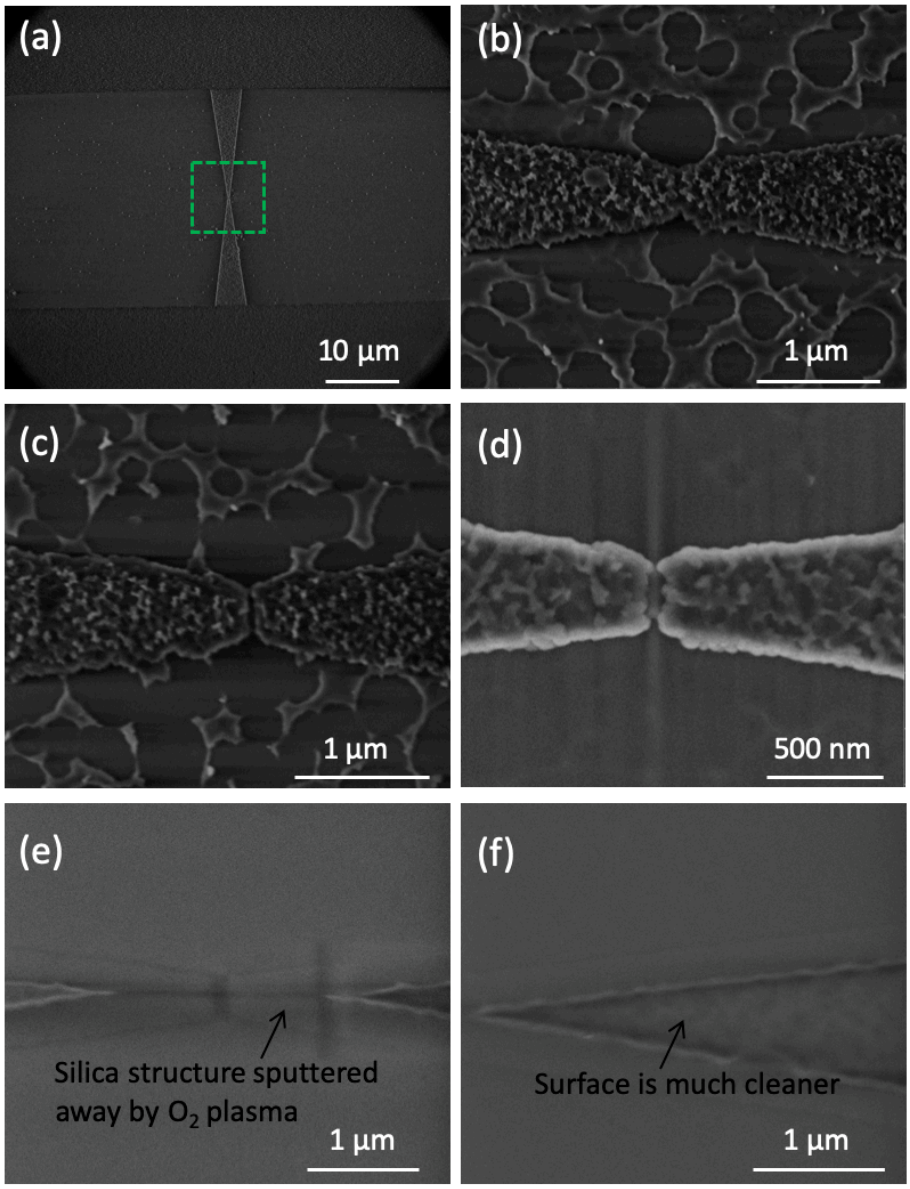

Fig 3.4 SEM of nanogaps fabricated with E-Beam lithography.
(a) SEM of the nanogap, approximately the area highlighted by red box in Fig 3.1b. (b) Close-up of the nanogap in the green box in (a). The surface is not clean and smooth, because there are a lot of PMMA residues left on the surface. (c) SEM of the nanostructure after 2 hrs cleaning in piranha solution at 120°C. The RIE process probably hardened PMMA so that piranha solution could not remove these residues anymore. (d) SEM of nanostructure after high power (900W) O_2 plasma cleaning for 30 s. Short O_2 plasma could partially remove PMMA residues. (e) SEM of the nanostructure after higher power (900W) O_2 plasma cleaning for 5 min. (f) Close-up of the nanostructure in (e). PMMA could be removed successfully by O_2 plasma but the nanostructure was also sputtered away by O_2 radicals. Note that SEM in (a) is rotated 90° compared to the images in (b)-(f).

These results showed that it was less likely that these residues were pure PMMA because it was too hard to remove. It was possible that the oxide RIE process passivated the PMMA residues and laid down a layer of Teflon like material. It was known that silicon oxide etching with C4F8, which was included in our process, might have polymer deposition during etching.[123] However, it must not be the polymerization process alone leading to the passivation. PMMA must play an important role in this phenomenon because the same etching process did not result in passivation of DUV photoresist (UV210-0.6) as described in the following session. Thus, further investigation is needed to identify the material composition and reasoning of this passivation phenomenon. Thus, we concluded that E-beam lithography (Fig 3.2a) might not be the best fabrication process for our purpose. It required a lot more work in parameter tuning in the etching process, which was not the goal of our project. In addition, E-beam lithography had very low throughput, compared to the process of the second method (Fig 3.2b).

3.3.2 Oxide deposition can successfully reduce nanochannels

After the E-Beam lithography method failed, we tried to fabricate ~250 nm wide and ~300 nm deep nanochannels with DUV and RIE on silica substrates, and then used oxide deposition to shrink the nanochannel width from 250 nm down to ~30 nm (Fig 3.2b). We chose to start from 250 nm because this was the resolution limit of our exposure tool, ASML 5500/300. As shown in Fig 3.5a,b, the nanochannel was approximately 280 nm after etching. This nanochannel could be shrunk down to ~25 nm (Fig 3.5c-e). Note, the silica surface from this fabrication process was free of residues. DUV photoresist (UV210-0.6) was passivated during the etching process since common organic solvent could not strip away the residual photoresist. However, all photoresists (including the anti-reflective coating) could be removed completely using oxygen plasma asher (Matrix Plasma Asher Model 106) followed by piranha cleaning at 120 ^{o}C for 10 min.

3.3.3 Single nanochannel can induce ICP based protein enrichment

After fabricating the first single-nanochannel preconcentrator, we tested it with Alexa-Fluor 647 conjugated streptavidin (Strep-647, Thermal Fisher Scientific, Waltham, MA). The solution loaded in this very first preconcentration experiment was composed by 20ug/ml strep-647, 0.075%BSA, and 0.1% Tween-20 in 1X PBS. We applied 25V DC voltage across the nano/microchannels through the reservoirs with the anode on the left and the cathode on the right. As shown in Fig 3.6, strep-647 was successfully enriched in front of the single nanochannel, and there was a depletion zone adjacent to that nanochannel. The image in Fig 3.6 was taken after one min of enrichment, and the signal in the enrichment zone was saturated, which represented >1 mg/ml of strep-647. Thus, we achieved more than 50 fold enrichment in one min.

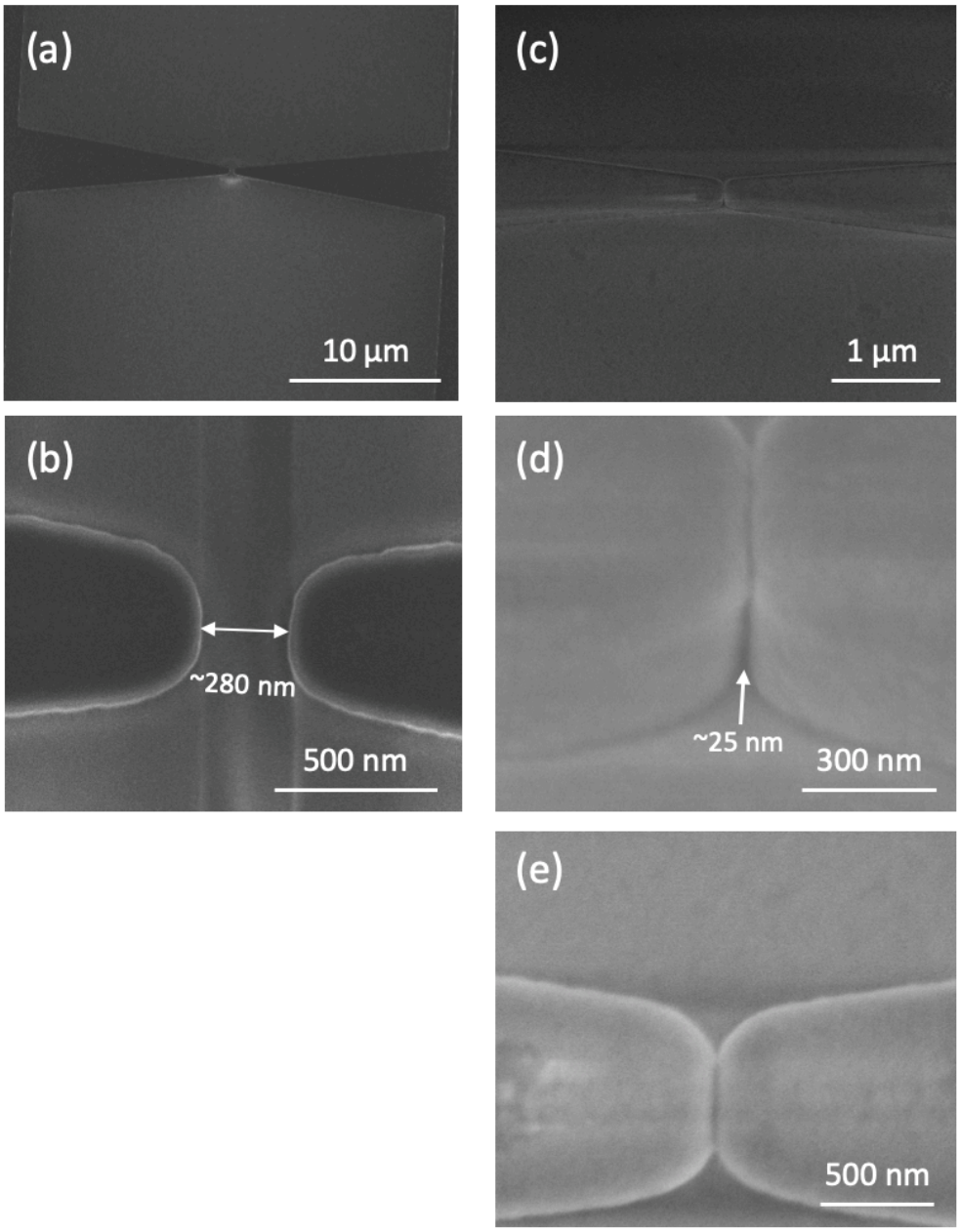

Fig 3.5 SEM images before and after oxide deposition.

SEM images before (a)&(b) and after (c)-(e) oxide deposition, approximately the area highlighted by red box in Fig 3.1b. In (a),(b),and (e) Images were taken at 90º, while in (c) and (d) the sample was tilted for 40º. The nanogap size was reduced from approximately 280 nm down to 25 nm. Note that these sizes are slightly off compared to the design in Fig 3.1. This is probably due to the fabrication and measurement error.

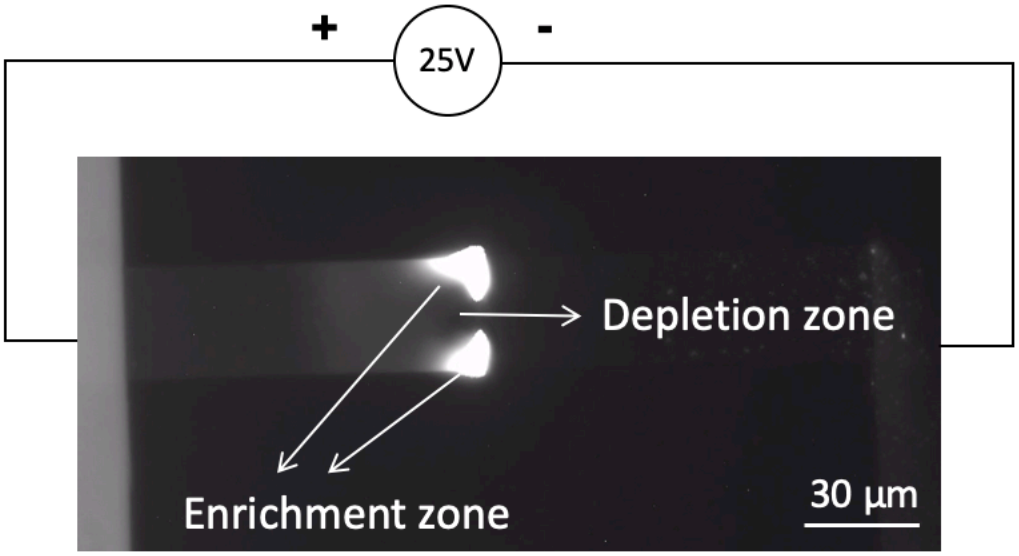

Fig 3.6 ICP based preconcentration in front of a single nanochannel.
Sample solution was composed by 20ug/ml strep-647, 0.075%BSA, and 0.1% Tween-20 in 1X PBS. A DC Voltage (25V) was applied across the nanochannel with anode on the left and cathode on the right.

3.3.4 Silane-PEG-Biotin is a better crosslinker for surface functionalization than APTES

Since our final goal was to perform immunoassays in this preconcentrator, we tried to functionalize the silica surface with biotin to mimic the antibody-antigen binding in immunoassays. We tried two different strategies for biotin conjugation in channels: 1) using APTES along with NHS-biotin and 2) using silane-PEG-biotin. Both of these two surface conjugation methods could successfully conjugate biotin onto the silica surface, but both of them changed the hydrophobicity of the surface as shown in Fig 3.7. The first strategy (APTES+NHS-biotin) resulted in more hydrophobic surfaces, compared to the bare silica surfaces. The contact angle after the treatment of APTES and NHS-biotin (contact angle = 68.8^{o}) was approximately twice as large as the contact angle of bare silica (contact angle =35.2^{o}). However, the second strategy (using silane-PEG-biotin) reduced the contact angle by approximately 35%, making the surfaces more hydrophilic, which due to the hydrophilic PEG spacer. Since our microchannels were only ~300 nm deep, a hydrophobic surface would prevent solution loading into the channel. Thus, we decided to use silane-PEG-biotin for streptavidin detection in our preconcentration device.

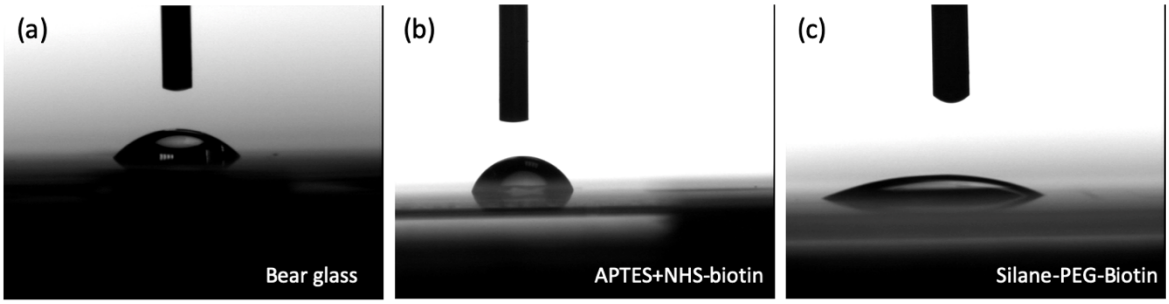

Fig 3.7 Contact angle of glass surface with different surface chemistry.
The use of APTS resulted in a more hydrophobic surface than bare glass, while the PEG crosslinker led to a more hydrophilic surface. A hydrophilic surface is better for sample loading into the microchannels and nanogaps.

3.3.5 Multi-nanochannel design leads to faster analytes accumulation due to higher electroosmotic flow

After conjugating biotin in front of the nanochannels (grey areas in Fig 3.8a1), the preconcentrators were sealed and tested with strep-647. We tested the detection of strep-647 in single-nanochannel preconcentrator by loading sample solution (20 ng/ml strep-647, 0.75% BSA and 0.1% Tween in 1X PBS) and applied 25V DC voltage for 15 min. As shown in Fig 3.8a3, the detection zone has a higher fluorescent intensity than the background, meaning 20 ng/ml strep-647 could be detected successfully.

However, given the high affinity of streptavidin-biotin pairs, this result was not good enough, since our target was to get sub-picomolar sensitivity in tens of minutes. We could detect 20 ng/ml strep-647 in 15min by simply adding sample solution on top of the biotinylated surface without preconcentration. Since all molecules accumulated in the enrichment zones are carried by electroosmotic flows from the bulk areas to the enrichment areas, the low volumetric flow in single-nanochannel devices may be the reason for low sensitivity. If we assume no molecule leaking into the downstream, the enrichment speed should be proportional to the electroosmotic flow, although this is not completely true[62]. This is partially proved by the fact that higher DC voltage induces faster enrichment in Chapter 4 since the electroosmotic flow rate is proportional to the electric field. Again, this is not completely true, since the voltage also affects the ICP development[62], but at least in the range of the voltages we tested, it shows this linear relationship approximately (details in Chapter 4).

As shown in Fig 3.8a2, the single nanochannel design induced two small enrichment zones. Although the intensity in these two small enrichment zones was 50 times higher than the background after 1 min enrichment, the total number of molecules enriched was still very limited.

Note, the sample solution in Fig 3.8a2 had 20 µg/ml strep-647 for a better demonstration of the shape of the enrichment zone. The intensity from 20 ng/ml enrichment was much lower.

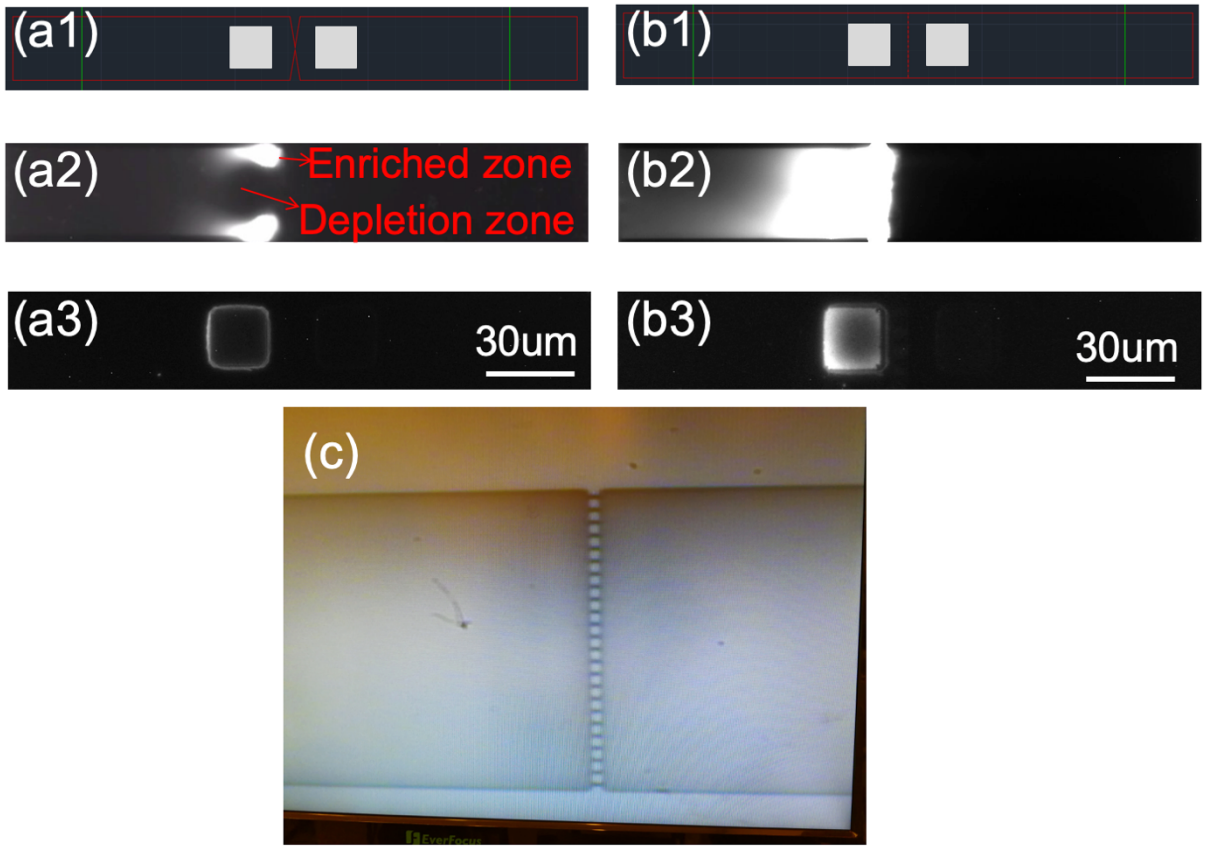

Fig 3.8 Single vs multiple nanochannels enrichment.
(a1) & (b1), single-/multiple-nanochannel designs and biotin conjugation areas. The red lines are the outline of the nanostructure and the grey squares are the biotin conjugation areas (detection zone). Both single-nanochannel (a2) and 24-nanochannel (b2) design were used to enrich 20 µg/ml Strep-647 with 0.75% BSA and 0.1% Tween in 1X PBS at 25V. Both images (a2 & b2) were taken after 1 min enrichment. Multi-nanochannel design led to much larger enrichment zone, indicating more strep-647 accumulated in the detection zone. (a3) & (b3) 20 ng/ml strep-647 was detected with the single-nanochannel (a3)and the multi-nanochannel design (b3). Multiple nanochannels accumulated more strep-647 molecules and resulted in higher intensity in detection zone. (c) The top view of the multi-nanochannel design.

Then, we tried to increase the volumetric flow by increasing the number of nanochannels. Increasing the number of nanochannels per microchannel does not increase the flow rate in each nanochannel since the linear velocity of electroosmotic flow should only be affected by the electric field and zeta potential of the surface. However, the total volumetric flow in each microchannel is proportional to the number of nanochannels per microchannel, assuming that the flow rate in each nanochannel remains the same.

As shown in Fig 3.8b1, we designed 24 nanochannels in each microchannel. In this design, all the fabrication process and the depth of nano/microchannels were the same as for the single-nanochannel design, so that we didn't need to change any fabrication parameters for the new design. We used the multi-nanochannel design to enrich 20 μg/ml strep-647 in 1X PBS with 0.75% BSA and 0.1% Tween at 25V (Fig 3.8b2). The 23 micropillars formed 24 nanochannels in the middle of each microchannel(Fig 3.8c). These micropillars (1μm by 1μm) have the same height as the microchannel sidewalls (~300 nm). Compared to the enrichment with single nanochannel design (Fig 3.8a2), multichannel design induced much larger enrichment zone with more molecules accumulated. We also repeated the experiment in Fig 3.8a3. Multi-nanochannel design resulted in much higher intensity for 20 ng/ml strep-647 under the same enrichment setting (Fig 3.8b3). This result demonstrated the fact that higher volumetric flow resulted in faster accumulation of protein molecules.

3.3.7 Multi-nanochannel design can detect 2 ng/ml strep-647 in 10 min

After confirming that multi-nanochannel design resulted in faster protein enrichment, we used this design to detect strep-647 at various concentrations (Fig 3.9). Strep-647 was diluted in 1X PBS with 0.75% BSA and 0.1% Tween-20. Both BSA and Tween-20 were used to reduce the unspecific binding on channel walls. We applied 25V through reservoirs with the anode on the left and the cathode on the right. As shown in Fig 3.9, 2 ng/ml strep-647 could be detected after 10 min enrichment and the signal saturated after 5 min enrichment of 200 ng/ml strep-647. The intensity was quantified along the orange lines in Fig 3.9. Fig 3.10a shows the intensity of 2 ng/ml strep-647 detection after 10 min and 20 min enrichment at 25V. Fig 3.10b shows the intensity of strep-647 detection at various concentrations with 10 min enrichment at 25V. These results demonstrate that 1) immunoassays can be integrated into preconcentrators; 2) multi-nanochannel design and higher electroosmotic flow accelerate enrichment.

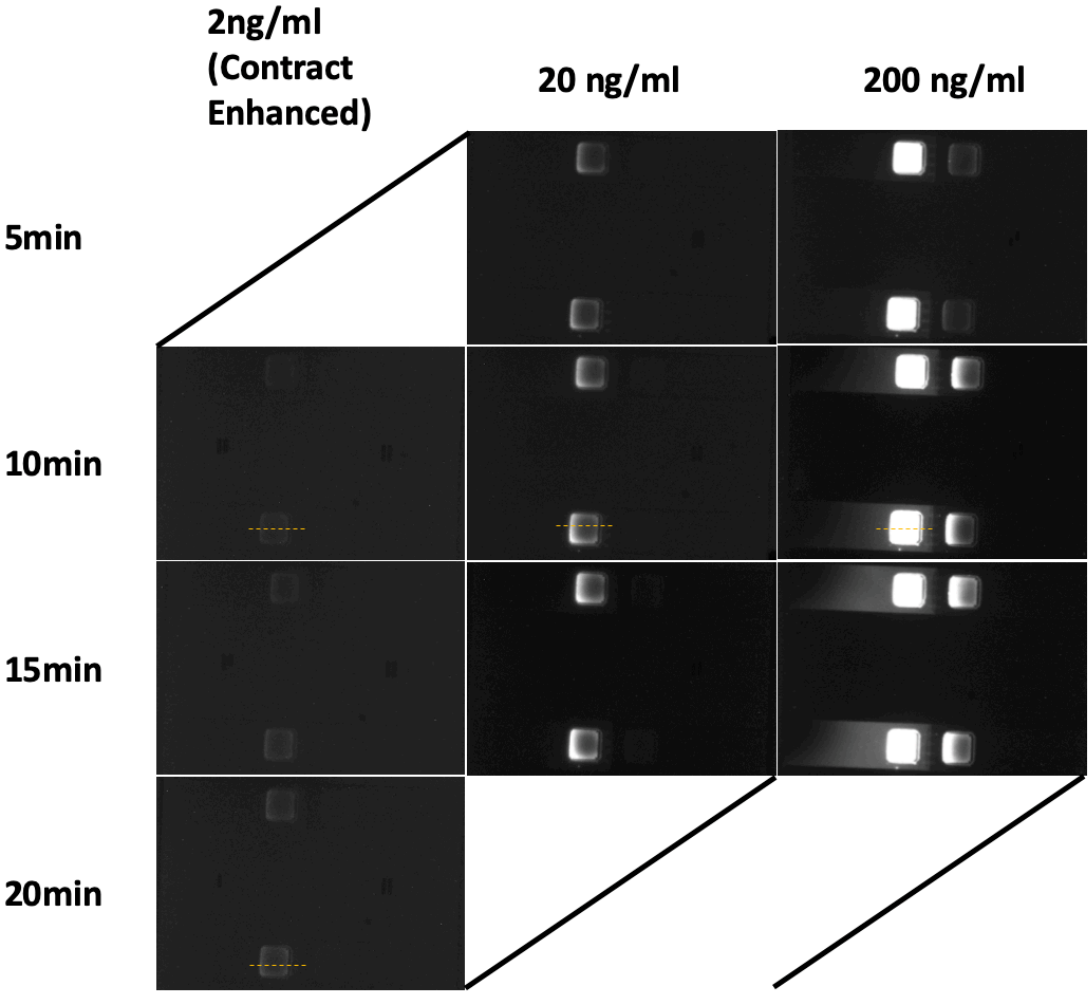

Fig 3.9 The detection of streptavidin at various concentrations and enrichment times.

All the experiments were performed in 1x PBS with 0.75% BSA and 0.1% Tween and Strep-647 was enriched under 25V DC voltage. Images for 38pM were enhanced for 40% of brightness for a better demonstration.

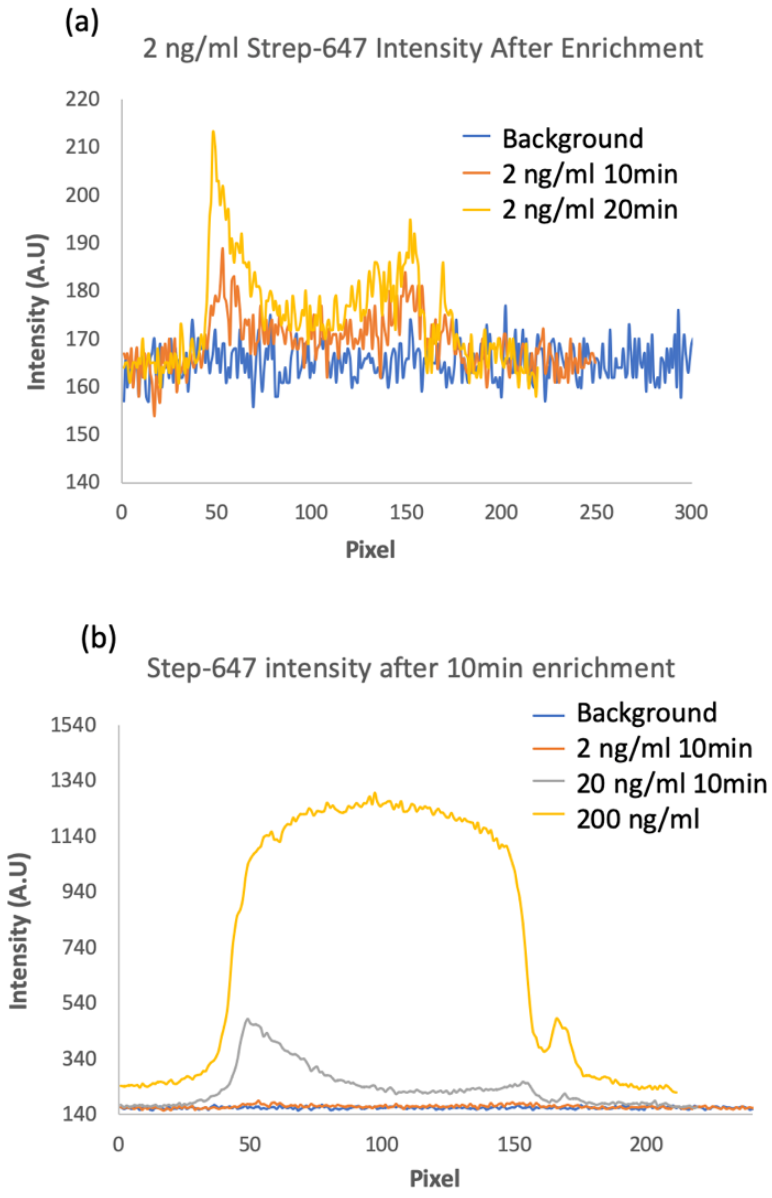

Fig 3.10 Detection of fluorescent streptavidin with multichannel enrichment.
(a) 2 ng/ml Strep-647 detection with 10min & 20min enrichment under 25V. (b) Strep-647 detection at various concentrations with 10min enrichment under 25V. These measurements were made along the orange lines in images in Fig 3.9.

3.3.7 Blow dry process deactivates antibodies on the substrates

In order to perform protein detection other than streptavidin, we needed to immobilize antibodies (instead of biotin) onto the surface before sealing. The sealing process required the two surfaces to be dry and clean. However, the drying process deactivated the antibody (Fig 3.11).

We used 3 types of secondary antibodies (2nd Ab) to verify the immobilization of the first antibody on the substrates. The 2nd Ab 1 (clone G28-5, BD Bioscience, San Jose, CA) and 2nd Ab 2 (clone RG11/39.4, BD Bioscience, San Jose, CA) were both FITC conjugated monoclonal secondary antibodies. The 2nd Ab1 and Ab2 specifically target to IgG1/2a and the Fc region of IgG1. Both of these two secondary antibodies showed fluorescent signals in the wet group (Fig 3.11a,c) but no signals in the dry group (Fig 3.11b,d). This indicated that our antibody immobilization process was successful, but the blow-dry process deactivated the capture antibody.

The 2nd Ab 3 (Goat anti-Rat IgG Cross-Adsorbed Secondary Antibody, Thermal Fisher Scientific, Waltham, MA) was an Alexa Fluor 546 conjugated polyclonal secondary antibody, which was less specific than the 2nd Ab 1 and 2nd Ab 2. This secondary antibody showed signal in both groups (Fig 3.11g,h), indicating that the primary-antibody molecules were still on the substrate after blowing dry. The blow-dry process might partially change the folding or the structure of the immobilized IgG. Thus, the polyclonal 2nd Ab 3 (binding to both heavy and light chains) could still bind to those dried IgG, while the secondary antibodies (2nd Ab 1 and 2nd Ab 2) with higher specificity could not.

We also tested the activity of the immobilized antibody by adding its antigen (2 μg/ml IL6) followed by loading of the detection antibody (Biotin Rat Anti-mouse IL6, BD Bioscience, San Jose, CA) and Strep-647. If the immobilized capture antibody still maintained its affinity to its antigen (IL6) despite the effect of drying, detection antibody could still bind to the captured IL6 molecules and in turn fluorescently labeled by strep-647. However, only the wet group showed fluorescent signals in this sandwich assay, and the dry group showed no signals at all (Fig 3.11e,f). Thus, our results showed that we had successfully conjugated primary antibody onto the silica substrates, but the drying step required by the following sealing process deactivated our immobilized antibody. Note that we didn't even dissolve the Ge layer after immobilization. The diluted H_2O_2 was also expected to deactivate the IgG by oxidation.

In addition, due to the surface bioconjugation, only the PSQ wafer could be plasma treated. This asymmetric plasma treatment lowered the bonding strength and increased the ratio of leaking devices. Thus, we concluded that surface functionalization might not be a good choice for our preconcentration device unless the activity of antibodies could be maintained during the drying process or another bonding process could be applied without drying the surface. Therefore, we used antibody conjugated microbeads in our next-generation devices (Chapter 4).

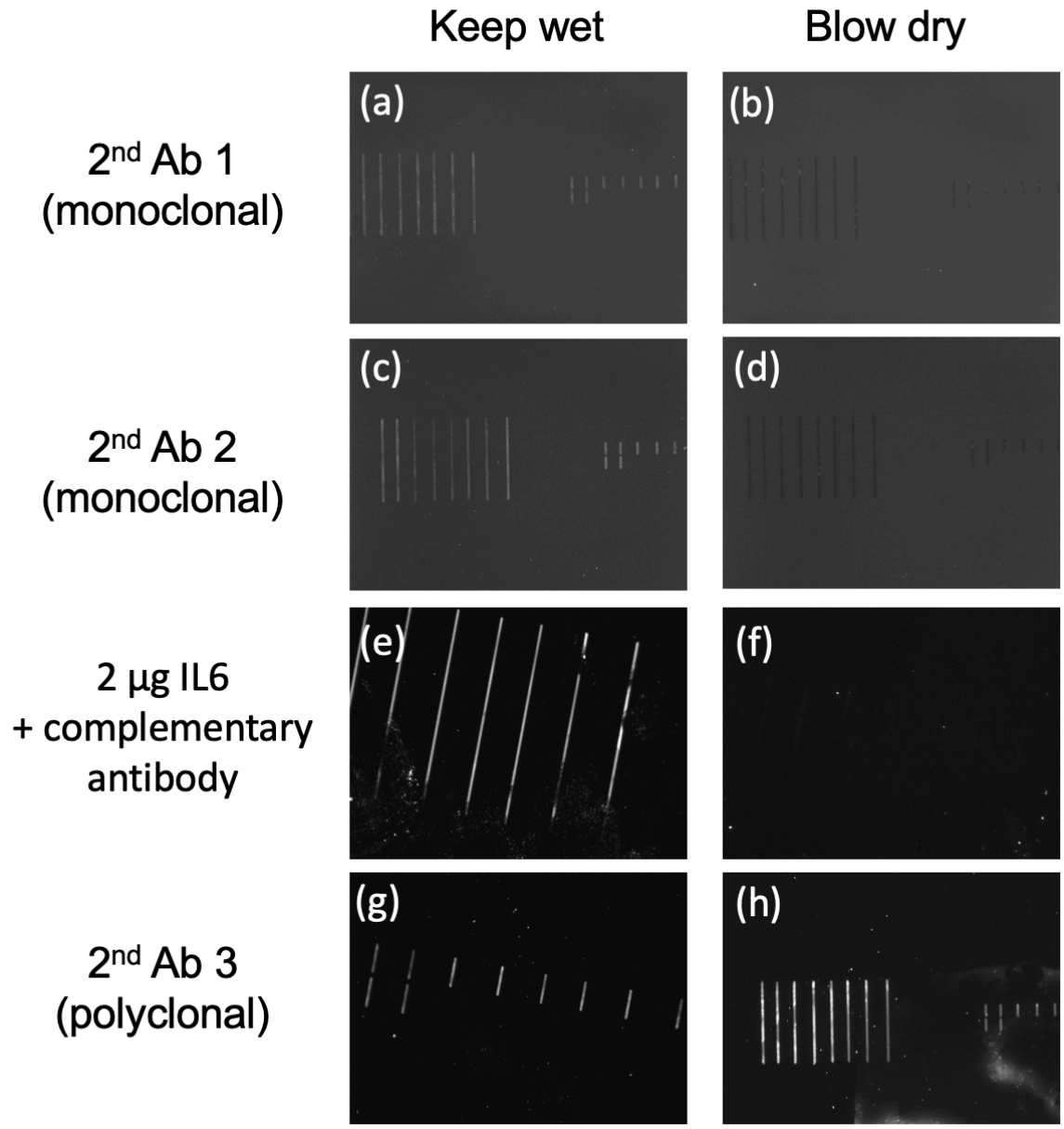

Fig 3.11 Drying process deactivated antibody for analyte capturing.
The 2nd Ab 1&2 are the antibodies specifically targeting to the light chains of IgG molecules, which are the binding sites of antibodies. No fluorescent signals from 2nd Ab1&2 after blowing dry the surface (b)&(d) suggested the deactivation of capture antibodies on the surface. The absence of signals in (f) confirmed this result. The 2nd Ab 3 targets to both heavy chains and light chains of antibodies, and the signal in (g) &(h) demonstrated the successful conjugation of capture antibodies on the surfaces. The blow-dry process only deactivated the antibody and the main IgG molecules were still on the surface.

3.3.8 Antibody conjugation on microbeads

After conjugating anti-IL6 antibody onto the microbeads by EDC/NHS chemistry, we verified the conjugation by using 2nd Ab1 and Ab3 (same as *section 3.3.7*), as shown in Fig 3.12 and Fig 3.13. With both 2nd Ab1 and Ab3, we got strong fluorescent signals in all groups, including the group with no primary antibody conjugated (negative control group). The signal in the group of negative control showed strong unspecific binding of 2nd antibody on the surfaces of microbeads. To reduce unspecific binding, we blocked the microbeads with 1% BSA before incubating them with 2nd Ab3 (Fig 3.14). In Fig 3.14, the no-conjugation group had no fluorescent signal while another two groups had strong fluorescent signal, which proved that we had successfully conjugated the primary antibody onto the microbeads and these signals were not due to the unspecific binding of the 2nd antibody.

After showing the existence of primary antibody on the microbeads, we also demonstrated the possibility of employing sandwich immunoassays on these microbeads (Fig 3.15). We incubated these antibody-conjugated microbeads with 2μg/ml mouse IL6 for 1h, followed by the incubation with complimentary antibody (detection antibody; *same as section 3.3.7*) for 30 min. Since these detection antibody molecules were biotinylated, we incubated these microbeads with strep-647 to provide fluorescent signals. As shown in Fig 3.15, the 1x EDC/NHS group showed much higher intensity than the group of 0.02x EDC/NHS, indicating that the lower EDC/NHS concentration had lower conjugation efficiency and resulted in less primary antibody molecules on each microbead. The absence of fluorescent signal in the group of negative control proved that unspecific bindings did not cause all those signals in another two groups in Fig 3.15. Thus, these microbeads were ready for immunoassays in our preconcentration devices.

3.3.9 Deep nanochannels can be fabricated on silicon substrates followed by oxide deposition

Besides the problem of surface antibody stability, we also tried to enhance the analyte accumulation in our device even further. In section 3.3.6, we demonstrated the detection of 2 ng/ml strep-647, which is still not good enough, especially for those low abundance proteins like cytokines, whose concentrations are usually in the range of pg/ml.[124–127] As we discussed above, the rate of analyte accumulation should increase along with the volumetric electroosmotic flow. Thus, we further increased the volumetric flow rate in each microchannel by increasing the depth of the nano/microchannel from ~300nm to several microns. This depth was again limited by the aspect ratio of the etching process.

To increase the depth of the nanochannels, we had to switch from silica wafers to silicon wafers for two reasons. 1) RIE tool for oxide etching in our lab cannot provide such high aspect ratio (height vs. width > 20:1). In our previous fabrication, the 250 nm wide and 300 nm deep nanochannels only required approximately 1:1 aspect ratio, but if we increased the depth to 10 μm, the aspect ratio would be 40:1. 2) The oxide etching recipe does not have high enough selectivity to DUV photoresist. Our inductively coupled plasma etcher uses C_4F_8 for silicon dioxide etching, and the selectivity to photoresist is approximately 4:1, meaning that the photoresist has to be >1μm

for a 4 μm deep etching. However, increasing the thickness of DUV photoresist from 420 nm to >1 μm compromises nanoscale resolution.

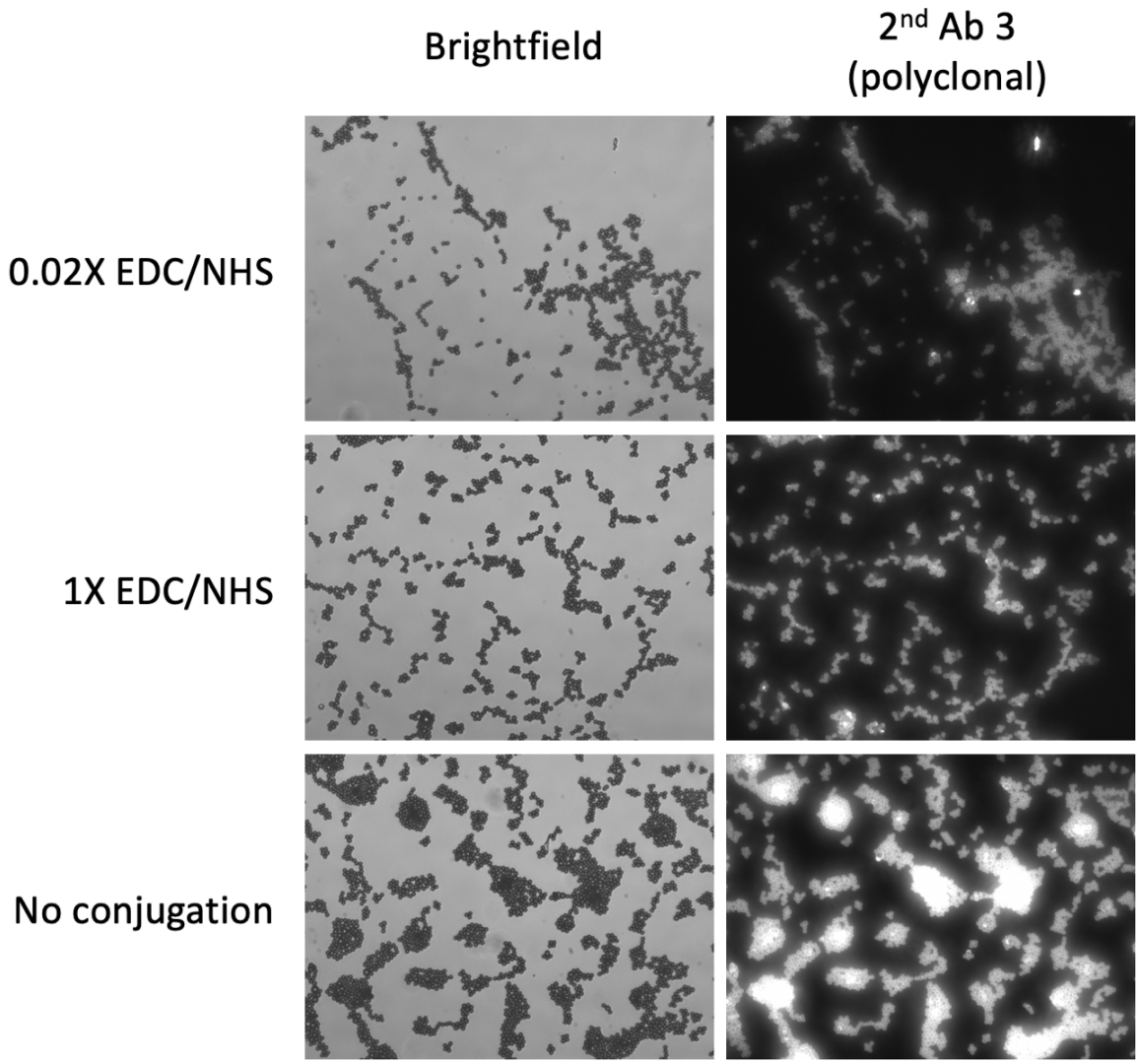

Fig 3.12 Labeling primary antibody on microbeads with polyclonal 2nd antibody. *These microbeads were conjugated with primary antibody with EDC/NHS chemistry and then labeled by 2nd Ab 3. This is a polyclonal secondary antibody targeting to both heavy and light chains of rat IgG molecules. The fluorescent signal in third group (no-conjugation group) showed strong unspecific binding on beads.*

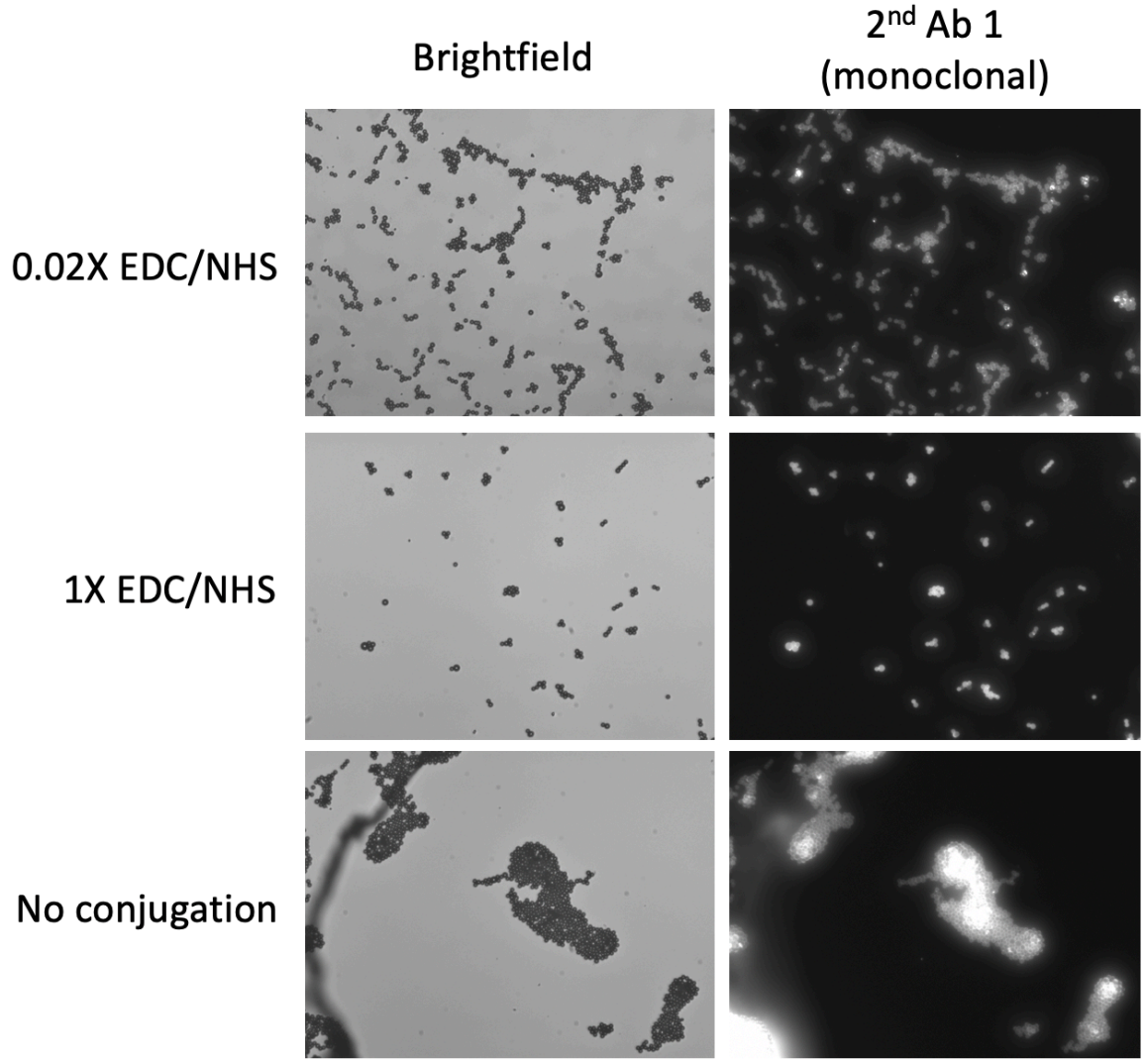

Fig 3.13 Labeling primary antibody on microbeads with monoclonal 2nd antibody.

These microbeads were conjugated with primary antibody with EDC/NHS chemistry and then labeled by 2nd Ab 1. This is a monoclonal secondary antibody targeting to IgG1/2a specifically. The fluorescent signal in third group (no-conjugation group) showed strong unspecific binding on beads.

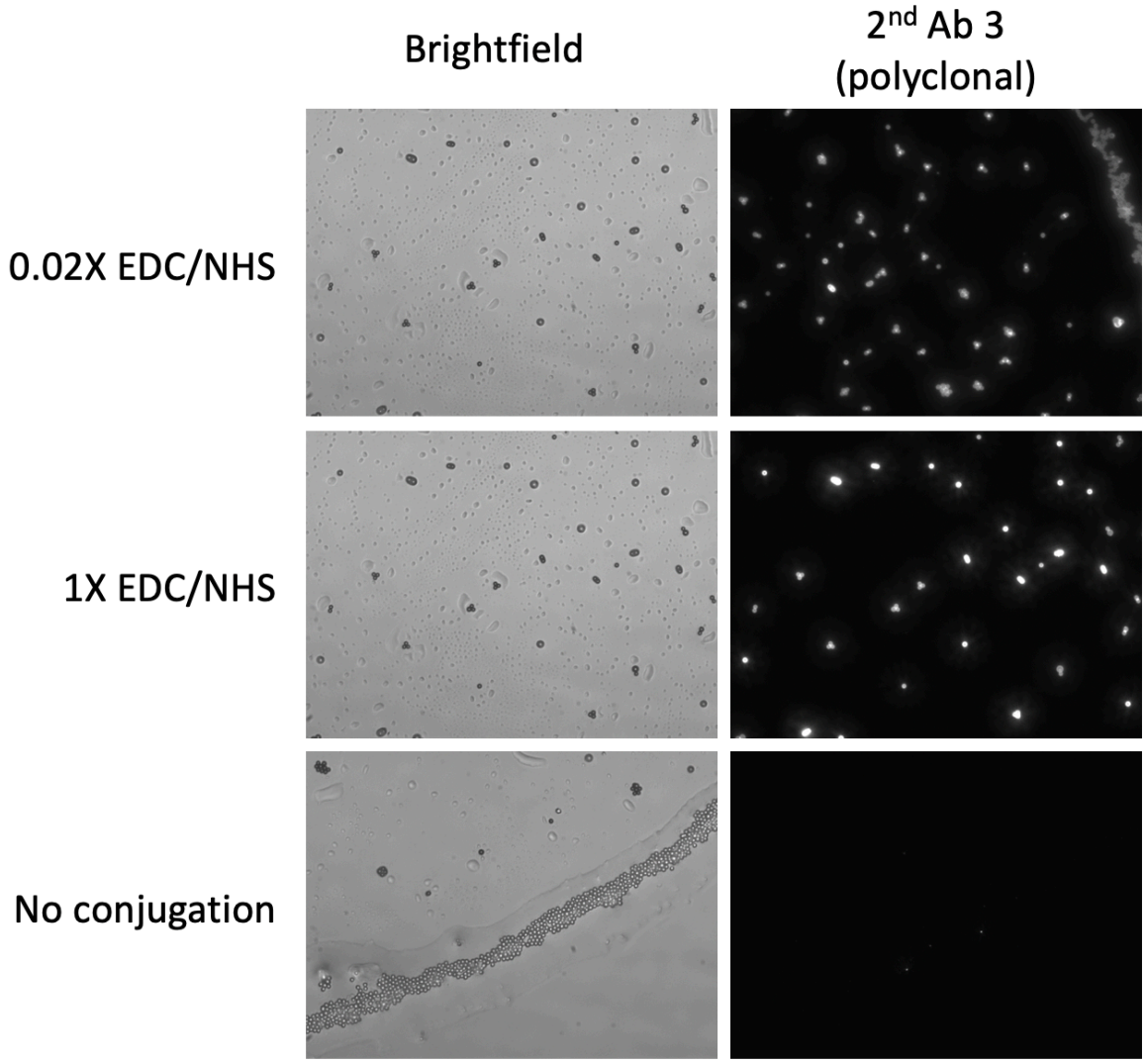

Fig 3.14 Blocking with BSA prevented the unspecific binding on microbeads.
These microbeads were conjugated with primary antibody with EDC/NHS chemistry and then incubated with by 2nd Ab 3. The absence of fluorescent signal in the third group (no-conjugation group) proved that BSA could significantly reduce unspecific binding, and the signals in the first and second groups were caused by the specific binding of 2nd Ab 3 on the primary antibody.

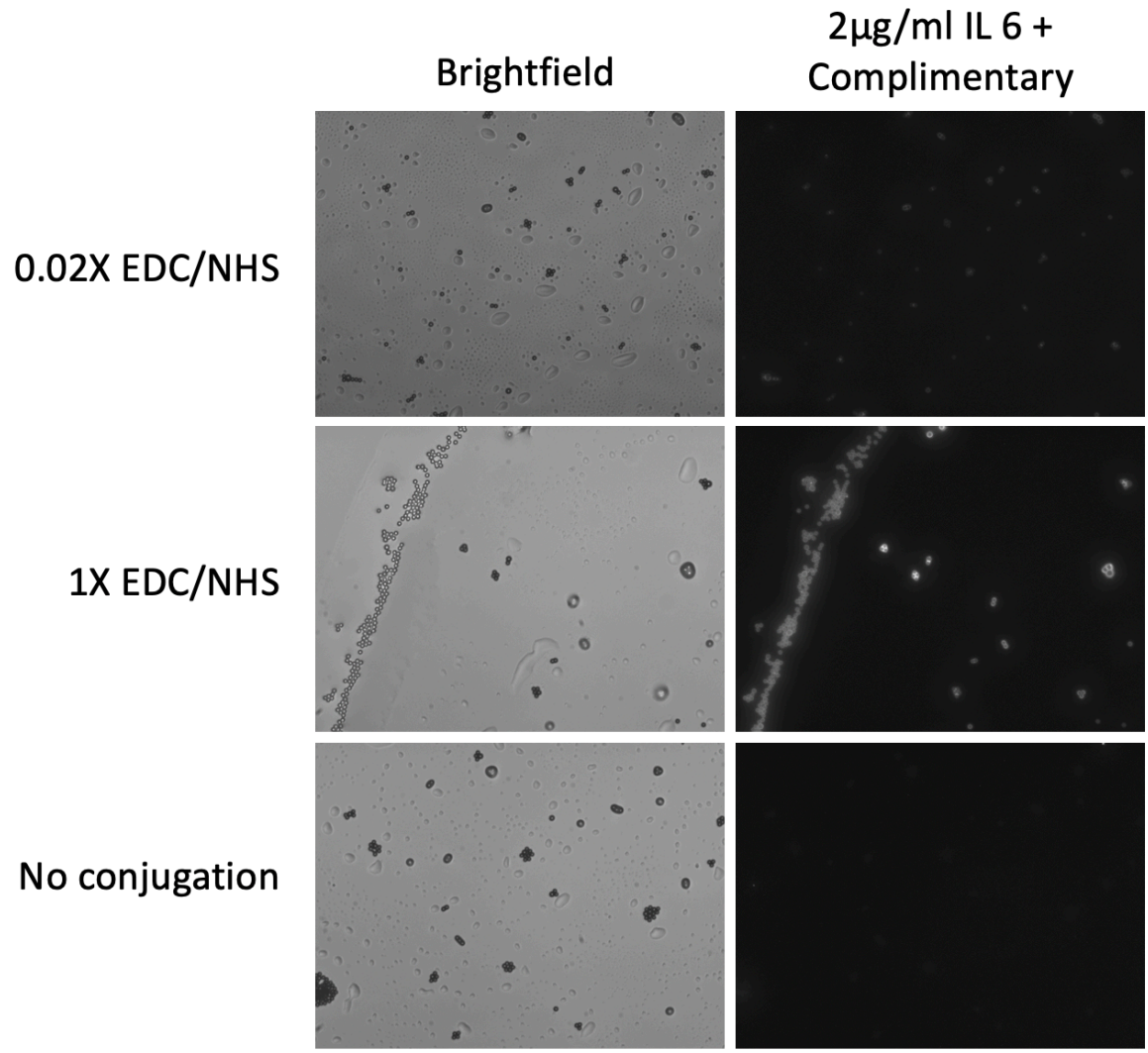

Fig 3.15 Sandwich assay on microbeads.
These microbeads were conjugated with anti-IL6 primary antibody with EDC/NHS chemistry and then incubated with 2µg/ml IL6. After washing away excessive IL6 molecules, the microbeads were incubated with detection antibody and strep-647 to label the captured IL6 molecules on microbeads.

Since we switched substrates, it was necessary for us to find the proper tool and recipe to etch silicon with high aspect ratio. We used a pattern similar to the one in Fig 3.8b2, except that there were only 12 nanochannels per microchannel (instead of 24 nanochannels in Fig 3.8b2). The pillars were designed to be 600 nm x 400 nm, and the gaps between pillars were 250nm. We first etched the silicon substrates with a transformer-coupled plasma etching system (LAM TCP 9400SE) using Cl_2(50 sccm) and HBr (150 sccm). As shown in Fig 3.16, after a ~4 µm etch, six

out of eleven pillars fell. The pillars were highly tapered since the etching profile was not perfectly 90°. The pillars fell during the etching process because the highly tapered bottoms could not support the larger upperparts. This effect was not noticeable, until decreasing the feature size down to sub-micron scale. Thus, this etching process does not fulfill our requirements for high-aspect-ratio nanochannels.

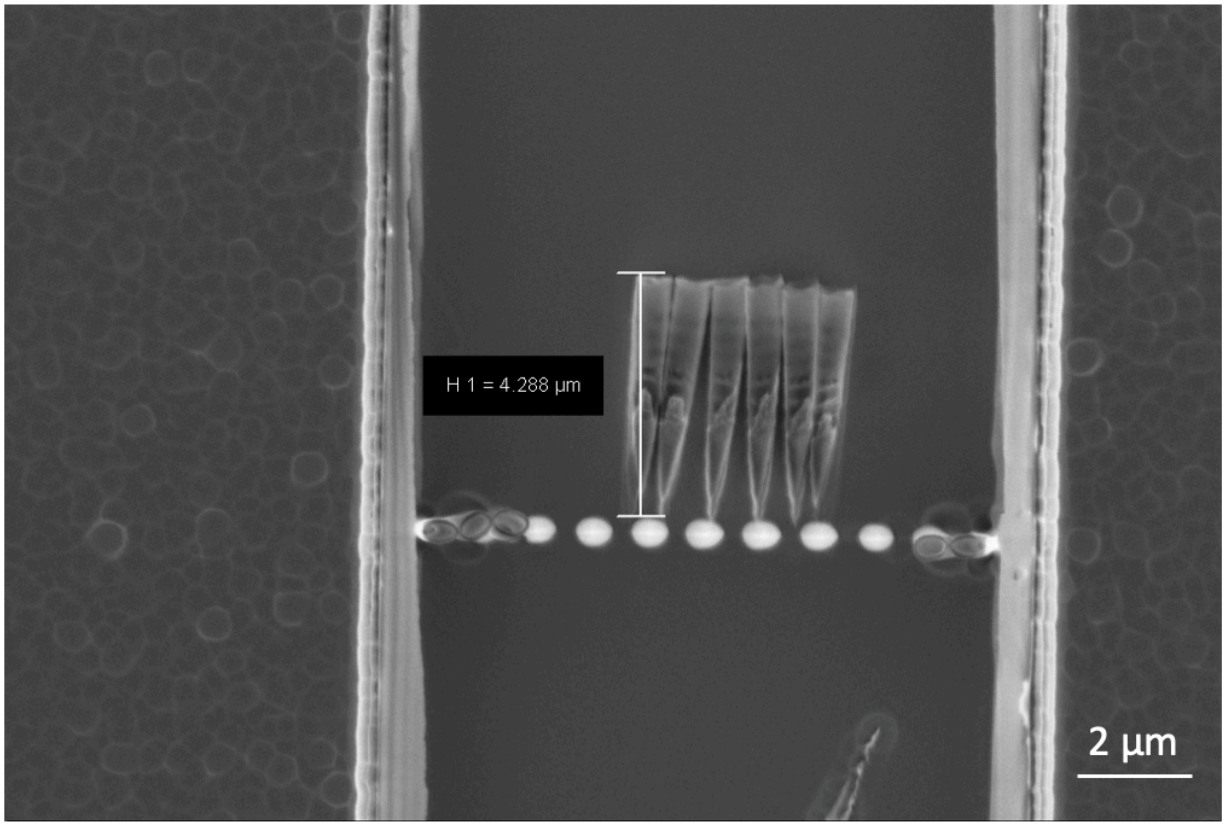

Fig 3.16 Silicon etching with Cl_2 in TCP 9400 does not have high enough aspect ratio.

These pillars were designed to be 600 nm x 400 nm in lateral. The pillars were approximately 4 µm tall, same as the depth of the trench in this image. The gap between pillars were designed to be 250 nm. This is a top view SEM. We can see the sidewalls of pillars in this SEM because some of the pillars (6 out of 11) fell. This etching recipe resulted in tapered pillars (negatively tapered trench between pillars).

Then, we started trying to use DRIE (or Bosch process) in an inductively coupled plasma etcher (SPTS Technologies, Newport, UK). The DRIE process alternates etching and deposition steps using SF_6 and C_4F_8 plasma, respectively.[128–132] The first step is usually to deposit a passivation layer to protect the sidewalls, and the second step is to etch away the polymer and the silicon. Since the etch rate on the bottom of the trench is greater than the rate on the sidewalls, the passivation polymer can effectively protect the sidewalls, while the silicon on the bottom is etched. This alternating mechanism results in highly anisotropic profile, although the SF_6 plasma etching is isotropic.

However, the isotropic etching causes rippled sidewalls as shown in Fig 3.17a,b (adapted from Jae-Ho Min, 2005)[132]. The duration of etch and deposition determines the size of the ripples. Generally, the longer duration causes larger undercuts (Fig 3.17a,b). The ratio of etch to deposition durations determines the angles between the sidewalls and the bottom of the channels. A larger ratio leads to negatively tapered sidewalls (Fig 3.17c), while a small ratio causes tapered channels (Fig 3.17d).[132] These are the two major factors limiting the feature size under submicron scales, so we tuned these two factors to optimize the DRIE recipe for our purpose.

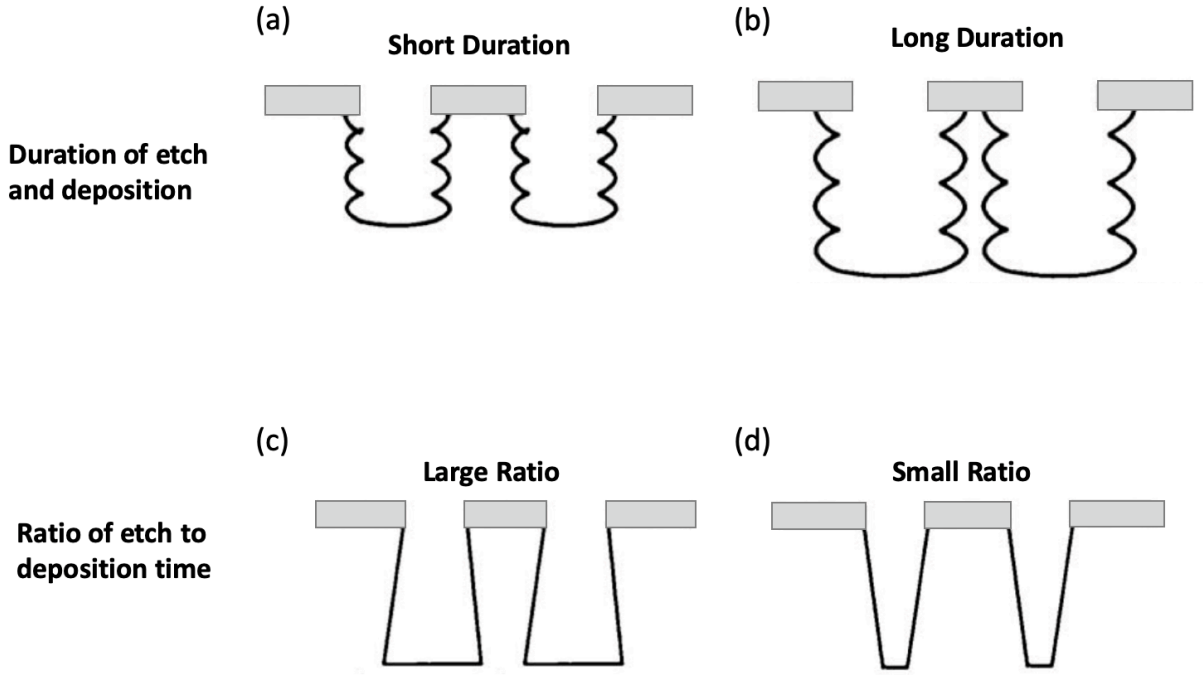

Fig 3.17 The duration and ratio of etch and deposition determines the shape of sidewalls.
(a)&(b) The longer etching duration for each cycle results in the larger size of sidewall ripples (larger undercut). (c) A large etch to deposition ratio leads to negatively tapered channel, while a smaller etch to deposition ratio (d) leads to tapered channels.

As shown in Fig 3.18, all pillars were completely etched away when we applied 5 s deposition and 7 s etching. The feature design was exactly the same as Fig 3.16 and the complete recipe is shown in Table 3.1. All pillars disappeared because the undercuts (ripples) were too large and the etched away most of the materials underneath the photoresists. Thus, we decreased the duration of etch and deposition to adjust the sizes of the ripples (Fig 3.19). Note, in this experiment, we used a layer of ~400 nm thick oxide as our hard mask. The etching process had higher selectivity to oxide (>100: 1) compared to the selectivity to photoresist (~50:1), since we were targeting to >20 μm depth at the very beginning, and a layer of ~420 nm photoresist was not enough for that purpose. The size of the ripples reduced from ~100 nm to ~30 nm, when we decreased the durations from 4 s deposition and 5 s etch to 2 s deposition and 3 s etch.

We finalized our process with 2 s deposition and 3 s etch because our tool could not switch gases fast enough to decrease the cycle times further. The sidewall profile was still negatively tapered, and the etching limit was around 6 μm deep (Fig 3.20a). Deeper etching (>6 μm) resulted in pillar falling. With this etching depth, we did not need an oxide hard mask, so we didn't use this hard mask anymore in our fabrication process.

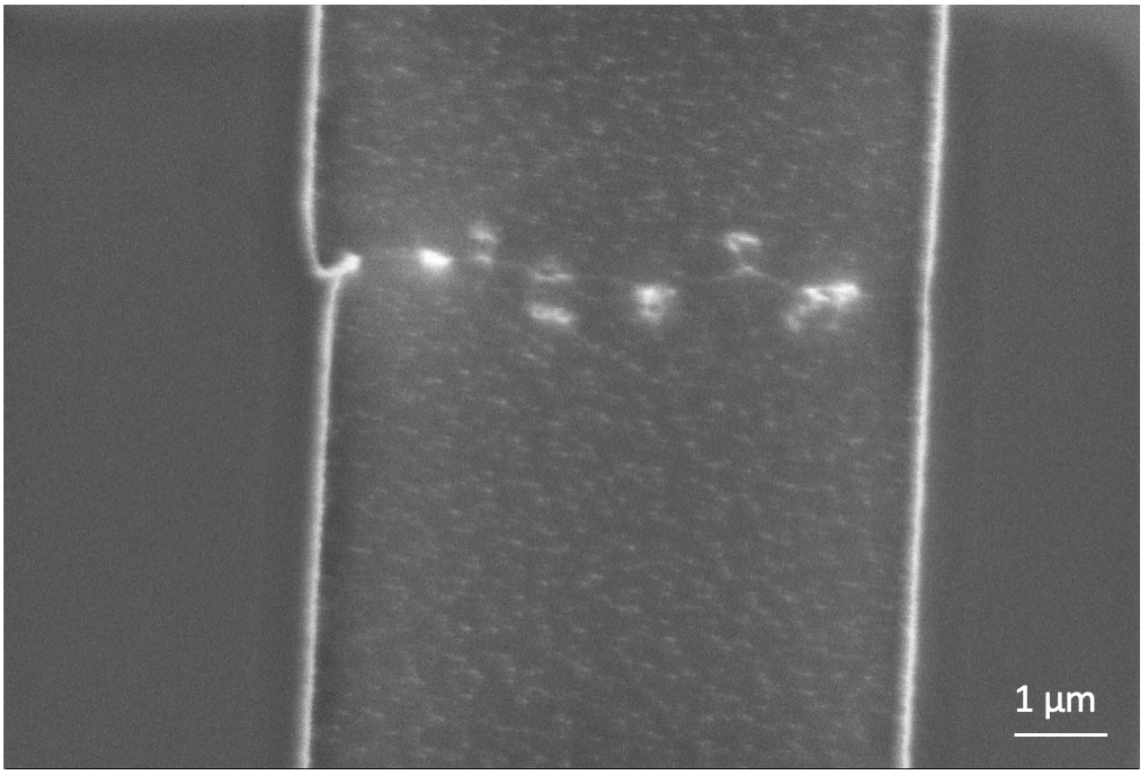

Fig 3.18. Top view of micropillars after DRIE for 3 microns.
Standard recipe (Passivation 5 sec / Etching 7 sec) was used in this experiment. All pillars were etched away and ended up without nanochannels.

After finalizing the etching recipe, we needed to find the proper oxide deposition recipe to shrink the size of gaps between pillars. Since our structure had a high aspect ratio and small gaps between pillars, we started with thermal oxidation because it is highly conformal. Thermal oxidation with O_2 only (dry oxidation) for 6 hrs was not enough to fill up the gaps (Fig 3.20b), so we added DI water steam into the furnace to accelerate the oxidation process (wet oxidation, Fig 3.20c,d).[133,134] After a 6 hr wet oxidation, the sidewall of the trench (microchannel) swelled and deformed the adjacent pillar (Fig 3.20d). However, the nanochannel sizes between pillars were still hundreds of nanometers, one magnitude larger than our target size (30 nm). This result indicates that the sidewalls have a higher oxidation rate than the pillars, probably because the pillars do not contain enough silicon to oxidize, although more investigation is needed for a more accurate explanation. After dry and wet oxidation failed filling up the gaps, we used a low-pressure chemical vapor deposition (LPCVD) furnace (TYTAN Diffusion Furnace System, Tystar, Garden Grove, CA) to deposit a layer of high-temperature oxide (HTO) at 900 °C. As shown in Fig

13.20e,f, HTO successfully shrunk the nanochannel size down to tens of nanometers. Thus, we used HTO to reduce nanochannel for all the following experiments in the next chapter.

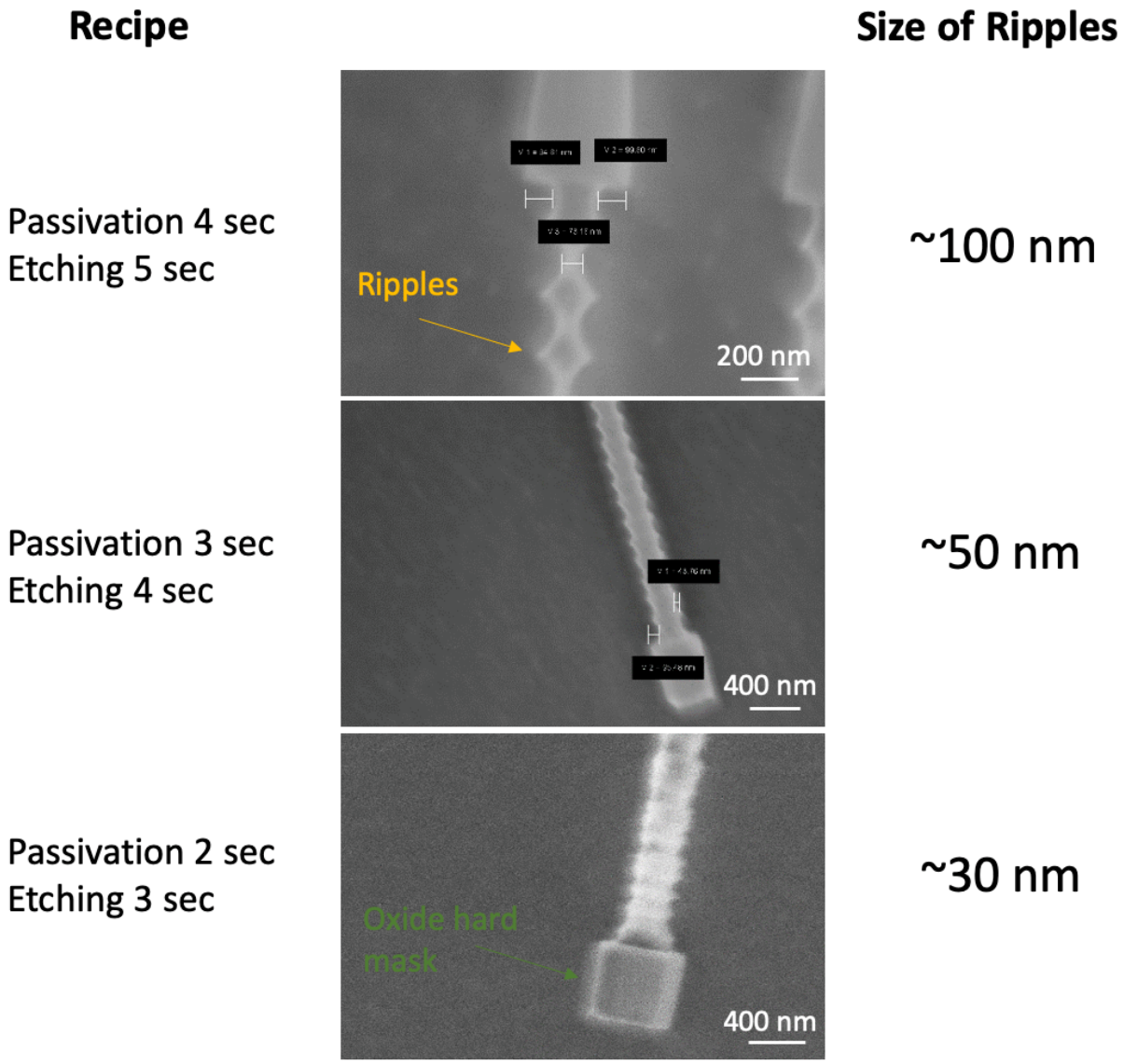

Fig 3.19 The shorter durations resulted in the smaller ripples.
Decreasing etching duration from 5 s to 3 sec reduces the sizes of ripples (orange arrow) from 100 nm to 30 nm. Oxide hard mask (green arrow) was used in this experiments, since we expected to etch tens of microns, which would exceed the limit of depth achievable from 420 nm thick photoresist. After we chose ~6.5 μm as the depth of our channels (height of pillars), oxide was not used anymore.

Table 3.1. DRIE recipe

Parameters	Passivation	Etch
Cycle Times (sec)	various (2-5s)	various (3s-7s)
C4F8 Flow (sccm)	100	0
SF6 Flow (sccm)	0	130
O2 Flow (sccm)	0	13
Coil Power (W)	600	600
Bias Power (W)	0	20
Bias Frequency (MHz)	0	13.56
Platen Chiller (C)	25	25

3.4 Conclusion

An ICP based preconcentration device was developed with 24 vertical nanochannels in each microchannel. The multi-nanochannel device led to a >10 times higher sensitivity (sensitivity increased from 20 ng/ml to 2 ng/ml) compared to the single-nanochannel device, due to the faster accumulation of protein molecules resulted from the higher volumetric flow rate. To further enhance the electroosmotic flow in the microchannel, we switched from silica substrates to silicon substrates for deeper nanochannels with a high aspect ratio. By increasing the depth from ~300nm to 6 μm, the volumetric flow rate should increase by 20-fold with the same linear flow rate. The fabrication process was demonstrated for these high-aspect-ratio nanochannels on a silicon wafer. The next step is to enhance the performance even further by using a new design with 398 vertical nanochannels (instead of tens of nanochannels) per microchannel (Chapter 4). The additional nanochannels should provide ~20 fold improvement in volumetric flow. Thus, this new design (398 nanochannels with the depth of 6 μm) can result in approximately 400-fold enhancement in sensitivity, compared to the multi-nanochannel design with the depth of ~300 nm. On the other hand, we switched from surface immunoassays to bead-based immunoassays, since antibodies were deactivated during the drying process, which was necessary for the sealing process. The large number of nanochannels in each microchannel provides enough flow rate for bead loading and washing(Details in Chapter 4).

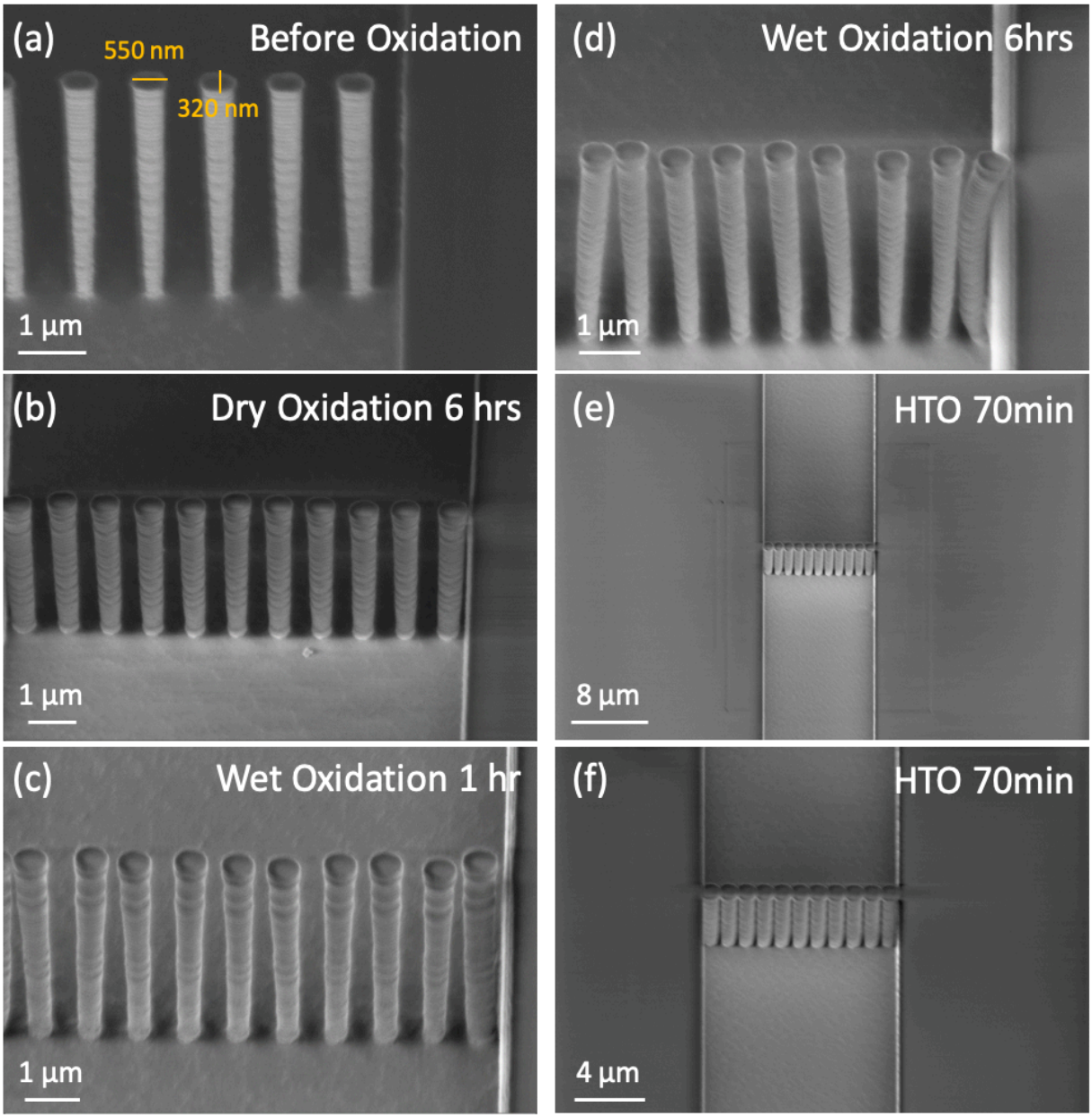

Fig 3.20 SEM of 6.5 µm pillars.

SEM of pillars before (a) and after oxidations(dry oxidation(b), wet oxidation(c,d), and HTO (e,f)). The pillars were 550 nm by 320 nm(600 nm x 400 nm on mask) and approximately 6 µm tall. The gaps between pillars were approximately 300 nm (250 nm on the mask), although the gap sizes at bottom are obviously larger. (b-d) Neither dry nor wet oxidation could close the gaps, due to the limited volume of silicon to oxidize on each pillar as well as the slow oxidation rate. HTO could successfully fill up the gap between pillars (e,f).

Chapter 4: Ion concentration polarization (ICP) of proteins at silicon micropillar nanogaps

Adapted with permission from:

1. Lu B, Maharbiz MM "Ion concentration polarization (ICP) of proteins at silicon micropillar nanogaps " *PLoS ONE.* (in review)

4.1 Abstract

Fast detection of low-abundance protein remains a challenge because detection speed is limited by analyte transport to the detection site of a biosensor. In this paper, we demonstrate a scalable fabrication process for producing nanogaps in vertical nanochannels (nanogaps) which enable ion concentration polarization (ICP) enrichment for fast analyte detection. Compared to horizontal nanochannels, massively paralleled vertical nanogaps not only provide comparable electrokinetics, but also significantly reduce fluid resistance, enabling microbead-based assays. The channels on the device are straightforward to fabricate and scalable using conventional lithography tools. The device is capable of enriching protein molecules by >1000 fold in 10 min. We demonstrate fast detection of IL6 down to 7.4 pg/ml with only a 10 min enrichment period followed by a 5 min incubation. This is a 162-fold enhancement in sensitivity compared to that without enrichment. Our results demonstrate the possibility of using silicon/silica based vertical nanogaps to mimic the function of polymer membranes for the purpose of protein enrichment.

4.2 Introduction

A number of microfluidics based immunoassays have been developed specifically for low abundance target molecules[135], including cantilever-based biosensors[136], surface plasmon resonance (SPR)[137], and nanowire-based immunoassays[34]. However, immunoassays for low concentration proteins remain a challenge because most existing technologies are sensitive to

antibody quality and require relatively long incubation times. The sensitivity of most biosensors depends on the affinity of the capture antibody, implying that high sensitivity biosensors require high quality antibodies with a very low dissociation constant, K_d. In addition, antibody-antigen systems require relatively long incubation times to achieve binding equilibrium. This is especially pronounced at low antigen concentrations [16], particularly at concentrations below the antibody dissociation constant as analyte transport to the biosensor becomes the rate limiting step [12–15]. As a result, incubation times ranging from several hours to overnight are usually necessary for low concentration detection [138]. To overcome these limitations, many sample enrichment technologies have been developed in recent years; these include nano-dispensing [139], size exclusion [45,46], isoelectric focusing [51–54], isotachophoresis [59], amplification stacking [47–50], and dielectrophoresis [55–58]. However, the application of these enrichment methods to immunoassays remains a challenge. Among the difficulties in applying these to immunoassays are the fact that nano-dispensing requires a complex and expensive dispensing system; size exclusion depends on the molecule size; sample stacking and isotachophoresis requires special buffer arrangements; and dielectrophoresis requires an expensive, high quality electronic amplifier with high slew rate, low noise, and high power.

In this context, ion concentration polarization (ICP) has captured tremendous interest in the field of electrokinetic preconcentration of biomolecules [1,61]. ICP-based preconcentrators do not require special buffers and reagents, in contrast to sample stacking and isotachophoresis. ICP methods accumulate biomolecules at the boundary of a depletion zone, regardless of the molecule size [68,76,140,141]. Since ICP-based devices only require DC voltages, they are much simpler and cheaper than those employing dielectrophoresis [55–58]. Because ICP is a phenomenon that exists at the interface between nanochannels and microchannels, ICP-based protein enrichment was originally achieved on silicon or glass substrates using thin horizontal nanochannels [16,60,64–67]. Polydimethylsiloxane (PDMS) and Nafion have also been used for nanofluidic preconcentration devices because the Nafion membrane provides similar permselectivity to silica nanochannels and PDMS is a well-known material for prototyping microfluidics [68,70–78]. For example, the simplest preconcentrator employs a Nafion membrane deposited in the center of a straight PDMS microchannel [72]. The high difference in conductivity between the Nafion membranes and the PDMS microchannel induce ICP, enriching biomolecules at the anodic side of the Nafion film. However, this simple design is hard to replicate on silicon or silica substrates with horizontal nanochannels, since the horizontal nanochannels alone cannot provide sufficient volumetric flow for immunoassay operations such as sample loading and washing. Thus, in most silicon/silica preconcentrators the horizontal nanochannels must be perpendicular to larger microchannels [16,60,64,66], which results in a more complex structure. Importantly, while PDMS/Nafion devices are excellent for prototyping (i.e. production in the tens of devices per day), silicon/silica-based devices are easier to scale up to high volumes (i.e. tens of thousands of devices per day) given modern photolithography tools and processes.

In this paper, we demonstrate a silicon/silica based preconcentration device with 397 micropillars forming 398 vertical nanogaps between them. The presented process has specific advantages when compared to previous silicon/silica nanochannel designs which require horizontal nanochannels as well as polymer membrane devices. One of the advantages of the silicon / silica fabrication process presented in this paper is that it allows for a design in which both the microfluidics and nanopillar concentrators are fabricated simultaneously and in-plane.

The large number of nanogaps that can be fabricated in parallel in one flow channel, coupled with a short channel length (1 μm) provide sufficient volumetric flow to allow for this simple design. Taken together, the nanogaps act as a silicon/silica-based membrane in-line with the microchannel flow. The only comparably simple design previously reported requires a Nafion-based preconcentrator [72]. Compared to polymer membrane devices, the presented fabrication process is more compatible with conventional lithography tools and cleanroom processes, making it amenable to scale-up to high volumes [16,60,64–67].

Furthermore, a combined pre-concentrator / filter design allows for bead-based immunoassays, as the micropillars both induce ICP and stop functionalized beads in the ICP enrichment zone. In contrast, most previously reported designs use separate features to perform enrichment and capture beads. For example, in Wang et al. [16], an additional shallower channel was fabricated to stop microbeads in front of the silica-based horizontal nanochannels; this requires additional mask alignment and etching steps. Likewise, in Ko et al. [71], additional sets of pillars were fabricated into their device to capture beads in front of Nafion membranes.

In our device, the coupling of ICP and electroosmotic flow (EOF) results in the accumulation of biomolecules in front of the pillars (detailed schematic diagram of mechanism in Fig 4.1). In effect, the array of nanogapped pillars mimics the function of a semi-permselective membrane that prefers to transport cations rather than anions, given that the silica surface is negatively charged in phosphate buffered solution (PBS) at pH=7.4. The permselectivity of silica nanogaps originates from surface conduction through the electrical double layer (EDL), which in microchannels is usually overwhelmed by bulk conduction. However, surface conduction becomes significant when the channel size is comparable to the thickness of the EDL. For example, if one were to fabricate nanoscale channels, the ratio of EDL thickness to channel width would increase by three orders of magnitude when compared to the effect in a microscale channel. It follows that the ratio of surface conductivity to bulk conductivity would also increase by three orders of magnitude (Dukhin number [46]).

Note that our nanogaps do not perform as a perfect ion selective membrane. The thickness of the EDL with 0.1X and 1X PBS is approximately 3 nm and 0.8 nm [61,64], respectively, both of which are significantly smaller than the size of our nanogaps (30 nm). There are two relevant conduction phenomenon in our nanogaps: *bulk* conduction - transporting both cations and anions and *surface* conduction - transporting mostly cations through EDL. At this scale (channel width ~10x larger than EDL thickness), the cations transported by surface conduction initiate a weak concentration polarization and decrease ion concentration on the anodic side of the nanostructure [1,61]. The lower ion concentration near the nanogaps increases the thickness of local EDL and enhances permselectivity which contributes to faster concentration polarization. Thus, the concentration polarization in our device depends on a positive feedback process [61] which develops strong ICP even at moderate (0.1X PBS, ~15 mM) ionic strength (i.e. buffers for which the Debye length is significantly shorter than the nanogap width). The low ion concentration region (depletion zone) induces nonequilibrium space charge layers, resulting in accelerated nonequilibrium EOFs in the vicinity of the nanostructures [64,142,143]. Due to the incompressibility of the fluid, strong vortical flows are generated in the depletion zone, driving the fluid back to the upstream [1,61,144,145]. At the same time, the low ion concentration amplifies the electric field in the depletion zone, repelling negatively charged biomolecules away from the

nanostructures. The backflow of the vortices along with the strong electric field work jointly to move biomolecules upstream until the convective and electromigratory velocity balance, resulting in the continuous accumulation of biomolecules (Fig 4.2h) [62,144].

To demonstrate the bead immunoassay possibilities of our device, we chose interleukin 6 (IL6). IL6 is a proinflammatory cytokine and serves as an important mediator during the acute phase response to inflammation in sepsis. Its concentration in blood is used as a diagnostic for sepsis [19,20] and is significantly positively correlated with septic patient mortality rate [21]. As a life-threatening disease caused by systemic immune response, septic patients usually need immediate treatment. The ability to monitor IL6 levels time scales in the tens of minutes would open the door to closed loop, patient-specific sepsis management [55–57].

4.3 Device Fabrication

The preconcentration device is formed from two parallel channels connected by microchannels which contain the nano-gapped pillars; four reservoirs provide tubing and electrode connections (Fig 4.2a). During enrichment, one channel (left) is connected to the anode while the other channel (right) is connected to the cathode. As shown in Fig 4.2(b-d), the microchannels are 700 µm long, 30 µm wide and 6.5 µm deep and contain 397 micropillars. Each micropillar has a cross section of approximately 1 µm by 1 µm and the same height as the microchannels. The gaps between micropillars are 30 nm wide, forming 398 nanogaps.

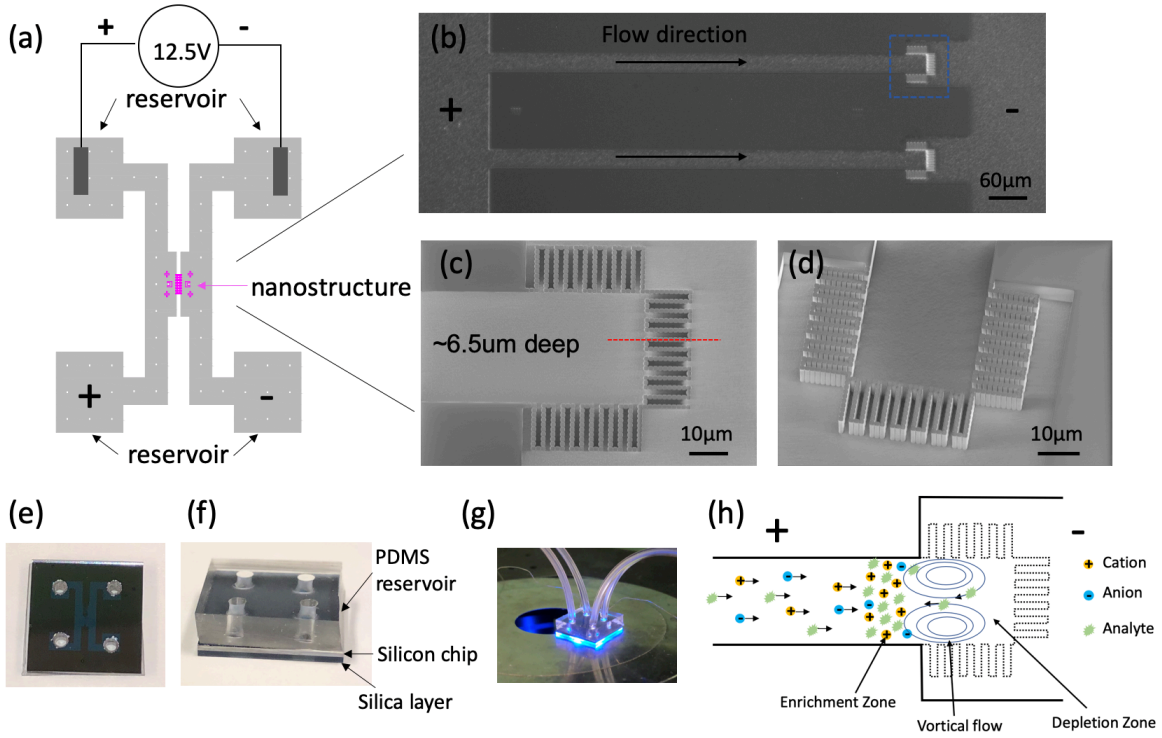

Fig 4.2 Overview of the preconcentration device.

(a) Schematic diagram of the entire device. Two main channels (each with two reservoirs) are connected by the microchannels with nanogaps in the middle. The reservoirs are used to connect external fluidic tubing with the microchannels and to provide contact with electrodes. (b) Close-up of the microchannels connecting the two main channels. These microchannels are 700 µm long, 30 µm wide, 6.5 µm tall, and contain 397 micropillars at one end. Nanogaps between micropillars are approximately 30 nm wide and induce ICP to enrich target proteins. (c) Top view. (d) 30^o off-axis. SEM of the nanostructures in the blue box in (b). There are in total 397 micropillars (1um x 1 um x 6.5 um) forming 398 nanogaps. (e)-(g) Pictures of finished chips. Each chip has three layers, PDMS layer for tube connection, silicon layers with all the micro/nano structures, and silica layer for sealing purpose. (h) Schematic of ICP and protein enrichment in front of nanostructures with the anode on the left side.

All structures are fabricated in the silicon substrate. We chose silicon micromachining instead of PDMS molding because a high aspect ratio is achievable when etching silicon. The finished devices have three layers as shown in Fig 4.2e & 1f. The fabricated silicon device is sealed with a silica wafer spin coated with polysilsesquioxane (PSQ) and this transparent side enables fluorescence detection. A thick layer of PDMS with four through-holes is bonded on the other side of the silicon layer to form the reservoirs for tube and electrode connection (Fig 4.2g).

Microchannels (including micropillars) were fabricated on a p-type prime silicon wafer (Fig 4.3a). A 420nm thick layer of deep ultraviolet (DUV) photoresist (UV210-0.6, Dow Chemical, Midland, MI) was spun on a silicon wafer and then exposed in ASML 5500/300 (ASML, Veldhoven, Netherlands). The exposed photoresist was then developed in Megaposit MF26A (Dow Chemical, Midland, MI) and hard baked for 2 hrs at 120ºC. The silicon wafer was etched 6.5 µm deep with deep reactive-ion etching (DRIE) in an ICP (inductively coupled plasma) etcher (SPTS Technologies, Newport, UK). Ideally, deeper nanogaps would give better results, but we were constrained to 6.5µm depths by the aspect ratio limits of the etch recipe. After spin coating a 10 µm thick layer of photoresist (SPR 220-7.0, Dow Chemical, Midland, MI) to protect surface structures, reservoirs were ground manually with a dental drill to create access holes through the silicon. This step could be replaced by RIE or KOH etching for scaled up manufacturing [16,60]. Because the minimum lithographically-defined linewidth was 250 nm (Fig 4.3b & 2d), the next step was to shrink the nanogaps from 250 nm to ~30 nm by oxide deposition. Since we had high aspect ratio structures, a highly conformal deposition process was used to achieve uniform deposition over the micropillars. We deposited a layer of high-temperature oxide (HTO) at 900^o C over the etched devices with a TYTAN Diffusion Furnace System (Tystar, Garden Grove, CA) to achieve ~30 nm wide nanogaps (Fig 4.3c & 4.3e). Note, it is important to deposit oxide after reservoir grinding. Otherwise, the newly grinded reservoirs would expose the conductive silicon substrate inside the reservoirs and create an electrical short circuit when wet.

After the fabrication of all features on the silicon wafer, a PSQ (Gelest, Morrisville, PA) coated silica wafer (500 µm thick) was used to seal the channels. PSQ has a similar chemistry to PDMS, able to form covalent bonds with a silicon dioxide surface after plasma treatment and has been used for silicon/silica based device sealing previously [56,120,121]. PSQ was chosen over PDMS for our device because commercially-available PSQ has higher strength and is more amenable to dilution and spin coating. We used a PSQ sealing process adapted from that reported by Gu et al [120]. PSQ was diluted in xylene in a 3:2 ratio and then spin-coated on an oxygen

plasma cleaned silica wafer at 3000 RPM for 1 min. After spin-coating, the silica wafer was baked overnight at 150°C. The hard-baked silica wafer and processed silicon wafer were then O_2 plasma treated at 100 W for 60 seconds in a YES-G500 Plasma Cleaning System (Yield Engineering Systems, Livermore, CA). The plasma power and time were crucial to properly activate the surface and form covalent bonds between two surfaces. We found that high-energy plasma damaged the structure of the PSQ and weakened wafer bonding. Similarly, long duration plasma exposure likely reduced the number of effective silanol groups via back-biting scission reactions. These two effects are well-known in PDMS plasma bonding processes [122]. This bonding process can be replaced by anodic bonding for scale-up [16,60]; at lab scale, PSQ mediated bonding is easier and faster. After plasma treatment, the two surfaces were brought in contact immediately. After wafer bonding, the wafer was diced into 1 cm by 1 cm chips as seen in Fig 4.2e, and then a thick layer of PDMS with 4 through-holes was bonded to the backside of the chip after a backside O_2 plasma treatment. This layer enabled connections between the tubing and the reservoirs.

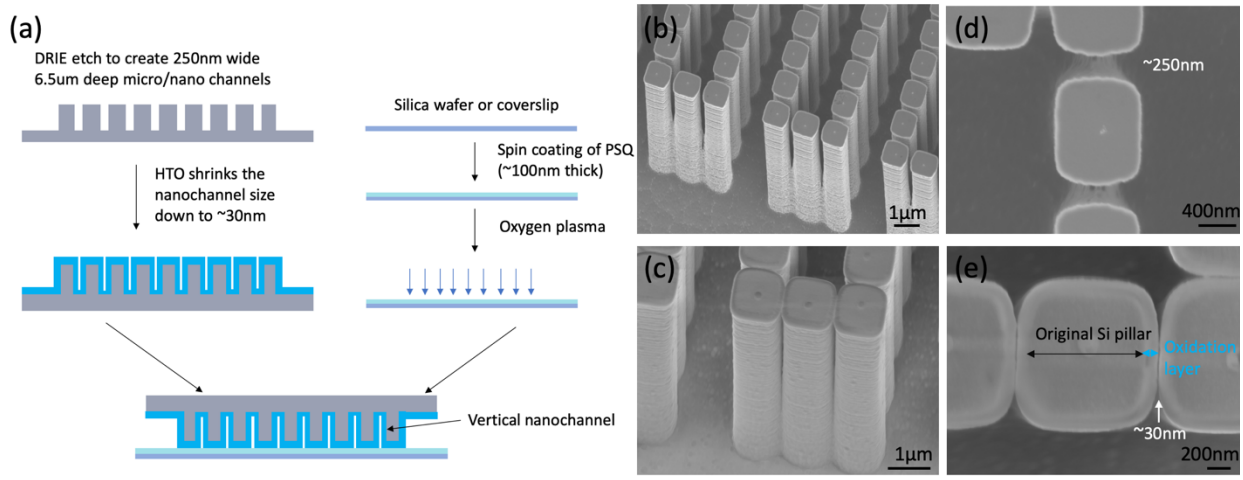

Fig 4.3. Fabrication of the nanofluidic device.
(a) Schematic cross-section of fabrication process at the red line shown in Fig 4.2c. All channels and pillars were 6.5 µm tall and etched in one single DRIE step. (b)&(d) SEM of micropillars before HTO. (c)&(e) SEM of micropillars after HTO. The additional silicon dioxide layer increased the pillar size and reduced the nanogap size.

4.4 Materials and Methods

For characterization experiments, Strep-647(Alexa-Fluor 647 conjugated streptavidin, Thermal Fisher Scientific, Waltham, MA) was used as the sample protein for preconcentration characterization in PBS (0.1X and 1X PBS, pH=7.4) solution. We also added 0.1% Tween-20 (Thermo Fisher Scientific, Waltham, MA) in all solutions in this paper to reduce non-specific binding on side walls. In the experiments that varied voltage (25V, 12.5V, 5V) and strep-647 concentration (200ng/ml, 20ng/ml, 2ng/ml), we used 0.1X PBS (pH=7.4) with 0.1% Tween-20.

For experiments employing fluorescent IL6, recombinant mouse IL6 (Thermo Fisher Scientific, Waltham, MA) was labeled with Alexa-Fluor 488 using the Microscale Protein Labeling Kit (Thermo Fisher Scientific, Waltham, MA). All labeled IL6 (IL6-488) preconcentration experiments were performed in 0.1X PBS (pH= 7.4,7.8,9) with 0.1% Tween-20 at 25V. Sodium hydroxide (NaOH) were used to adjust the pH of 0.1X PBS solution. Both labeled and non-labeled IL6 were diluted in 0.1X PBS (pH=7.8) with 0.1% Tween-20 at 25V for bead-based immunoassays, while a washing buffer was created with 1X PBS with 0.1% Tween-20. Strep-647 and detection antibody (BD Bioscience, San Jose, CA) were diluted in the washing buffer at the concentration of 2 µg/ml and 1 µg/ml, respectively, in immunoassays for non-labeled IL6. BSA-488 (Alexa Fluor 488 conjugated bovine serum albumin, Thermo Fisher Scientific, Waltham, MA) and BSA-647 (Alexa Fluor 647 conjugated bovine serum albumin, Thermo Fisher Scientific, Waltham, MA) were used as tracers for non-labeled IL6 and labeled IL6, respectively.

Carboxyl group-coated polystyrene microbeads (~4.6 µm diameter, Spherotech,Lake Forest, IL) were conjugated with capture antibody of mouse IL6 by conventional EDC (1-Ethyl-3-(3-dimethylaminopropyl)-carbodiimide, Thermo Fisher Scientific, Waltham, MA) and Sulfo-NHS (N-hydroxysulfoxuccinimide, Thermo Fisher Scientific, Waltham, MA) chemistry. Briefly, EDC and Sulfo-NHS were first dissolved in 0.05M MES buffer (Thermo Fisher Scientific, Waltham, MA) and immediately added to 0.5% w/v microbeads solution in DI water. The mixed solution was incubated for 15 min at room temperature, which was followed by centrifugation and wash in DI water with 0.1% Tween 20 in order to remove excessive EDC and Sulfo-NHS. Tween-20 prevented microbeads from aggregating and adhering to centrifuge tube surfaces during centrifugation. Because Sulfo-NHS hydrolyzes in water spontaneously, the washing process had to be fast. After washing at least 3 times, anti-IL6 capture antibody (BD Biosciences, San Jose, CA) was added into the microbead solution and incubated for 2 hrs at room temperature. Then, quencher solution, 50% w/v hydroxyl amine (Sigma-Aldrich, St. Louis, MO), was added into the mixture and incubated for another 10 min to deactivate the remaining NHS, after which the microbeads were washed again in DI water with 0.1% Tween-20. Before using the antibody conjugated microbeads, we blocked the microbeads by incubating in 1% BSA (bovine serum albumin, Thermo Fisher Scientific, Waltham, MA) for 1 hr at room temperature.

All fluorescent images were taken on an inverted fluorescent microscope (Nikon Eclipse Ti, Nikon Instruments Inc, Melville, NY) with a CCD camera such that the anode was on the left side and the cathode on the right side of the image. Platinum wires (0.13mm in diameter, A-M System, Sequim, WA) were used as electrodes to apply voltage to each reservoir. A waveform generator (Keysight,Santa Rosa, CA) connected to an amplifier (Tegam, Geneva, OH) was used to apply DC Voltage. ImageJ was used for image analysis.

4.5 Results

4.5.1 Lower ionic strength results in stronger enrichment

We characterized the preconcentration phenomenon under different conditions in order to find the optimal ionic strength, voltage, and pH. Fig 4.4a shows the protein enrichment behavior under different ionic strengths of buffer solution (0.1X and 1X PBS). Strep-647 at a concentration of 200 ng/ml was used as the fluorescent tracer. When applying a 12.5 V DC voltage, we could observe the formation of an enrichment zone on the anodic (left) side of nanogaps. As soon as no voltage applied, accumulated strep-647 molecules easily leak through the nanogaps with positive pressure from anodic side. Note that the streptavidin molecules (~5 nm diameter [61]) are much smaller than the nanogaps: enrichment is caused by the development of ICP instead of size filtering. As shown in Fig 4.4a, detectable accumulation of strep-467 occurred after 1 min in 0.1X PBS, but was not detectable until 5 min in 1X PBS. After 10min, the intensity saturated in 0.1X PBS, while the intensity in 1X PBS was only approximately 30% of the saturated level.

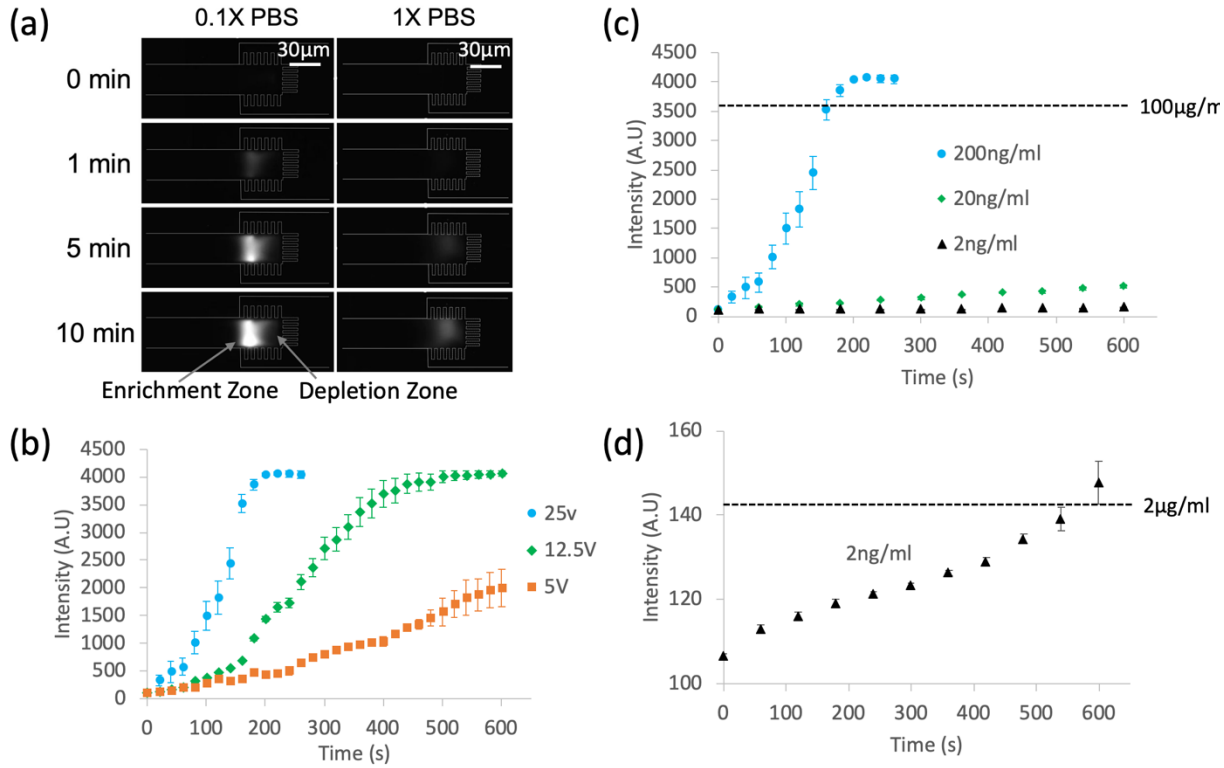

Fig 4.4 Characterization of protein enrichment.

(a) Protein (200 ng/ml Strep-647) enrichment in different ionic strengths (0.1X & 1X PBS with 0.1% Tween-20). ICP based protein enrichment is much more effective in 0.1X PBS than in 1X PBS. A DC voltage of 12.5V was applied across the channels with anode on the left side and cathode on the right side. (b) Enrichment speed as a function of the applied DC voltage (5 V, 12.5 V and 25 V). Higher voltage leads to faster enrichment of 200 ng/ml Strep-647 solution. (c) Enrichment over 10min with various Strep-647 concentrations at 25V. (d) Closeup view for the 2ng/ml Strep-647 experiment in (c). Note the ~1000 fold enrichment in 10min. All sample solutions in (b-d) were diluted in 0.1X PBS with 0.1% Tween-20.

4.5.2 Higher voltage leads to faster enrichment

We also investigated the preconcentration effect as a function of the applied DC voltage. Fig 4.4b shows that higher voltage leads to faster preconcentration. It took 600 s to achieve a 2000 A.U intensity at 5 V, while it took approximately 240-260 s and 120 s at 12.5 V and 25 V, respectively, to reach the same intensity. In this voltage range, the enrichment speed is roughly proportional to the voltage, which is in agreement with the theoretical relationship between EOF and applied voltage.

4.5.3 The preconcentrator achieves 1000-fold enrichment

After determining the optimal ionic strength and voltage, we characterized the enrichment phenomenon with various concentrations of strep-647. Fig 4.4c & 4.4d shows the preconcentration performance for strep-647 at 25 V in 0.1X PBS (pH=7.4) with 0.1% Tween-20. Fig 4.4c shows the enrichment of strep-647 at initial concentrations of 200ng/ml, 20 ng/ml, and 2 ng/ml over 10 min. During the preconcentration, one fluorescent image was taken every minute. Between image captures, the shutter for the excitation light was closed to prevent photobleaching. Fig 4.4d is a closer look at the 2ng/ml group in Fig 4.4c; for reference, the horizontal dashed line represents the signal intensity of a 2 µg/ml strep-647 solution. As we concentrated the proteins, the fluorescent intensity of the initially 2 ng/ml solution increased and exceeded the intensity level of the 2 µg/ml reference within 10 min; this is indicative of a 1000-fold enrichment.

4.5.4 IL6 can be enriched with pH adjustment

Before integrating immunoassays into our device, we used IL6-488 to demonstrate that the preconcentrator could enrich not only streptavidin but also IL6. However, there was no enrichment of IL6-488 in 0.1X PBS at pH=7.4, as shown in Fig 4.5a. The IL6-488 enrichment was then tested at higher pH (pH= 7.8, 9). Because the IL6 molecules are more negatively charged at higher pH, we expected them to accumulate more easily within the depletion zone(Fig 4.5a). Note that the antigen-antibody reaction is negatively affected by higher pH (pH > 8), which reduces the affinity of antibodies [69]. We tested the antibody activity by incubating IL6 with antibody-conjugated beads at various pH(pH=7.4, 7.8, 9). For the same concentration of IL6, the signal intensity on beads was at least 60% lower at pH=9 compared to that at pH=7.4 due to the lower affinity of the antibody at higher pH(Fig 4.6). Thus, for all of the following immunoassays, we chose the lowest pH (pH=7.8) that promoted enrichment but did not reduce intensity below about 90% of the intensity observed at pH 7.4.

4.5.5 BSA-647 is a good fluorescent tracer for IL6 preconcentration

In order to monitor the development of ICP and an enrichment zone in the IL6 immunoassay, we used a fluorescent tracer for IL6. We required a fluorescent tracer that 1) enriched along with IL6, 2) accumulated at the same location as IL6, and 3) did not interfere with other reagents in the immunoassay. As shown in Fig 4.5b, when enriched simultaneously along with IL6-488 in the same solution, BSA-647 enrichment zone was colocalized with the enrichment zone of IL6-488. Therefore, we used BSA-647 as our fluorescent tracer for IL6 immunoassays at pH=7.8.

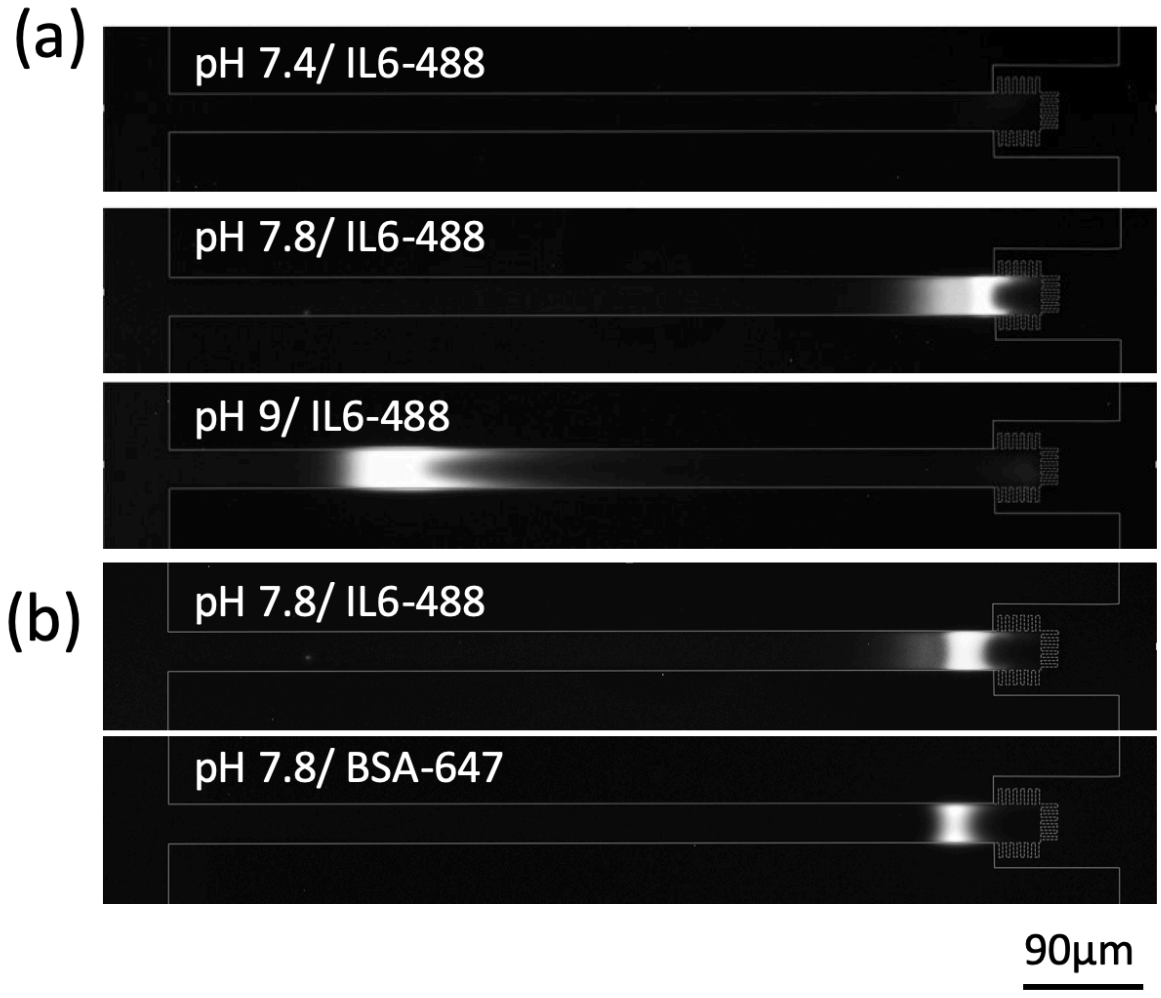

Fig 4.5 BSA is a good tracer for IL6 preconcentration.
(a) The enrichment performance of IL6-488 under various pH. Sample solution (0.1X PBS, 0.1% Tween-20, 2µg/ml IL6-488 at pH= 7.4, 7.8, 9) was loaded into the device and 25V was applied to the reservoirs for 10min. (b) BSA-647 could be used as a good tracer for IL6 enrichment. Both BSA-647 (200 ng/ml) and IL6-488 (2 µg/ml) were enriched simultaneously at 25V in the same sample solution as (a) except the pH=7.8. The enrichment zone of BSA-647 was highly colocalized with the enrichment zone of IL6-488. To maintain the activity of IL6, we used a low degree of labeling for IL6-488 (less fluorescent molecules per protein molecule). Thus, we used 10 times higher concentration of IL6-488 than BSA-647 for characterization experiments.

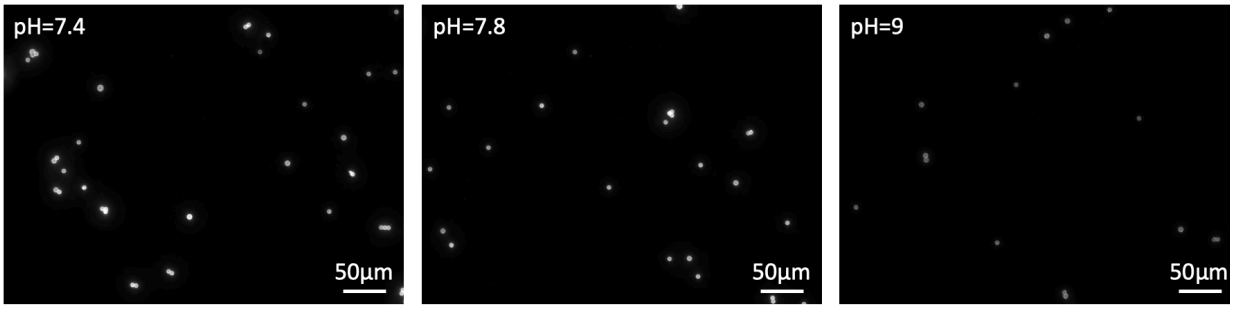

Fig 4.6 Higher pH negatively affects antibody-antigen reaction.
In this experiment, microbeads were incubated with 200 ng/ml non-labeled IL6 for 2 hr, followed by the incubation in detection antibody and strep-647, respectively. The IL6 solutions were prepared at different pH. The intensity of microbeads at pH=9 is more than 60% lower than that at pH=7.4.

4.5.6 Nanogap preconcentrator enables bead-based immunoassays

To demonstrate the compatibility of this method with bead-based immunoassays, we conjugated polystyrene microbeads (4.6 µm in diameter) with rat anti-mouse IL6 capture antibody. Since the microbeads were smaller than the height of the microchannels but much larger than the nanogaps, all microbeads were stopped at the pillars. Smaller beads (100 nm – 2 µm in diameter, data not shown) also stopped at the pillars, but we chose ~4.6 µm diameter beads because the larger size provided better observation and control over the number of beads per microchannel. In addition, beads with submicron size could potentially partially block the nanogaps and decrease the effective nanogap size, which would significantly affect enrichment behavior.

The immunoassay process is shown in Fig 4.7. First, approximately five microbeads were loaded into each microchannel, followed by the loading of IL6-488 sample solution. DC voltage was applied for 10 min at 25 V. Note, similar to other ICP based preconcentrators[60,61,64,65,71,72,74,146], we also observed vortical flow in the depletion region so that microbeads moved along with the vortical flow during enrichment. The location of microbeads in Fig 4.7c & 5d is , therefore, different from the location in Fig 4.7a. The microbeads were incubated for five minutes after turning off the voltage (Fig 4.7b & 4.7c). Since the nanogaps restricted diffusion, IL6-488 diffusion was slower in the nanostructures than in an open microchannel (where molecules can diffuse freely in both directions). Thus, after a 5 min incubation, the elevated fluorescent signal (Fig 4.7c) was ~75% lower than the signal immediately after turning off the voltage (Fig 4.7b), but it was still more than 50x higher than the background. This result demonstrated that without additional convection, IL6 molecules did not diffuse away immediately. This additional 5 min incubation improved antigen-antibody binding and noticeably enhanced signal intensity [72], after which a positive pressure was applied through anodic side to wash away excessive fluorescent molecules (Fig 4.7d) .

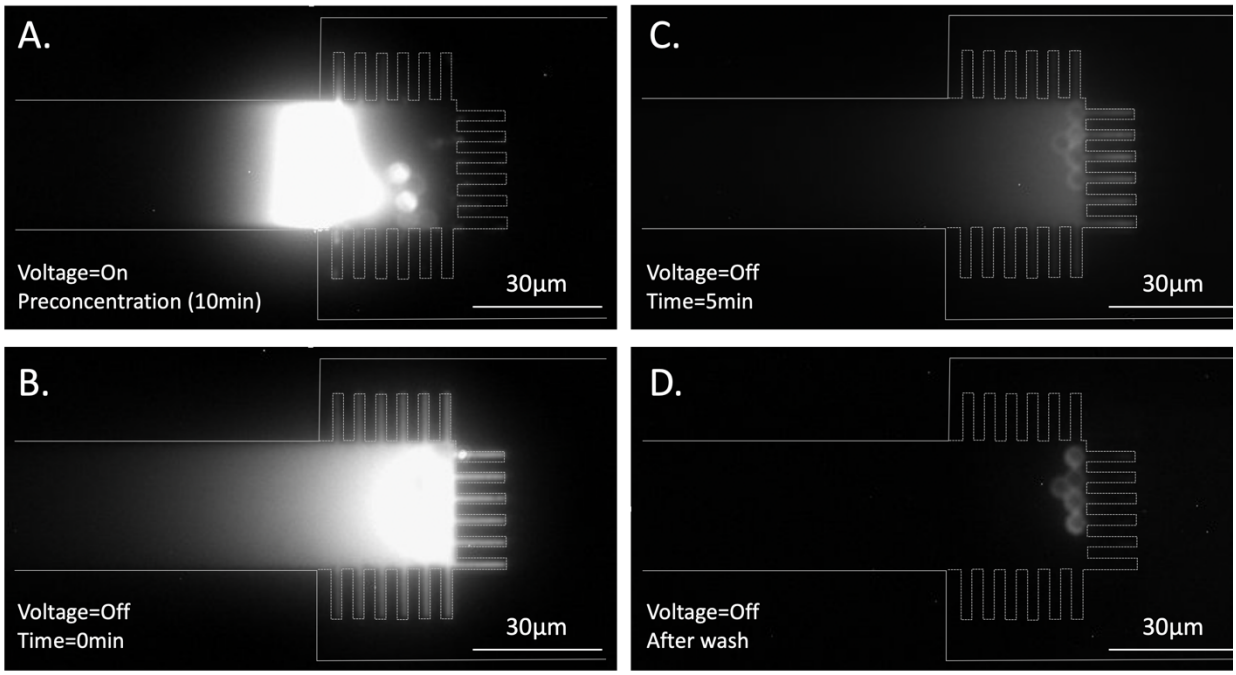

Fig 4.7 Immunoassay procedures for IL6-488.
(a) Bead loading (~5 microbeads per microchannel) and preconcentration of IL6-488 at 25V for 10 min in sample solution (0.1X PBS, 1% Tween-20, 500 ng/ml IL6-488, pH=7.8). Immediately after turning off the voltage (b), the enrichment molecules started diffusing away toward both sides. Since the nanogaps restricted diffusion, the diffusion to right side was slower. Thus, even 5 min after turning off the voltage, a higher (50X higher than background) fluorescent signal was detectable in front of the nanostructure (c), although it was ~75% weaker than the signal immediately after turning off the voltage (b). (d) After 5min incubation, a positive pressure was applied through anodic side reservoirs to wash away excessive IL6-488.

The detection of non-labeled IL6 uses the same process as IL6-488 detection, except that biotin conjugated detection antibody and strep-647 were loaded after loading IL6. An additional washing step was necessary between the loading of detection antibody and strep-647, since the mixture of these two reagents might induce micro-aggregation and block the nanogaps. The dose response curves of both labeled and non-labeled IL6 are shown in Fig 4.8. Two inset fluorescence images show the saturated signals for each case. Fluorescent signals were normalized using the saturated signal and zero dose signal as 100% and 0% intensity. We used the four parameter logistic model in Eq. 1 to fit the dose response curves which models the physicochemical mechanism of antigen-antibody binding

$$y = d + \frac{a-d}{1+(\frac{x}{c})^b} \qquad \text{Eq.1}$$

where y is the fluorescent intensity, x is the target concentration, d represents the intensity at infinite concentration, a is the estimated intensity at zero concentration of target, b is the Hill

coefficient referring to the steepness of the curve, and *c* is the midrange concentration [71,147]. All fitted curves had R^2 (coefficient of determination) values larger than 0.98. Three standard

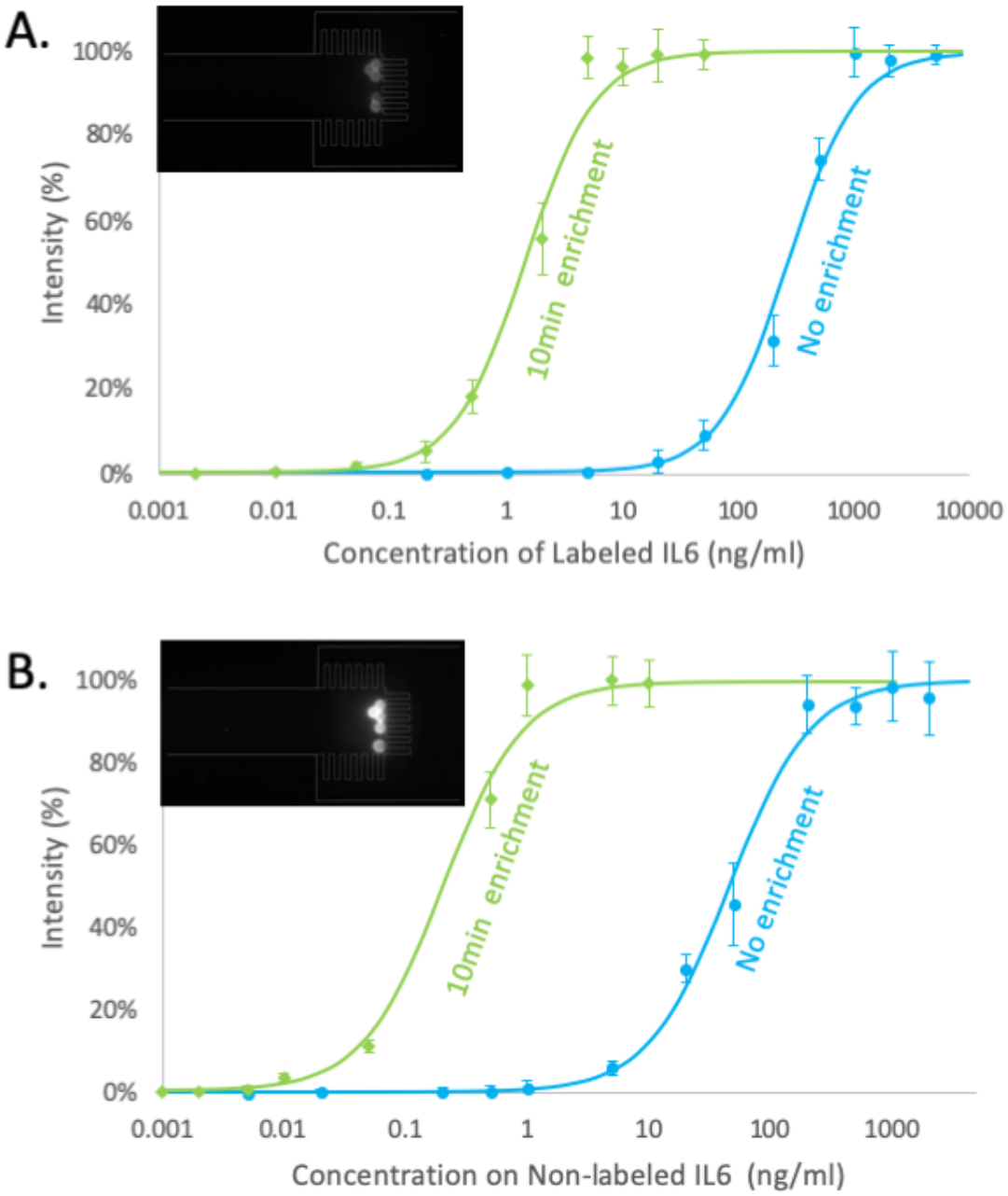

Fig 4.8. Dose response of the immunoassay with and without preconcentration. *Immunoassays for (a) IL6-488 and (b) non-labeled IL6 were performed on beads with (green curve) and without (blue curve) enrichment. The sensitivity of IL6-488 and non-labeled IL6 detection was enhanced ~125 fold and ~162 fold, respectively. The in-plot fluorescence images show saturated signals for IL6-488 (a) and non-labeled IL6 (b). Both labeled and non-labeled IL6 preconcentration was conducted with the same sample solution (0.1X PBS, 1% Tween-20,*

pH=7.8), DC voltage (25 V) and duration (10 min). BSA-647 or BSA-488 (200 ng/ml) was used as the tracer protein and simulated molecular background for labeled and non-labeled IL6, respectively. Both of the non-enrichment groups were incubated in tubes for 2 hrs at room temperature in the same sample solution.

deviations above the background signal was used to define the limit of detection (LOD). Using these curves, the LOD of labeled and non-labeled IL6 without enrichment was 15ng/ml and 1.2ng/ml, respectively. After 10 min enrichment, the LOD of labeled and non-labeled IL6 was enhanced to 120 pg/ml (~125 fold improvement) and 7.4pg/ml (~162 fold improvement), which is comparable to the 500 fold enhancement in 60 min (30 min enrichment plus 30 min additional incubation) from the previously reported straight PDMS/Nafion microchannel design [72].

4.6 Discussion

The weaker enrichment observed for 1X PBS vs. 0.1X PBS (Fig 4.4a) is likely due to the higher ionic strength of the solution. A higher ionic strength solution would exhibit a thinner EDL and, therefore, slower electroosmotic flow (assuming the same DC voltage applied) and a smaller ratio of surface conductivity to bulk conductivity. Thus, it takes longer to develop a low concentration region near the nanogaps and accumulate target molecules. Interestingly, no fluorescent signal was found for 0.01X PBS. One possible reason is that this much lower ion concentration promotes strong ICP immediately and a depletion zone develops which is longer than the microchannel, preventing protein enrichment.

Also of interest is that for voltages of 5 - 25V, the enrichment rate of our preconcentrator is proportional to the voltage, because higher electric potential results in higher electroosmotic flow rate. Electroosmotic flow is the principal effect bringing proteins to the enrichment zone from bulk areas. Thus, a higher electroosmotic flow rate accelerates the protein accumulation process. However, if the voltage is too low (< 2V), the depletion zone did not fully develop and was not effective at preventing analytes from moving downstream [62]. When the voltage was higher than 50 V, the EOF overwhelmed the ICP-based enrichment so the enrichment zone became unstable. Consequently, strep-647 molecules leaked through nanogaps frequently. In addition, when the voltage was very high (>100 V), background proteins (such as the BSA used in the immunoassays in section 3.6) started to aggregate and to block the nanogaps (Fig 4.9). This may be due to pH changes [148] or ohmic heating [149–152] but further investigation is needed to be certain.

Unlike Strep-647 (pI ~5.5 [153]), IL6-488 (pI ~6.96 [154]) could not be enriched at pH 7.4. We believe this is because the pI value of mouse IL6 is very close to the pH of PBS (pH=7.4); thus, mouse IL6 molecules are either not charged or weakly charged in PBS. According to the mechanism of ICP-based enrichment, neutral molecules cannot be trapped efficiently in front of the depletion zone [61]. In contrast, IL6-488 was successfully enriched at higher pH (pH = 7.8, 9). There are two possible reasons. First, more silanol groups on silica surface are deprotonated in higher pH [155]. The higher charge density on nanogap surfaces leads to higher surface conductivity, which enhances ICP development. Second, the higher pH also leads to more

negatively charged IL6-488 molecules, so that the depletion zone can trap IL6-488 molecules more efficiently, preventing them moving downstream [1]. At pH=9, the enrichment zone was approximately 450µm away from the nanostructure (Fig 4.5a), which was only 36µm at pH=7.8. This is likely due to higher surface charge density producing stronger ICP development and the depletion zone propagating further at pH=9. In addition, increasing pH increases the electrophoretic mobility of protein molecules (i.e. more negatively charged at higher pH), so that the vortical flows carry these molecules further back to the location of lower electric field, where the convection and electromigration balance [68,140].

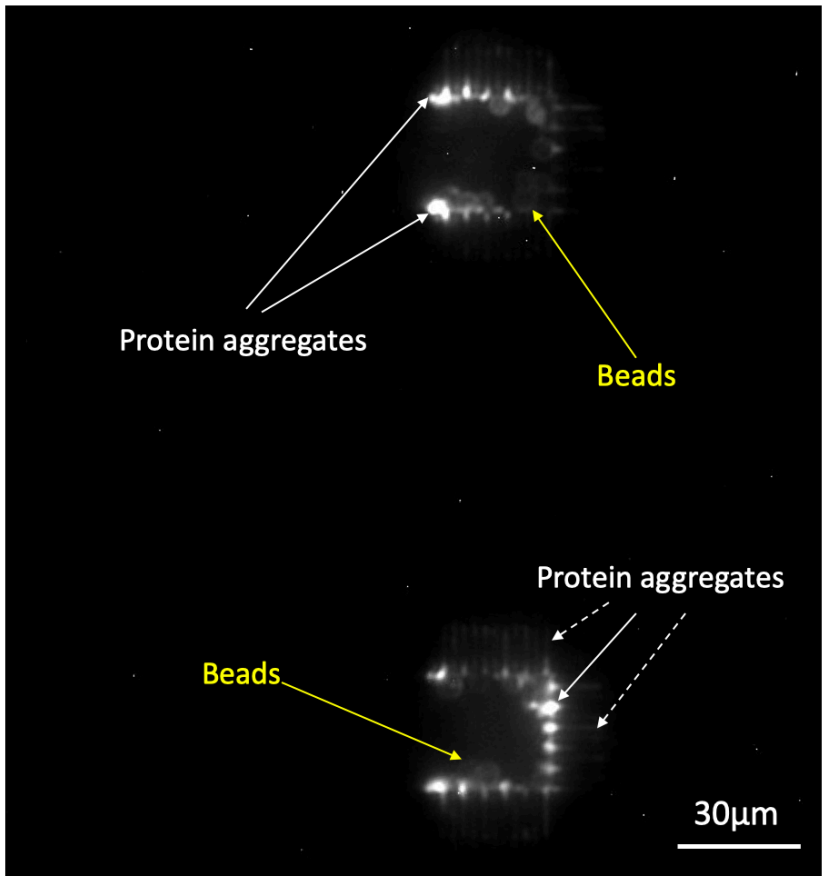

Fig 4.9 Protein aggregation induced by high voltage.
This experiment was conducted with the same immunoassay process described in the paper, except that the DC voltage used for enrichment was 100 V. Yellow arrow point at beads and white arrows indicate the protein aggregates. Nanostructure should be non-fluorescent. We can see the nanostructure in this image because the nanochannels were completely blocked by a layer of protein aggregates, indicated by white dashed arrows.

Lastly, the saturated signal for non-labeled IL6 (Fig 4.8b inset image) was much higher than the saturated signal for labeled IL6 (Fig 4.8a inset image). There are three possible reasons for this. First, since each detection antibody molecule has multiple biotin sites and each strep-647

molecule has multiple fluorophores, this combination amplifies the signal. Second, we used a lower degree of labeling for IL6 so there were fewer fluorophores per IL6 molecule. Third, the labeled IL6 and non-labeled IL6 used different fluorescent molecules for detection. The Alexa Fluor 647 on Strep-647 (for non-labeled IL6) is generally brighter than the Alexa Fluor 488 on IL6-488.

Although we successfully enriched IL6 and enhanced the sensitivity by more than 2 orders of magnitude, the sensitivity enhancement factor was still lower than the concentration factor, which was at least 1000 times greater than initial concentration. This might be result of the local pH change, ohmic heating and the change in buffer ionic strength during preconcentration [72]. However, more investigation is needed to identify which factor plays the main role.

4.7 Conclusion

In summary, we demonstrated the use of nanogaps fabricated between micropillars to mimic a semi-permselective membrane for the purpose of ICP-based target molecule preconcentration. Since the nanogaps have a high ratio of surface conductivity to bulk conductivity, ICP based protein preconcentration was generated on the anodic side of the micropillars. The large number of short vertical nanogaps allowed sufficient volumetric flow for bead loading and washing, which is not possible for conventional horizontal nanochannels. This structure is comparable in performance to preconcentration microchannel designs using Nafion film [72] but is more amenable to large scale fabrication. We also demonstrated a preconcentration-enhanced immunoassay for the detection of IL6. This structure and preconcentration mechanism can be useful to improve the efficiency and the multiplexing capability of silicon/silica based preconcentrators. The performance of this device can be tuned by increasing the number or changing the dimensions of the pillars without changing the fabrication process. We expect this assay can be used for a broad range of analytes and a variety of detection methods. For example, this device can be combined with faster label-free detection methods to further speed up assays and eliminate the additional fluid control needed for bead loading and washing.

Chapter 5: Conclusions and Future Outlook

Miniaturized biomolecular detection is a fast-growing field that has been extensively studied over the past couple decades. With the advances in micro- and nano-fabrication techniques, microfluidic devices have acquired many advantages over laboratory-scale equipment such as fast detection, minimal consumption of samples, compatibility with portable diagnostic solutions, high efficiency, and low cost. Microfluidic biomolecular detection is particularly important in disease diagnostics, improving the effectiveness of treatment and human life expectancy. However, many low abundant biomarkers such as early stage cancer biomarkers and cytokines often demand an extremely low LOD. Thus, a rapid biomolecular detection with low LOD is highly desirable for disease diagnostics.

Most immunoassays demand the use of antibodies and miniaturized devices require precise and submicron-scale antibody immobilization onto the biosensing surfaces. In this thesis, we first demonstrated a new protein nanopatterning technique using Ge as a sacrificial layer, which is compatible with conventional fabrication tools and suitable for low cost and high volume manufacturing of miniaturized biosensors. This technique is of particular utility for surface conjugation chemistries with organic solvents. We reported protein patterning with two different methods of Ge deposition: e-beam evaporation and LPCVD. Sidewall functionalization can be achieved and controlled by using a non-conformal Ge deposition process such as e-beam evaporation, while the Ge films deposited by LPCVD are more conformal and can avoid protein immobilization on sidewalls, which may be preferred for some biosensor applications.

Then, we introduced ICP as the mechanism for rapid analyte enrichment in order to improve the sensitivity of immunoassays without prolonged incubations. The first version preconcentrator was developed on silica substrates using ICP induced enrichment. We improved the performance of our devices from a single 300 nm deep nanochannel to hundreds of 6.5 μm deep nanochannels, from silica substrates to silicon substrates, from surface-based immunoassays to bead-based immunoassays, and from fluorescent streptavidin enrichment to natural IL6 molecules detection. Finally, we showed an ICP-based preconcentrator using hundreds of vertical nanochannels to mimic a perm-selective membrane for analyte preconcentration. The channels on the device are straightforward to fabricate and scalable using conventional lithography tools. The large number of short vertical nanochannels allows sufficient volumetric flow for bead loading and washing directly through nanochannels, which is not possible for conventional horizontal nanochannels. The final device is capable of enriching protein molecules by more than 1000 fold in 10min and detecting IL6 down to 7.4pg/ml with only a 10 min enrichment followed by a 5 min incubation. This is a 162-fold enhancement in sensitivity compared to that without enrichment.

Our device has comparable performance with the ICP enhanced immunoassay devices using Nafion film[72]. This structure and preconcentration mechanism can be useful to improve the efficiency and the multiplexing capability of silicon/silica based preconcentrators. The

performance of this device can be tuned easily by increasing the number or changing the dimensions of the pillars without changing the fabrication process.

To move this ICP-based technology towards commercialization and eventual use in the clinic, we need a more fundamental understanding of ICP mechanisms. Both additional understanding of all of the underlying processes at work and mathematical models of ICP are necessary for further development of this technology. Most ICP modeling results have the nanochannel perpendicular to microchannels, so the modeling specifically for this nanogap-design will be tremendously helpful to apply this ICP mechanism in more biosensing systems. For example, one of the challenging problems is the instability of the concentration plug. In our hands, enrichment zones were not stable under high voltage, long enrichment time, and complex biological solutions. This instability might be due to various factors, including dynamic pH changes, ohmic heating, biomolecule aggregation, and nanogap blockage. Mitigating this instability is critical for future development and commercialization of ICP-based preconcentration devices.

With regards to our specific design, several areas deserve additional attention. First, fabricating robust nanogaps (or permselective membranes) with high yield remains challenging. Second, enrichment required low ionic strength (~15mM) solutions. It would be preferable to modify the method to enable preconcentration in high ionic strength (>100mM) solution or serum samples. Third, nanogaps would sometimes block, generating instabilities which could be compensated by the researcher but required feedback. Lastly, as mentioned above, we noticed that the enrichment zones often became unstable and moved away from their designed location, making detection difficult.

Once fully developed, we expect ICP-based enrichment to be used in more assays with a broad range of analytes. The mechanism of ICP can only accumulate charged molecules. However, most clinical analytes have charge at physiological pH, so ICP-based preconcentration can be utilized for most biological analytes in the fields of healthcare, food industry, and environmental monitoring[1][61]. In addition, this preconcentration technique can be incorporated with other biosensing techniques to boost the performance of those other techniques. For example, this device could be combined with label-free detection methods (for example, electrochemical detection methods [56,156]) to speed up those assays.

Reference:

1. Fu LM, Hou HH, Chiu PH, Yang RJ. Sample preconcentration from dilute solutions on micro/nanofluidic platforms: A review. Electrophoresis. 2018;39: 289–310. doi:10.1002/elps.201700340
2. Sonker M, Sahore V, Woolley AT. Recent advances in microfluidic sample preparation and separation techniques for molecular biomarker analysis: A critical review. Anal Chim Acta. Elsevier Ltd; 2017;986: 1–11. doi:10.1016/j.aca.2017.07.043
3. Son SY, Lee S, Lee H, Kim SJ. Engineered nanofluidic preconcentration devices by ion concentration polarization. Biochip J. 2016;10: 251–261. doi:10.1007/s13206-016-0401-7
4. Liu CC, Wang YN, Fu LM, Chieh C. Micro-distillation system for formaldehyde concentration detection. Chem Eng J. Elsevier B.V.; 2016;304: 419–425. doi:10.1016/j.cej.2016.06.114
5. Yang R, Hou H, Wang Y, Fu L. Sensors and Actuators B : Chemical Micro-magnetofluidics in microfluidic systems : A review. Sens Actuators B Chem. Elsevier B.V.; 2016;224: 1–15. doi:10.1016/j.snb.2015.10.053
6. Liu CC, Wang YN, Fu LM, Yang DY. Rapid integrated microfluidic paper-based system for sulfur dioxide detection. Chem Eng J. Elsevier B.V.; 2017;316: 790–796. doi:10.1016/j.cej.2017.02.023
7. da Costa ET, Santos MFS, Jiao H, do Lago CL, Gutz IGR, Garcia CD. Fast production of microfluidic devices by CO2 laser engraving of wax-coated glass slides. Electrophoresis. 2016;37: 1691–1695. doi:10.1002/elps.201600065
8. Das D, Phan DT, Zhao Y, Kang Y, Chan V, Yang C. A multi-module microfluidic platform for continuous pre-concentration of water-soluble ions and separation of oil droplets from oil-in-water (O/W) emulsions using a DC-biased AC electrokinetic technique. Electrophoresis. 2017;38: 645–652. doi:10.1002/elps.201600477
9. Rusling JF, Kumar C V., Gutkind JS, Patel V. Measurement of biomarker proteins for point-of-care early detection and monitoring of cancer. Analyst. 2010;135: 2496–2511. doi:10.1039/c0an00204f
10. Chikkaveeraiah B V., Mani V, Patel V, Gutkind JS, Rusling JF. Microfluidic electrochemical immunoarray for ultrasensitive detection of two cancer biomarker proteins in serum. Biosens Bioelectron. Elsevier B.V.; 2011;26: 4477–4483. doi:10.1016/j.bios.2011.05.005
11. Aragay G, Pons J, Merkoçi A. Recent Trends in Macro-, Micro-, and Nanomaterial-Based Tools and Strategies for Heavy-Metal Detection. Chem Rev. 2011;111: 3433–3458. doi:10.1021/cr100383r
12. Sheehan PE, Whitman LJ. Detection Limits for Nanoscale Biosensors. Nano Lett. 2005;5: 803–807. doi:10.1021/nl050298x
13. Sparreboom W, van den Berg a, Eijkel JCT. Principles and applications of nanofluidic transport. Nat Nanotechnol. Nature Publishing Group; 2009;4: 713–720. doi:10.1038/nnano.2009.332
14. Nair PR, Alam MA. Performance limits of nanobiosensors. Appl Phys Lett. 2006;88: 9–11. doi:10.1063/1.2211310
15. Cohen AE, Fields AP. The cat that caught the canary: What to do with single-molecule trapping. ACS Nano. 2011;5: 5296–5299. doi:10.1021/nn202313g

16. Wang YC, Han J. Pre-binding dynamic range and sensitivity enhancement for immuno-sensors using nanofluidic preconcentrator. Lab Chip. 2008;8: 392–394. doi:10.1039/b717220f
17. Schulte W, Bernhagen J, Bucala R. Review ArticleCytokines in Sepsis: Potent Immunoregulators and Potential Therapeutic Targets—An Updated View. 2013;2013: 1–17. Available: papers3://publication/uuid/58BF094B-59D1-4CC3-A3B6-1B2B116F42F8
18. Iskander KN, Osuchowski MF, Stearns-Kurosawa DJ, Kurosawa S, Stepien D, Valentine C, et al. Sepsis: multiple abnormalities, heterogeneous responses, and evolving understanding. Physiol Rev. 2013;93: 1247–88. doi:10.1152/physrev.00037.2012
19. DAMA P, LEDOUX D, NYS M, VRINDTS Y, GROOTE D DE, FRANCHIMONT P, et al. Cytokine Serum Level During Severe Sepsis in Human IL-6 as a Marker of Severity. Ann Surg. 1992;215: 356–362. doi:10.1097/00000658-199204000-00009
20. Hou T, Huang D, Zeng R, Ye Z, Zhang Y. Accuracy of serum interleukin (IL)-6 in sepsis diagnosis: a systematic review and meta-analysis. Int J Clin Exp Med. 2015;8: 15238–15245. Available: http://www.ncbi.nlm.nih.gov/pubmed/26629009%0Ahttp://www.pubmedcentral.nih.gov/articlerender.fcgi?artid=PMC4658898
21. Takahashi W, Watanabe E, Fujimura L, Watanabe-Takano H, Yoshidome H, Swanson PE, et al. Kinetics and protective role of autophagy in a mouse cecal ligation and puncture-induced sepsis. Crit Care. 2013;17. doi:10.1186/cc12839
22. Gauer RL. Early recognition and management of sepsis in adults: The first six hours. Am Fam Physician. 2013;88: 44–53. doi:10.1016/j.nwh.2016.02.003
23. Hotchkiss RS, Monneret G, Payen D. Immunosuppression in sepsis: A novel understanding of the disorder and a new therapeutic approach. Lancet Infect Dis. Elsevier Ltd; 2013;13: 260–268. doi:10.1016/S1473-3099(13)70001-X
24. Chaudhry H, Zhou J, Zhong Y, Ali MM, Mcguire F, Nagarkatti PS, et al. Role of cytokines as a double-edged sword in sepsis. In Vivo (Brooklyn). 2013;27: 669–684.
25. Lu T, Lee H, Chen T, Herchak S, Kim J-H, Fraser SE, et al. High sensitivity nanoparticle detection using optical microcavities. Proc Natl Acad Sci. 2011;108: 5976–5979. doi:10.1073/pnas.1017962108
26. Tekin HC, Gijs MAM. Ultrasensitive protein detection: A case for microfluidic magnetic bead-based assays. Lab Chip. 2013;13: 4711–4739. doi:10.1039/c3lc50477h
27. Joo J, Kwon D, Yim C, Jeon S. Highly sensitive diagnostic assay for the detection of protein biomarkers using microresonators and multifunctional nanoparticles. ACS Nano. 2012;6: 4375–4381. doi:10.1021/nn301071c
28. Ding Y, Mutharasan R. Highly sensitive and rapid detection of microcystin-LR in source and finished water samples using cantilever sensors. Environ Sci Technol. 2011;45: 1490–1496. doi:10.1021/es1020795
29. Yin TI, Zhao Y, Horak J, Bakirci H, Liao HH, Tsai HH, et al. A micro-cantilever sensor chip based on contact angle analysis for a label-free troponin i immunoassay. Lab Chip. 2013;13: 834–842. doi:10.1039/c2lc40767a
30. Lee JH, Hwang KS, Park J, Yoon KH, Yoon DS, Kim TS. Immunoassay of prostate-specific antigen (PSA) using resonant frequency shift of piezoelectric nanomechanical microcantilever. Biosens Bioelectron. 2005;20: 2157–2162. doi:10.1016/j.bios.2004.09.024
31. Jiang T, Zhang L, Zhou J. Silver nanocube-mediated sensitive immunoassay based on

surface-enhanced Raman scattering assisted by etched silicon nanowire arrays. Analyst. Royal Society of Chemistry; 2014;139: 5893–5900. doi:10.1039/c4an01293c
32. Men D, Guo Y, Zhang Z, Wei H. Protein Nanowires Dramatically Increase the Sensitivity of Immunoassays. Nano Lett. 2009;9: 2246–2250. doi:10.1021/nl9003464
33. Tang J, Tang D, Su B, Li Q, Qiu B, Chen G. Silver nanowire-graphene hybrid nanocomposites as label for sensitive electrochemical immunoassay of alpha-fetoprotein. Electrochim Acta. Elsevier Ltd; 2011;56: 8168–8175. doi:10.1016/j.electacta.2011.05.128
34. Zheng G, Patolsky F, Cui Y, Wang WU, Lieber CM. Multiplexed electrical detection of cancer markers with nanowire sensor arrays. Nat Biotechnol. 2005;23: 1294–1301. doi:10.1038/nbt1138
35. Du D, Zou Z, Shin Y, Wang J, Wu H, Engelhard MH, et al. Sensitive immunosensor for cancer biomarker based on dual signal amplification strategy of graphene sheets and multienzyme functionalized carbon nanospheres. Anal Chem. 2010;82: 2989–2995. doi:10.1021/ac100036p
36. Du D, Wang L, Shao Y, Wang J, Engelhard MH, Lin Y. Functionalized graphene oxide as a nanocarrier in a multienzyme labeling amplification strategy for ultrasensitive electrochemical immunoassay of phosphorylated p53 (s392). Anal Chem. 2011;83: 746–752. doi:10.1021/ac101715s
37. Vashist SK, Marion Schneider E, Zengerle R, von Stetten F, Luong JHT. Graphene-based rapid and highly-sensitive immunoassay for C-reactive protein using a smartphone-based colorimetric reader. Biosens Bioelectron. Elsevier; 2015;66: 169–176. doi:10.1016/j.bios.2014.11.017
38. Zhong Z, Wu W, Wang D, Wang D, Shan J, Qing Y, et al. Nanogold-enwrapped graphene nanocomposites as trace labels for sensitivity enhancement of electrochemical immunosensors in clinical immunoassays: Carcinoembryonic antigen as a model. Biosens Bioelectron. Elsevier B.V.; 2010;25: 2379–2383. doi:10.1016/j.bios.2010.03.009
39. Liu Y, Liu Y, Feng H, Wu Y, Joshi L, Zeng X, et al. Layer-by-layer assembly of chemical reduced graphene and carbon nanotubes for sensitive electrochemical immunoassay. Biosens Bioelectron. Elsevier B.V.; 2012;35: 63–68. doi:10.1016/j.bios.2012.02.007
40. Law WC, Yong KT, Baev A, Prasad PN. Sensitivity improved surface plasmon resonance biosensor for cancer biomarker detection based on plasmonic enhancement. ACS Nano. 2011;5: 4858–4864. doi:10.1021/nn2009485
41. Mayer KM, Hao F, Lee S, Nordlander P, Hafner JH. A single molecule immunoassay by localized surface plasmon resonance. Nanotechnology. 2010;21: 255503. doi:10.1088/0957-4484/21/25/255503
42. Wang Y, Dostalek J, Knoll W. Magnetic nanoparticle-enhanced biosensor based on grating-coupled surface plasmon resonance. Anal Chem. 2011;83: 6202–6207. doi:10.1021/ac200751s
43. Liu M, Ning B, Qu L, Peng Y, Dong J, Gao N, et al. Development of indirect competitive immunoassay for highly sensitive determination of ractopamine in pork liver samples based on surface plasmon resonance sensor. Sensors Actuators, B Chem. Elsevier B.V.; 2012;161: 124–130. doi:10.1016/j.snb.2011.09.078
44. Gnedenko O V., Mezentsev Y V., Molnar AA, Lisitsa A V., Ivanov AS, Archakov AI. Highly sensitive detection of human cardiac myoglobin using a reverse sandwich immunoassay with a gold nanoparticle-enhanced surface plasmon resonance biosensor. Anal Chim Acta. Elsevier B.V.; 2013;759: 105–109. doi:10.1016/j.aca.2012.10.053

45. Jaffrin MY. Hydrodynamic Techniques to Enhance Membrane Filtration. Annu Rev Fluid Mech. 2011;44: 77–96. doi:10.1146/annurev-fluid-120710-101112
46. Van Der Bruggen B, Vandecasteele C, Van Gestel T, Doyen W, Leysen R. A review of pressure-driven membrane processes in wastewater treatment and drinking water production. Environ Prog. 2003;22: 46–56. doi:10.1002/ep.670220116
47. Wei W, Xue G, Yeung ES. One-step concentration of analytes based on dynamic change in pH in capillary zone electrophoresis. Anal Chem. 2002;74: 934–940. doi:10.1021/ac015617t
48. Arnett SD, Lunte CE. Investigation of the mechanism of pH-mediated stacking of anions for the analysis of physiological samples by capillary electrophoresis. Electrophoresis. 2003;24: 1745–1752. doi:10.1002/elps.200305399
49. Beard NP, Zhang C-X, DeMello AJ. In-column field-amplified sample stacking of biogenic amines on microfabricated ellectrophoresis devices. Electrophoresis. 2003;24: 732–739. doi:10.1002/elps.200390088
50. Lichtenberg J, Verpoorte E, de Rooij NF. Sample preconcentration by field amplication stacking for microchip-based capillary electrophoresis. Electrophoresis. 2001. pp. 258–271. doi:10.1002/1522-2683(200101)22:2<258::AID-ELPS258>3.0.CO;2-4
51. Chen JZ, Balgley BM, DeVoe DL, Lee CS. Capillary isoelectric focusing-based multidimensional concentration. Anal Chem. 2003;75: 3145–3152. doi:10.1021/ac034014+
52. Herr AE, Molho JI, Drouvalakis KA, Mikkelsen JC, Utz PJ, Santiago JG, et al. On-chip coupling of isoelectric focusing and free solution electrophoresis for multidimensional separations. Anal Chem. 2003;75: 1180–1187. doi:10.1021/ac026239a
53. Cui H, Horiuchi K, Dutta P, Ivory CF. Multistage isoelectric focusing in a polymeric microfluidic chip. Anal Chem. 2005;77: 7878–7886. doi:10.1021/ac050781s
54. Cui H, Horiuchi K, Dutta P, Ivory CF. Isoelectric focusing in a poly(dimethylsiloxane) microfluidic chip. Anal Chem. 2005;77: 1303–9. doi:10.1021/ac048915+
55. Liao KT, Chou CF. Nanoscale molecular traps and dams for ultrafast protein enrichment in high-conductivity buffers. J Am Chem Soc. 2012;134: 8742–8745. doi:10.1021/ja3016523
56. Sanghavi BJ, Varhue W, Rohani A, Liao K-T, Bazydlo LAL, Chou C-F, et al. Ultrafast immunoassays by coupling dielectrophoretic biomarker enrichment in nanoslit channel with electrochemical detection on graphene. Lab Chip. 2015;15: 4563–4570. doi:10.1039/C5LC00840A
57. Sanghavi BJ, Varhue W, Chávez JL, Chou CF, Swami NS. Electrokinetic preconcentration and detection of neuropeptides at patterned graphene-modified electrodes in a nanochannel. Anal Chem. 2014;86: 4120–4125. doi:10.1021/ac500155g
58. Liao KT, Tsegaye M, Chaurey V, Chou CF, Swami NS. Nano-constriction device for rapid protein preconcentration in physiological media through a balance of electrokinetic forces. Electrophoresis. 2012;33: 1958–1966. doi:10.1002/elps.201100707
59. Jung B, Bharadwaj R, Santiago JG. On-chip millionfold sample stacking using transient isotachophoresis. Anal Chem. 2006;78: 2319–2327. doi:10.1021/ac051659w
60. Wang YC, Stevens AL, Han J. Million-fold preconcentration of proteins and peptides by nanofluidic filter. Anal Chem. 2005;77: 4293–4299. doi:10.1021/ac050321z
61. Kim SJ, Song YA, Han J. Nanofluidic concentration devices for biomolecules utilizing ion concentration polarization: Theory, fabrication, and applications. Chem Soc Rev.

2010;39: 912–922. doi:10.1039/b822556g
62. Ouyang W, Ye X, Li Z, Han J. Deciphering ion concentration polarization-based electrokinetic molecular concentration at the micro-nanofluidic interface: theoretical limits and scaling laws. Nanoscale. Royal Society of Chemistry; 2018;10: 15187–15194. doi:10.1039/c8nr02170h
63. Mani A, Zangle TA, Santiago JG. On the Propagation of Concentration Polarization from Characteristic Analysis. Langmuir. 2009;25: 3898–3908. doi:10.1021/la803317p
64. Kim SJ, Wang YC, Lee JH, Jang H, Han J. Concentration polarization and nonlinear electrokinetic flow near a nanofluidic channel. Phys Rev Lett. 2007;99: 1–4. doi:10.1103/PhysRevLett.99.044501
65. Yossifon G, Mushenheim P, Chang YC, Chang HC. Eliminating the limiting-current phenomenon by geometric field focusing into nanopores and nanoslots. Phys Rev E - Stat Nonlinear, Soft Matter Phys. 2010;81: 1–13. doi:10.1103/PhysRevE.81.046301
66. Chung PS, Fan YJ, Sheen HJ, Tian WC. Real-time dual-loop electric current measurement for label-free nanofluidic preconcentration chip. Lab Chip. Royal Society of Chemistry; 2015;15: 319–330. doi:10.1039/c4lc01143k
67. Pu Q, Yun J, Temkin H, Liu S. Ion-enrichment and ion-depletion effect of nanochannel structures. Nano Lett. 2004;4: 1099–1103. doi:10.1021/nl0494811
68. Ouyang W, Ko SH, Wu D, Wang AY, Barone PW, Hancock WS, et al. Rapid Assessment of Therapeutic Proteins Using Molecular Charge Modulation Enhanced Electrokinetic Concentration Assays. Anal Chem. 2016;88: 9669–9677. doi:10.1021/acs.analchem.6b02517
69. Reverberi R, Reverberi L. Factors affecting the antigen-antibody reaction. Blood Transfus. 2007;5: 227–240. doi:10.2450/2007.0047-07
70. Lee JH, Han J. Concentration-enhanced rapid detection of human chorionic gonadotropin as a tumor marker using a nanofluidic preconcentrator. Microfluid Nanofluidics. 2010;9: 973–979. doi:10.1007/s10404-010-0598-z
71. Ko SH, Kim SJ, Cheow LF, Li LD, Kang KH, Han J. Massively parallel concentration device for multiplexed immunoassays. Lab Chip. 2011;11: 1351–1358. doi:10.1039/c0lc00349b
72. Ko SH, Song Y-AA, Kim SJ, Kim M, Han J, Kang KH. Nanofluidic preconcentration device in a straight microchannel using ion concentration polarization. Lab Chip. 2012;12: 4472. doi:10.1039/c2lc21238b
73. Chao CC, Chiu PH, Yang RJ. Preconcentration of diluted biochemical samples using microchannel with integrated nanoscale Nafion membrane. Biomed Microdevices. 2015;17. doi:10.1007/s10544-015-9940-2
74. Kwak R, Kang JY, Kim TS. Spatiotemporally Defining Biomolecule Preconcentration by Merging Ion Concentration Polarization. Anal Chem. 2016;88: 988–996. doi:10.1021/acs.analchem.5b03855
75. Yoo YK, Yoon DS, Kim G, Kim J, Han S Il, Lee J, et al. An Enhanced Platform to Analyse Low-Affinity Amyloid β Protein by Integration of Electrical Detection and Preconcentrator. Sci Rep. Springer US; 2017;7: 1–8. doi:10.1038/s41598-017-14338-4
76. Lee JH, Song Y, Tannenbaum SR, Han J. Increase of Reaction Rate and Sensitivity of Low-Abundance Enzyme Assay Using Micro/ Nanofluidic Preconcentration Chip. Lab Chip. 2008;80: 6592–6598. doi:10.1039/B717900F.Analytical
77. Fan YJ, Deng CZ, Chung PS, Tian WC, Sheen HJ. A high sensitivity bead-based

immunoassay with nanofluidic preconcentration for biomarker detection. Sensors Actuators, B Chem. Elsevier; 2018;272: 502–509. doi:10.1016/j.snb.2018.05.141
78. Lee JH, Song Y-A, Han J. Multiplexed proteomic sample preconcentration device using surface-patterned ion-selective membrane. Lab Chip. 2008;8: 596–601. doi:10.1039/b717900f
79. Choi E, Kwon K, Kim D, Park J. An electrokinetic study on tunable 3D nanochannel networks constructed by spatially controlled nanoparticle assembly. Lab Chip. Royal Society of Chemistry; 2015;15: 512–523. doi:10.1039/c4lc00949e
80. Syed A, Mangano L, Mao P, Han J, Song YA. Creating sub-50 nm nanofluidic junctions in a PDMS microchip via self-assembly process of colloidal silica beads for electrokinetic concentration of biomolecules. Lab Chip. Royal Society of Chemistry; 2014;14: 4455–4460. doi:10.1039/c4lc00895b
81. Quist J, Trietsch SJ, Vulto P, Hankemeier T. Elastomeric microvalves as tunable nanochannels for concentration polarization. Lab Chip. 2013;13: 4810–4815. doi:10.1039/c3lc50658d
82. Chung S, Lee JH, Moon M-W, Han J, Kamm RD. Non-Lithographic Wrinkle Nanochannels for Protein Preconcentration. Adv Mater. 2008;20: 3011–3016. doi:10.1002/adma.200701715
83. Jeong HL, Chung S, Sung JK, Han J. Poly(dimethylsiloxane)-based protein preconcentration using a nanogap generated by junction gap breakdown. Anal Chem. 2007;79: 6868–6873. doi:10.1021/ac071162h
84. Kim SJ, Han J. Self-Sealed Vertical Polymeric Nanoporous-Junctions for High-Throughput Nanofluidic Applications. Anal Chem. 2008;80: 3507–3511. doi:10.1021/ac800157q
85. Schepelina O, Zharov I. Poly (2- (dimethylamino) ethyl methacrylate) -Modified Nanoporous Colloidal Films with pH and Ion Response. Langmuir. 2008; 14188–14194. doi:10.1021/la802453z
86. Smith JJ, Zharov I. Ion transport in sulfonated nanoporous opal films. ACS Symp Ser. 2008;996: 248–255. doi:10.1021/bk-2008-0996.ch018
87. Schepelina O, Zharov I. PNIPAAM-modified nanoporous colloidal films with positive and negative temperature gating. Langmuir. 2007;23: 12704–12709. doi:10.1021/la702008j
88. Moon M-W, Lee SH, Sun J-Y, Oh KH, Vaziri A, Hutchinson JW. Wrinkled hard skins on polymers created by focused ion beam. Proc Natl Acad Sci. 2007;104: 1130–1133. doi:10.1073/pnas.0610654104
89. Efimenko K, Rackaitis M, Manias E, Vaziri A, Mahadevan L, Genzer J. Nested self-similar wrinkling patterns in skins. Nat Mater. 2005;4: 293–297. doi:10.1038/nmat1342
90. Chun H, Chung TD, Ramsey JM. High yield sample preconcentration using a highly ion-conductive charge-selective polymer. Anal Chem. 2010;82: 6287–6292. doi:10.1021/ac101297t
91. Song S, Singh AK, Kirby BJ. Electrophoretic concentration of proteins at laser-patterned nanoporous membranes in microchips. Anal Chem. 2004;76: 4589–4592. doi:10.1021/ac0497151
92. Hlushkou D, Dhopeshwarkar R, Crooks RM, Tallarek U. The influence of membrane ion-permselectivity on electrokinetic concentration enrichment in membrane-based preconcentration units. Lab Chip. 2008;8: 1153–1162. doi:10.1039/b800549d

93. Dhopeshwarkar R, Sun L, Crooks RM. Electrokinetic concentration enrichment within a microfluidic device using a hydrogel microplug. Lab Chip. 2005;5: 1148–1154. doi:10.1039/b509063f
94. Yang RJ, Pu HH, Wang HL. Ion concentration polarization on paper-based microfluidic devices and its application to preconcentrate dilute sample solutions. Biomicrofluidics. 2015;9. doi:10.1063/1.4913366
95. Yeh SH, Chou KH, Yang RJ. Sample pre-concentration with high enrichment factors at a fixed location in paper-based microfluidic devices. Lab Chip. Royal Society of Chemistry; 2016;16: 925–931. doi:10.1039/c5lc01365h
96. Jianrong C, Yuqing M, Nongyue H, Xiaohua W, Sijiao L. Nanotechnology and biosensors. Biotechnol Adv. 2004;22: 505–518. doi:10.1016/j.biotechadv.2004.03.004
97. Haes AJ, Van Duyne RP. A nanoscale optical biosensor: Sensitivity and selectivity of an approach based on the localized surface plasmon resonance spectroscopy of triangular silver nanoparticles. J Am Chem Soc. 2002;124: 10596–10604. doi:10.1021/ja020393x
98. Zoller FA, Padeste C, Ekinci Y, Solak HH, Engel A. Nanostructured substrates for high density protein arrays. Microelectron Eng. 2008;85: 1370–1374. doi:10.1016/j.mee.2007.12.061
99. Zhou G, Bergeron S, Juncker D. High-performance low-cost antibody microarrays using enzyme-mediated silver amplification. J Proteome Res. 2015;14: 1872–1879. doi:10.1021/pr501259e
100. Han SW, Lee S, Hong J, Jang E, Lee T, Koh WG. Mutiscale substrates based on hydrogel-incorporated silicon nanowires for protein patterning and microarray-based immunoassays. Biosens Bioelectron. 2013;45: 129–135. doi:10.1016/j.bios.2013.01.062
101. Bernard A, Renault JP, Michel B, Bosshard HR, Delamarche E. Microcontact printing of proteins. Adv Mater. 2000;12: 1067–1070. doi:Doi 10.1002/1521-4095(200007)12:14<1067::Aid-Adma1067>3.0.Co;2-M
102. Filipponi L, Livingston P, Kašpar O, Tokárová V, Nicolau D V. Protein patterning by microcontact printing using pyramidal PDMS stamps. Biomed Microdevices. 2016;18: 1–7. doi:10.1007/s10544-016-0036-4
103. Zhou G, Bergeron S, Ricoult S, Juncker D. Digitizing immunoassay on an antibody nanoarray to improve assay sensitivity. 2013 Transducers Eurosensors XXVII 17th Int Conf Solid-State Sensors, Actuators Microsystems, TRANSDUCERS EUROSENSORS 2013. 2013; 2783–2786. doi:10.1109/Transducers.2013.6627383
104. Bernard A, Delamarche E, Schmid H, Michel B, Bosshard HR, Biebuyck H. Printing patterns of proteins. Langmuir. 1998;14: 2225–2229. doi:10.1021/la980037l
105. Lee K-B. Protein Nanoarrays Generated By Dip-Pen Nanolithography. Science (80-). 2002;295: 1702–1705. doi:10.1126/science.1067172
106. Salaita K, Wang Y, Mirkin C a. Applications of dip-pen nanolithography. Nat Nanotechnol. 2007;2: 145–155. doi:10.1038/nnano.2007.39
107. Piner RD, Zhu J, Xu F, Hong S. "Dip-Pen" Nanolithography. 1999;283: 661–663. doi:10.1126/science.283.5402.661
108. Veiseh M, Zareie MH, Zhang M. Highly selective protein patterning on gold-silicon substrates for biosensor applications. Langmuir. 2002;18: 6671–6678. doi:10.1021/la025529j
109. Lan S, Veiseh M, Zhang M. Surface modification of silicon and gold-patterned silicon surfaces for improved biocompatibility and cell patterning selectivity. Biosens

Bioelectron. 2005;20: 1697–1708. doi:10.1016/j.bios.2004.06.025
110. Frasconi M, Mazzei F, Ferri T. Protein immobilization at gold-thiol surfaces and potential for biosensing. Anal Bioanal Chem. 2010;398: 1545–1564. doi:10.1007/s00216-010-3708-6
111. Lee SH, Lee CS, Shin DS, Kim BG, Lee YS, Kim YK. Micro protein patterning using a lift-off process with fluorocarbon thin film. Sensors Actuators, B Chem. 2004;99: 623–632. doi:10.1016/j.snb.2003.11.040
112. Sorribas H, Padeste C, Tiefenauer L. Photolithographic generation of protein micropatterns for neuron culture applications. Biomaterials. 2002;23: 893–900. doi:10.1016/S0142-9612(01)00199-5
113. Yin L, Cheng H, Mao S, Haasch R, Liu Y, Xie X, et al. Dissolvable metals for transient electronics. Adv Funct Mater. 2014;24: 645–658. doi:10.1002/adfm.201301847
114. Harvey WW, Gatos HC. The Reaction of Germanium with Aqueous Solutions Dissolution Kinetics in Water Containing Dissolved Oxygen. J Electrochem Soc. 1959;105: 654–660.
115. Cerniglia N, Wang P. Dissolution of Germanium in Aqueous Hydrogen Peroxide Solution. J Electrochem Soc. 1962;109: 508–512.
116. Lu B, Maharbiz MM. Protein patterning using germanium as a sacrificial layer. Proc Annu Int Conf IEEE Eng Med Biol Soc EMBS. 2017; 1865–1868. doi:10.1109/EMBC.2017.8037210
117. Kang SK, Park G, Kim K, Hwang SW, Cheng H, Shin J, et al. Dissolution chemistry and biocompatibility of silicon- and germanium-based semiconductors for transient electronics. ACS Appl Mater Interfaces. 2015;7: 9297–9305. doi:10.1021/acsami.5b02526
118. Cohen DJ, Gloerich M, Nelson WJ. Epithelial self-healing is recapitulated by a 3D biomimetic E-cadherin junction. Proc Natl Acad Sci U S A. 2016;113: 14698–14703. doi:10.1073/pnas.1612208113
119. Heck JM. Polycrystalline Silicon Germanium for Fabrication, Release, and Packaging of Microelectromechanical Systems. 2001;
120. Gu J, Gupta R, Chou CF, Wei Q, Zenhausern F. A simple polysilsesquioxane sealing of nanofluidic channels below 10 nm at room temperature. Lab Chip. 2007;7: 1198–1201. doi:10.1039/b704851c
121. Leichlé T, Lin YL, Chiang PC, Hu SM, Liao KT, Chou CF. Biosensor-compatible encapsulation for pre-functionalized nanofluidic channels using asymmetric plasma treatment. Sensors Actuators, B Chem. Elsevier B.V.; 2012;161: 805–810. doi:10.1016/j.snb.2011.11.036
122. Tang KC, Liao E, Ong WL, Wong JDS, Agarwal A, Nagarajan R, et al. Evaluation of bonding between oxygen plasma treated polydimethyl siloxane and passivated silicon. J Phys Conf Ser. 2006;34: 155–161. doi:10.1088/1742-6596/34/1/026
123. Sui J, Zhang S, Liu Z, Yan J, Dai Z. A multi-scale study on silicon-oxide etching processes in C 4 F 8 /Ar plasmas. Plasma Sci Technol. 2016;18: 666–673. doi:10.1088/1009-0630/18/6/14
124. Kleiner G, Marcuzzi A, Zanin V, Monasta L, Zauli G. Cytokine Levels in the Serum of Healthy Subjects. Mediat Inflamm. 2013;2013. doi:10.1155/2013/434010
125. Simmons EM, Himmelfarb J, Tugrul Sezer M, Chertow GM, Mehta RL, Paganini EP, et al. Plasma cytokine levels predict mortality in patients with acute renal failure. Kidney Int. 2004;65: 1357–1365. doi:10.1111/j.1523-1755.2004.00512.x
126. Kim HO, Kim HS, Youn JC, Shin EC, Park S. Serum cytokine profiles in healthy young

and elderly population assessed using multiplexed bead-based immunoassays. J Transl Med. BioMed Central Ltd; 2011;9: 113. doi:10.1186/1479-5876-9-113
127. Frangiamore SJ, Saleh A, Grosso MJ, Farias Kovac M, Zhang X, Daly TM, et al. Neer Award 2015: Analysis of cytokine profiles in the diagnosis of periprosthetic joint infections of the shoulder. J Shoulder Elb Surg. Elsevier Inc.; 2017;26: 186–196. doi:10.1016/j.jse.2016.07.017
128. Blauw M, Zijlstra T, Drift E. Balancing the etching and passivation in time-multiplexed deep dry etching of silicon. J Vac Sci Technol B Microelectron Nanom Struct. 2001;19. doi:10.1116/1.1415511
129. Rangelow I. Critical tasks in high aspect ratio silicon dry etching for microelectromechanical systems. J Vac Sci Technol A - J VAC SCI TECHNOL A. 2003;21: 1550–1562. doi:10.1116/1.1580488
130. Wai Kok K, Yoo W, Sooriakumar K, Pan JS, Lee EY. Investigation of in situ trench etching process and Bosch process for fabricating high-aspect-ratio beams for microelectromechanical systems. J Vac Sci Technol B Microelectron Nanom Struct. 2002;20: 1878–1883. doi:10.1116/1.1501583
131. Franz Laermer, Andrea Schilp RBG. Method of anisotropically etching silicon, US5501893A Patent [Internet]. US Patent 5,501,893. 1993. Available: https://patents.google.com/patent/US5501893A/en
132. Min J-H, Lee J-K, Moon SH, Kim C-K. Deep etching of silicon with smooth sidewalls by an improved gas-chopping process using a Faraday cage and a high bias voltage. Journal of Vacuum Science & Technology B: Microelectronics and Nanometer Structures. 2005. p. 1405. doi:10.1116/1.1993623
133. Deal BE, Grove AS. General relationship for the thermal oxidation of silicon. J Appl Phys. 1965;36: 3770–3778. doi:10.1063/1.1713945
134. Deal BE. The Oxidation of Silicon in Dry Oxygen, Wet Oxygen, and Steam. J Electrochem Soc. 1963;110: 527. doi:10.1149/1.2425807
135. Bange A, Halsall HB, Heineman WR. Microfluidic immunosensor systems. Biosens Bioelectron. 2005;20: 2488–2503. doi:10.1016/j.bios.2004.10.016
136. Wu G, Datar RH, Hansen KM, Thundat T, Cote RJ, Majumdar A. Bioassay of prostate-specific antigen (PSA) using microcantilevers. Nat Biotechnol. 2001;19: 856–860. doi:10.1038/nbt0901-856
137. Kurita R, Yokota Y, Sato Y, Mizutani F, Niwa O. On-chip enzyme immunoassay of a cardiac marker using a microfluidic device combined with a portable surface plasmon resonance system. Anal Chem. 2006;78: 5525–5531. doi:10.1021/ac060480y
138. Cesaro-Tadic S, Dernick G, Juncker D, Buurman G, Kropshofer H, Michel B, et al. High-sensitivity miniaturized immunoassays for tumor necrosis factor a using microfluidic systems. Lab Chip. 2004;4: 563–569. doi:10.1039/b408964b
139. Grilli S, Miccio L, Gennari O, Coppola S, Vespini V, Battista L, et al. Active accumulation of very diluted biomolecules by nano-dispensing for easy detection below the femtomolar range. Nat Commun. Nature Publishing Group; 2014;5: 1–6. doi:10.1038/ncomms6314
140. Cheow LF, Han J. Continuous Signal Enhancement for Sensitive Aptamer Affinity Probe Electrophoresis Assay Using Electrokinetic Concentration. Anal Chem. 2011;83: 7086–7093. doi:10.1021/ac201307d.Continuous
141. Choi J, Huh K, Moon DJ, Chae JH, Kim HC, Hong JW, et al. AN ELECTROKINETIC

DEVICE FOR SELECTIVE PRECONCENTRATION AND ONLINE COLLECTION BASED ON ION CONCENTRATION POLARIZATION. Transducers. 2015. pp. 228–231. doi:10.1109/TRANSDUCERS.2015.7180903
142. Leinweber FC, Tallarek U. Nonequilibrium electrokinetic effects in beds of ion-permselective particles. Langmuir. 2004;20: 11637–11648. doi:10.1021/la048408n
143. Rubinstein SM, Manukyan G, Staicu A, Rubinstein I, Zaltzman B, Lammertink RGH, et al. Direct observation of a nonequilibrium electro-osmotic instability. Phys Rev Lett. 2008;101: 1–4. doi:10.1103/PhysRevLett.101.236101
144. Qiu B, Gong L, Li Z, Han J. Electrokinetic flow in the U-shaped micro-nanochannels. Theor Appl Mech Lett. The Authors. Published by Elsevier Ltd on behalf of The Chinese Society of Theoretical and Applied Mechanics; 2019;9: 36–42. doi:10.1016/j.taml.2019.01.006
145. Gong L, Ouyang W, Li Z, Han J. Force fields of charged particles in micro-nanofluidic preconcentration systems. AIP Adv. 2017;7. doi:10.1063/1.5008365
146. Kwak R, Kim SJ, Han J. Continuous-flow biomolecule and cell concentrator by ion concentration polarization. Anal Chem. 2011;83: 7348–7355. doi:10.1021/ac2012619
147. Hecht AH, Sommer GJ, Durland RH, Yang X, Singh AK, Hatch A V. Aptamers as affinity reagents in an integrated electrophoretic lab-on-a-chip platform. Anal Chem. 2010;82: 8813–8820. doi:10.1021/ac101106m
148. Liu YF, Oey I, Bremer P, Carne A, Silcock P. Effects of pH, temperature and pulsed electric fields on the turbidity and protein aggregation of ovomucin-depleted egg white. Food Res Int. Elsevier Ltd; 2017;91: 161–170. doi:10.1016/j.foodres.2016.12.005
149. Borzova VA, Markossian KA, Chebotareva NA, Kleymenov SY, Poliansky NB, Muranov KO, et al. Kinetics of thermal denaturation andaggregation of bovine serum albumin. PLoS One. 2016;11: 1–29. doi:10.1371/journal.pone.0153495
150. Pereira RN, Souza BWS, Cerqueira MA, Teixeira JA, Vicente AA. Effects of electric fields on protein unfolding and aggregation: Influence on edible films formation. Biomacromolecules. 2010;11: 2912–2918. doi:10.1021/bm100681a
151. Wei Z, Ruijin Y, Yali T, Wenbin Z, Xiao H. Investigation of the protein-protein aggregation of egg white proteins under pulsed electric fields. J Agric Food Chem. 2009;57: 3571–3577. doi:10.1021/jf803900f
152. Bekard I, Dunstan DE. Electric field induced changes in protein conformation. Soft Matter. 2014;10: 431–437. doi:10.1039/c3sm52653d
153. Dittmer J, Dittmer A, Bruna RD, Kasche V. A native, affinity-based protein blot for the analysis of streptavidin heterogeneity: Consequences for the specificity of streptavidin mediated binding assays. Electrophoresis. 1989;10: 762–765. doi:10.1002/elps.1150101106
154. Hornbeck PV, Zhang B, Murray B, Kornhauser JM, Latham V, Skrzypek E PhosphoSitePlus, 2014: mutations, PTMs and recalibrations. Nucleic Acids Res. 2015 43:D512-20. In: 2014. 2014.
155. Behrens SH, Grier DG. The charge of glass and silica surfaces. J Chem Phys. 2001;115: 6716–6721. doi:10.1063/1.1404988
156. Chang B-Y, Park S-M. Electrochemical impedance spectroscopy. Annu Rev Anal Chem (Palo Alto Calif). 2010;3: 207–229. doi:10.1146/annurev.anchem.012809.102211